

Dissertation zur Erlangung des Doktorgrades
der Fakultät für Chemie und Pharmazie
der Ludwig–Maximilians–Universität München

Raman Radiation Studies of Nanocarbon Materials

von
Harald Patrick Budde
aus
München

2016

Erklärung

Diese Dissertation wurde im Sinne von §7 der Promotionsordnung vom 28. November 2011 von Herrn Prof. Dr. Achim Hartschuh betreut.

Eidesstattliche Versicherung

Diese Dissertation wurde eigenständig und ohne unerlaubte Hilfe erarbeitet.

München, den 13. September 2016

.....
(Harald Budde)

Dissertation eingereicht am: 15.09.2016
Erstgutachter: Prof. Dr. Achim Hartschuh
Zweitgutachter: Prof. Dr. Don C. Lamb
Mündliche Prüfung am 20.10.2016

Abstract

Raman spectroscopy is a valuable characterization method applicable to a broad range of materials. Vibrational information enclosed in the Raman spectrum provides access to various material properties. Because of the strong dependence of vibrations on the material architecture, Raman spectroscopy is an excellent technique for defect investigation. More detailed insight about the analyzed substance is gained by coupling Raman spectroscopy to back focal plane imaging, an experimental method that allows to angularly resolve radiation. This work mainly aims at understanding the physical processes occurring during the interaction of either electromagnetic or acoustic waves with nanocarbon material.

The first part reports on the angular distribution of Raman G and 2D scattering from graphene situated on a glass substrate recorded by back focal plane imaging. The Raman G emission can be seen as the superposition of two orthogonal incoherent point-dipoles, oriented in the sample plane, while the 2D Raman signal can be described as a sum of three incoherent point-dipoles each rotated by 120° . Parameter-free calculations of the G and 2D intensities are in excellent agreement with the experimental radiation patterns. The 2D polarization ratio depends on the numerical aperture of the microscope objective due to the depolarization of the emission and excitation light at the air-dielectric interface and tight focusing. Because of this, the polarization contrast decreases substantially for increasing collection angle. This also influences the 2D/G intensity ratio, a crucial quantity for the determination of single-layer graphene. The results are thus important for the quantitative analysis of the Raman intensities in confocal microscopy. First steps towards the measurement of antenna-enhanced Raman radiation patterns are shown. The pattern of the enhanced Raman G signal reflects the orientation of the optical antenna.

The second part addresses the Raman defect study of single-walled carbon nanotubes (SWCNTs) processed by a material-efficient dispersion method. This procedure is based on the recycling of the precipitate in multiple steps. SWCNTs from the recycling process exhibit longer mean lengths than SWCNTs extracted by comparable standard dispersion methods. The Raman defect density of the recycled SWCNTs is determined by recording the Raman D/G intensity ratio. The statistical Raman analysis shows a clear increase in defect density with rising sonication time. However, there is no increase in defect density with each recycling step. SWCNTs extracted in a late recycling step are localized in the center of a SWCNT aggregate protecting them from sonication.

Table of Contents

Abstract	v
0 Introduction	1
1 State of the Art	5
1.1 Graphene	5
1.1.1 Electronic Structure	6
1.1.2 Raman Spectroscopy of Graphene	7
1.1.3 Polarized Raman Spectroscopy of Graphene	12
1.2 Single-walled Carbon Nanotubes (SWCNTs)	18
1.2.1 Structure	18
1.2.2 Raman Spectroscopy of SWCNTs	22
2 Experimental Approach	27
2.1 Sample Preparation	27
2.1.1 Single-walled Carbon Nanotubes	27
2.1.2 Gold Nanorods	28
2.1.3 Graphene	31
2.2 Confocal Microscope Setup	32
2.3 Back Focal Plane Imaging	35
2.3.1 Theoretical Description of Radiation Patterns in the Back Focal Plane	35
2.3.2 Simulation of Dipolar Radiation Patterns in the Back Focal Plane .	37
2.3.3 Experimental Realization of Radiation Pattern Detection	40
2.3.4 Required Properties of the Microscope Objective	43
3 Raman Radiation Patterns of Graphene	47
3.1 State of the Art - Polarized Radiation Patterns and Depolarization	48
3.2 Polarization-dependent Raman Radiation Patterns of Graphene	51
3.3 Quantitative Raman Intensity Investigation	54
3.4 Fraction of Detected Light	60
3.5 Conclusion	61

4 Raman Defect Study of Recycled SWCNTs	63
4.1 Recycling of Dispersed SWCNTs and their Characterization	64
4.2 Raman Defect Study of Recycled SWCNTs	68
4.3 Conclusion	71
5 Summary and Outlook	72
Appendix	77
A Simulation of Polarized Radiation Patterns	77
B Antenna-enhanced Raman Radiation Patterns of Graphene	85
B.1 State of the Art - Optical Antennas and Their Influence on Radiation Patterns	86
B.2 Deposition, Localization and Identification of Single Gold Nanorods	88
B.3 Raman G Radiation Patterns Enhanced by Deposited Gold Nanorods	90
B.4 Conclusion and Outlook	92
Bibliography	93
Acronyms	109
List of Figures	116
List of Publications	117
List of Conferences	119
Acknowledgements	120

Introduction

The investigation of objects too small to recognize with the naked eye is a fascinating subject for humanity. More than 400 years ago the optical microscope was developed, an instrument creating magnified images of the sample by the collection of light through a glass lens. The invention gave access to detailed information about the shape of biological structures and led to the discovery of microorganisms. The coupling with a spectrometer enabled the extraction of various optical and electronic material properties. Lasers as a light source further expanded the scientific possibilities of the instrument. Besides resolving nanostructures at the resolution limit, for example local physical and chemical properties of single molecules and molecular processes on the timescale of 10^{-15} s can be observed with modern microscope systems [1, 2, 3].

In general, both microscopy and spectroscopy are based on the microscopic interaction between light and matter. Electromagnetic radiation that meets the interface of a material can transmit or absorb. A third possible light-matter interaction is scattering, which is a collective term for several physical phenomena such as refraction, diffraction and reflection. The classical example for scattering is the *Tyndall effect* [4], which is observed upon illumination of colloidal suspensions with white light. This effect describes the stronger scattering of short-wavelength components at the microscopic particles resulting in the diverging color appearance for different point of views.

Scattering is classified as elastic when the wavelength of the incident light is retained. An example for this is *Rayleigh scattering*, where the incident wavelength is significantly larger than the size of the scatterer [5, 6, 7, 8]. For excitation with a HeNe laser at 633 nm it is present at particle sizes between 1 to 60 nm. For larger particles at the same incident wavelength there are different scattering mechanisms (e.g. *Mie scattering*). An example for a scattering process with a changed wavelength is *Brillouin scattering*, where thermally excited acoustic phonons at the sample are involved [9]. As the frequency shift for this process is quite low ($10\text{-}10^6$ Hz), Brillouin scattering of visible light is considered as a quasi-elastic scattering process [10].

Raman scattering is the most prominent example for inelastic scattering. After its prediction in 1923 [11], Indian physicist and nobel prize winner Chandrasekhara Raman experimentally observed the effect five years later [12]. He focused sun light upon a sample

with a telescope lens and collected the scattered radiation with another lens. The altered wavelength of the scattered light was demonstrated with the help of an optical filter system. As Brillouin scattering, Raman scattering involves vibrational modes in the sample. However, it originates from the interaction between light and optical phonons or molecular vibrations. The rule of mutual exclusion states that for centrosymmetric molecules each vibrational mode is either Infrared- (IR) or Raman-active. Symmetric vibrational modes of these molecules cause a change in polarizability due to dislocation of charges and are thus Raman-active. In contrast, asymmetric vibrations cause a change of the dipole moment and are IR-active. Thus, for the investigation of vibrational properties both spectroscopy methods are complementary. However, IR spectroscopy often does not benefit from the implementation of a laser since it is based on the absorption of IR photons.

Many materials investigated by Raman spectroscopy leave a specific vibrational fingerprint in the Raman spectrum that can be used for their identification. A broad range of different information about the material is encoded in the spectrum, especially information concerning the material structure [13, 14, 15]. This facilitates the quality control and investigation of defects present in the sample material. Connected to this, Raman spectroscopy benefits from its applicability to various material states. As long as the probed vibrational modes are Raman-active, the sample can be solid, liquid or gaseous. Measurements are also possible for surface layers, microscopic or bulk material at various temperatures [16]. As the scattering intensity relative to the incident intensity is quite low ($I_S = 10^{-6}I_0$ for the Stokes process), Raman spectroscopy became a relevant analysis method only with the development of high intensity laser sources and sensitive detectors decades after the experimental discovery.

Over time, more sophisticated Raman techniques have been developed. Surface-enhanced Raman scattering (SERS) amplifies the Raman signal of molecules adsorbed to a rough noble metal surface or a substrate treated with noble metal colloids. This enables the determination of very low analyte concentrations [17]. For tip-enhanced Raman scattering (TERS), a sharp metal tip is brought in close proximity to the analyte. Optical processes within the small volume around the tip are enhanced. Thus, small sample features on the nanometer scale can be spatially resolved [18, 19, 20, 21]. To allow for separate and precise positioning of the metal tip, the optical setup is usually coupled with a scanning probe microscope (SPM). The amplification of both SERS and TERS originate from confined electric fields in the near-field of the metal structure generated by optically excited localized plasmons. For the case of amplification by TERS, the lightning rod effect needs to be considered as well.

Back focal plane imaging is an optical technique that enables the measurement of the radiation pattern formed by the collected signal light in the back aperture of a microscope objective. It illustrates the angularly resolved intensity map of the collected signal. The radiation pattern of single dipoles has been thoroughly studied and can be simulated by equations reported by *Lieb et al.* [22]. By comparison of recorded radiation patterns with

calculations and recorded patterns of known material systems [23, 24] further insight on the sample state and the emission process can be gained.

Graphene and single-walled carbon nanotubes (SWCNTs) are promising candidates for a large variety of different applications such as transparent thin-film transistors [25, 26], sensors [27, 28] or energy storage [29, 30]. Introducing nanocarbon materials as a building block for photonic or optoelectronic instruments would allow for a drastic reduction of the device size and improvement of the device performance. To facilitate the implementation, an in-depth understanding of light-matter interaction for these materials is required. Investigating graphene by a combination of Raman spectroscopy and back focal plane imaging would support this issue. The standard production method of SWCNT samples by sonication of aqueous SWCNT-surfactant mixtures is expensive, because of its low dispersion yield. Having a detailed knowledge about the physical processes happening during the sonication step would help bringing the SWCNT sample fabrication to the industrial scale.

In this thesis the following questions and aims are addressed: (i) How can the observed radiation patterns of the graphene Raman G and 2D band be distinguished? (ii) How can the Raman emission that accounts for the polarization properties of the G and 2D band be expressed in a parameter-free microscopic model? Separate from these, a third question is formulated: (iii) How does sonication during different preparation methods of SWCNTs influence the defect density of the nanocarbon material?

The thesis is structured as follows. Chapter 1 deals with the state of the art of the investigated emitter systems graphene and single-walled carbon nanotubes. In the beginning, general information about graphene including its unique electronic structure is presented. Subsequently, the Raman spectroscopy of graphene will be introduced and the origin of the characteristic peaks will be explained. An emphasis will be put on polarization-dependent Raman spectroscopy of graphene, which is required as background knowledge for chapter 3 (Raman radiation patterns of graphene). The section dealing with SWCNTs is structured in a similar way. It begins with information about the structure and optical properties of SWCNTs. The Raman spectroscopy chapter introduces the significant Raman bands of SWCNTs. In this section, the Raman D/G intensity ratio will be highlighted. This ratio is strongly correlated to the defect density of the sample and can be investigated for quality control. A model is presented that explains the influence of a rising point-defect density on the Raman D band intensity.

In chapter 2, the experimental approach is discussed. Details about the sample preparation of SWCNTs, graphene (exfoliated and chemically-grown) and Au nanorods are presented. The second part of this chapter introduces the experimental microscope setup and lists its components. In a third section, information about the optical technique of back focal plane imaging is given. It is shown, how a radiation pattern is formed in the back focal plane of a microscope objective. Subsequently, the simulation of dipolar radiation patterns according to equations by *Lieb et al.* [22] is demonstrated. The appearance of cal-

culated radiation patterns is discussed for distinct orientations of the point-dipole. In the following the experimental realization of back focal plane imaging is thematised. This subsection addresses the imaging of the back focal plane by a $4f$ configuration, the alignment of the $4f$ configuration and the effect of a background reducing spatial filter in the focus of the microscope tube lens on the radiation pattern. The final section discusses the required properties of a microscope objective for the optimal recording of a radiation pattern.

The achieved experimental results are presented in the following part of the thesis, starting with chapter 3, which addresses question (i) and (ii). It begins with the state of the art about polarized radiation patterns. The simulation of distinctly polarized dipolar radiation patterns and the effect of depolarization, observable for large emission angles, are discussed here. Subsequently, the recorded radiation patterns of the graphene Raman G and 2D signal for the non-polarized and polarized case are presented. The radiation patterns are compared with the simulations of dipolar radiation patterns and discussed in terms of the polarization dependence, reported by *Yoon et al.* [31]. The intensity of the experimental and theoretical patterns with regards to the numerical aperture of the microscope objective are then investigated quantitatively. The influence of depolarization on the intensity for rising numerical aperture and its implication on the 2D/G intensity ratio, crucial for the identification of single-layer graphene, are considered. In conclusion, the fraction of detection for Raman scattering is calculated.

The Raman defect study of recycled SWCNTs (question (iii)) is discussed in chapter 4. It begins with the introduction to the recycling procedure and its purpose for industrial application. Samples of the recycling and the standard process with matching experimental parameters are compared in terms of dispersion yield, average SWCNT length and average defect density by absorption spectroscopy, statistical atomic force microscopy and statistical Raman spectroscopy, respectively. Based on these results, two mechanism occurring simultaneously during the sonication process of SWCNTs are identified.

Finally, the most significant results attained in this thesis will be summarized. In addition, an outlook will be given, presenting ideas for future Raman investigations on the discussed subjects.

Two appendices are attached to the main part of the thesis. Appendix A contains supplementary information on polarized radiation patterns, supporting the investigations presented in chapter 3. An overview of calculated point-dipole patterns for different dipole orientations and polarization directions will be shown and discussed. In addition, the calculation of polarized radiation patterns will be shown in detail. Finally, technical information about the microscope objective and tube lens used for the measurements is listed. Expanding investigations on Raman radiation patterns of graphene (chapter 3) are presented in appendix B. It deals with the influence of antenna-enhancement on the Raman G radiation pattern, which is provided by deposited gold nanorods. After providing background knowledge about optical antennas first experimental results are shown.

Chapter 1

State of the Art

This chapter provides theoretical background about the nanocarbon emitter systems graphene and single-walled carbon nanotubes, necessary for the comprehension of this work's investigations. Each section will give general information about the material, highlighting its structural and optoelectronic properties. The physical processes occurring during Raman scattering will be explained along with the prominent Raman bands appearing in the spectrum of graphene and single-walled carbon nanotubes. For the case of graphene there will be a focus on polarized Raman spectroscopy.

1.1 Graphene

Graphene was isolated for the first time in a simple and reproducible way by Nobel Price winners *Novoselov* and *Geim* in 2004[32]. The fact, that graphene is a quasi 2D, single atomic layer material already sparked the interest of many researchers. However, after the report of fabricating graphene samples by micromechanical cleavage of graphite, the number of graphene-related studies drastically increased. As a direct consequence, many extraordinary properties were quickly discovered or verified experimentally. Exemplary attributes are graphene's high mechanical [33] and thermodynamic stability [34] as well as its unique electronic [35] and optical characteristics [36]. Besides this, a large-scale fabrication of graphene by chemical vapor deposition for industrial and research application was established [37] and improved in terms of reducing the defect density [38]. All these features make graphene an interesting building block for optoelectronic and photonic devices[25, 27, 29, 39, 40, 41, 42, 43, 44].

This section is divided into three parts. The first part will elaborate the electronic structure of graphene. The second part features Raman scattering in general with a highlight on graphene Raman spectroscopy. In the third part polarization-dependent Raman spectroscopy of graphene will be explained.

1.1.1 Electronic Structure

The information provided in this section is based on refs. [45] and [46].

Graphene is composed of sp^2 -hybridized carbon atoms, each forming three covalent σ bonds of 1.42 Å length with its adjacent atoms. The remaining electron in the carbon atom's free p_z -orbital forms a π -bond. In the ensemble, the π -bonds of the carbon atoms are hybridized forming the bonding π and antibonding π^* bands, which are responsible for graphene's electronic properties.

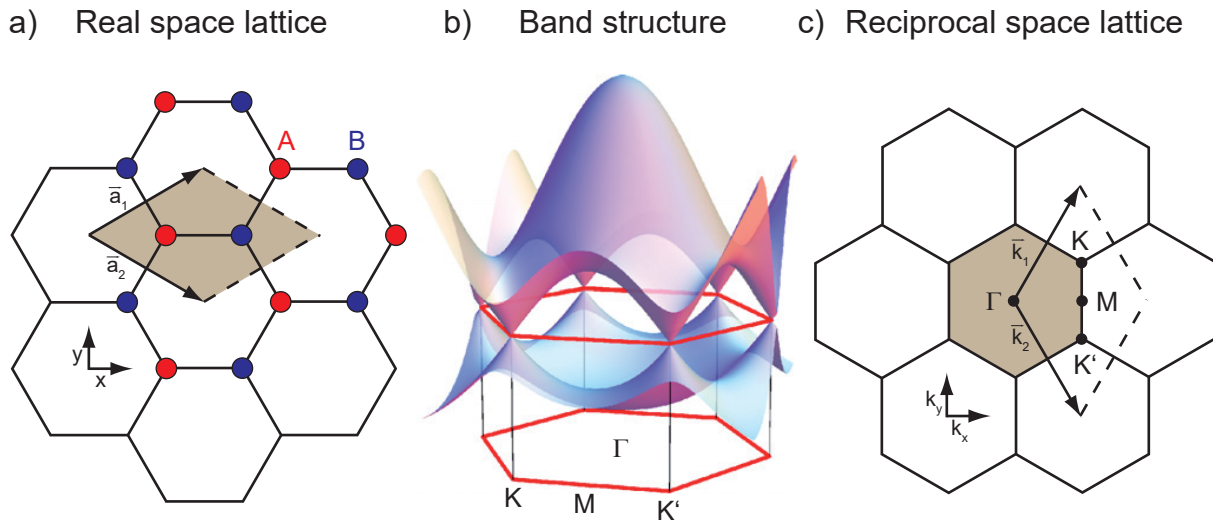


Figure 1.1: a) Real space unit cell of graphene. The real space lattice vectors \vec{a}_1 and \vec{a}_2 define the graphene unit cell (grey shaded rhombus), which contains two carbon atoms, each belonging to two intersecting sublattices, A (red circles) and B (blue circles). b) Full electronic dispersion of the π -bands in the graphene Brillouin zone, showing the trigonal warping effects away from the \mathbf{K} and \mathbf{K}' -points and the saddle point singularity at the \mathbf{M} -point. The equi-energy contour lines of the conduction band are also displayed. c) The first Brillouin zone (BZ) of graphene (grey shaded hexagon) with the high-symmetry points Γ , \mathbf{M} and $\mathbf{K}(\mathbf{K}')$. \vec{k}_1 and \vec{k}_2 are the reciprocal lattice vectors. Figures adapted from refs. [45, 36].

The atoms of the monolayer are organized in a hexagonal lattice, that can be divided into two sublattices, illustrated in fig. 1.1a). The atoms of sublattice A (red circles) and B (blue circles) form intersecting triangle-patterns. \vec{a}_1 and \vec{a}_2 are the lattice vectors, that build the real space unit cell of graphene. Both vectors are positioned with an angle of 60° to each other[47]. The band structure of graphene can be derived from the relationship of the electron's energy E and momentum k . As the motion of the electrons in graphene are confined to two dimensions, also the momentum space is constrained to two dimensions. Based on the tight-binding approximation formulated by ref. [48], the electronic dispersion

in the graphene Brillouin zone can be calculated (see fig. 1.1b). The valence and conduction bands meet at certain points at the edge of the Brillouin zone, the so called Dirac points. This fact effectively makes graphene a zero-bandgap semiconductor or semimetal. The six Dirac points can be divided into two sets of three points, labeled \mathbf{K} and \mathbf{K}' . Due to this graphene exhibits a valley degeneracy of $g_v=2$. This results in a degeneracy of the electronic bands [49, 35, 50, 51]. The dispersion of the bands is linear near the Dirac points. Thus, electrons near the two inequivalent valleys in graphene behave like massless relativistic Dirac fermions with the speed given by the Fermi velocity $\nu_F \approx 10^6 \text{ m/s} = 0.003 \cdot c$ (speed of light). The dispersion relation near the \mathbf{K} points is given by [52]:

$$E_{\pm}(k) \approx \pm \hbar \nu_F |k - K| \quad (1.1)$$

with the Plack constant $\hbar = 6.626 \cdot 10^{-34} \text{ m}^2 \text{ kg s}^{-1}$. Besides the Dirac points other noteworthy highsymmetry points are the Γ point in the center and the \mathbf{M} point in the middle of an edge. These are also illustrated in fig. 1.1c, showing the reciprocal lattice unit cell, which is formed by the reciprocal lattice vectors k_x and k_y . The first Brillouine zone is marked in grey.

1.1.2 Raman Spectroscopy of Graphene

The information provided in this section is based on refs. [45], [53] and [54].

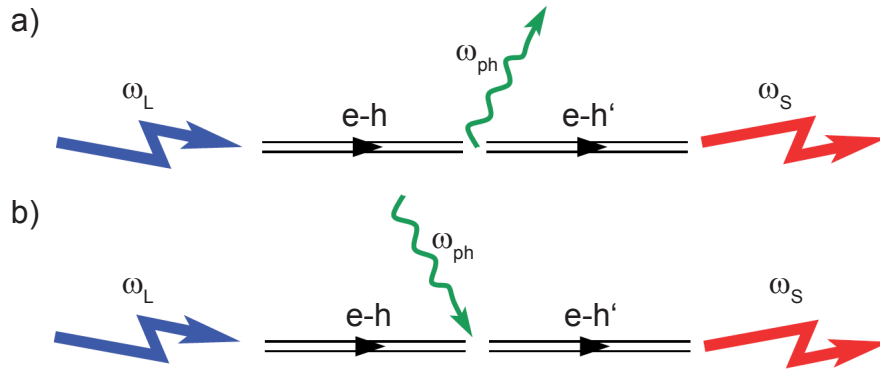


Figure 1.2: Raman Scattering process. a) Stokes: An incoming photon ω_L excites an electron-hole pair e-h. The pair decays into a phonon ω_{ph} and another electron-hole pair e-h'. e-h' recombines, emitting a photon ω_S . b) Anti-Stokes: Equivalent process with the phonon being absorbed by the e-h pair. Figure adapted from ref. [53].

Raman spectroscopy is a non-destructive investigation tool commonly used to study the structure and electronic properties of the sample material. It is one of the most used characterization methods in carbon science and technology [55, 56, 53, 39]. Graphene properties such as layer number [57], defects [58], strain [59, 60, 61, 62] and residual charge impurities [63, 64] can be conveniently identified. Recent publications address the stacking

order and the sheet mis-orientation in bilayer graphene [65, 66]. Raman scattering is defined as inelastic scattering of photons by phonons. The incident photon thereby creates a time-dependent perturbation of the Hamiltonian. As the electronic field of the photon is changing rapidly, only electrons respond to the perturbation. An electron e is excited from the ground state with the energy $E_L = \hbar\omega_L$ and wavevector k_L of the absorbed photon, leaving a hole h at the ground state. The photoexcited electron is subsequently scattered inelastically due to absorption or emission of a phonon with energy $E_{ph} = \hbar\omega_{ph}$ and wavevector q . In the third step, the electron-hole pair e - h' recombines emitting the scattered photon with the energy $E_S = \hbar\omega_S$ and wavevector k_S . These three steps occur almost instantaneously on the femtosecond timescale [45]. Energy and momentum are thereby conserved:

$$E_L = E_S \pm E_{ph} \quad (1.2)$$

$$k_L = k_S \pm q \quad (1.3)$$

The emission of a phonon into the material has the consequence of reducing the energy of the scattered photon by E_{ph} (*Stokes process*, see fig. 1.3a, c, d). When the incident photon finds the system in an excited vibrational state due to the absorption of an already present phonon, the scattered photon can leave the system with energy increased by E_{ph} (*anti-Stokes process*, see fig. 1.3b). The phonon population n determines the probability of the Stokes and anti-Stokes process. n is given by the Bose-Einstein-distribution (eq. 1.4):

$$n = \frac{1}{e^{E_{ph}/k_B T} - 1} \quad (1.4)$$

with k_B being the Boltzmann constant and T the temperature. As the Stokes process generates phonons, the phonon population is increased. Consequently the anti-Stokes process leads to a reduced phonon population. Therefore, the Stokes process shows a higher probability than the anti-Stokes process. Due to this, measurement of the Stokes process was established as the standard Raman experiment plotting the intensity of the scattered light as a function of the Raman shift (difference between incident and scattered photon energy).

The Raman scattering process can be further classified depending on the incident or scattered photon energy relative to the energy of the electronic transition involving ground state and excited state (see fig. 1.3). The process is classified as *non-resonant* when both E_L and E_S do not coincide with the energy difference between ground and excited state (solid lines). For this case the electron is excited and scattered into short-lived virtual states (dashed lines). In the Stokes process (anti-Stokes process) shown in fig. 1.3b (c) the incident energy E_L (scattering energy E_S) is matching the electronic transition. The processes are labeled as incident resonant (scattered resonant), respectively. A Raman process is double resonant, when both E_L and E_S coincide with the electronic transition (see fig. 3.5d). For a first-order Raman process the enhancement of the Raman intensity by

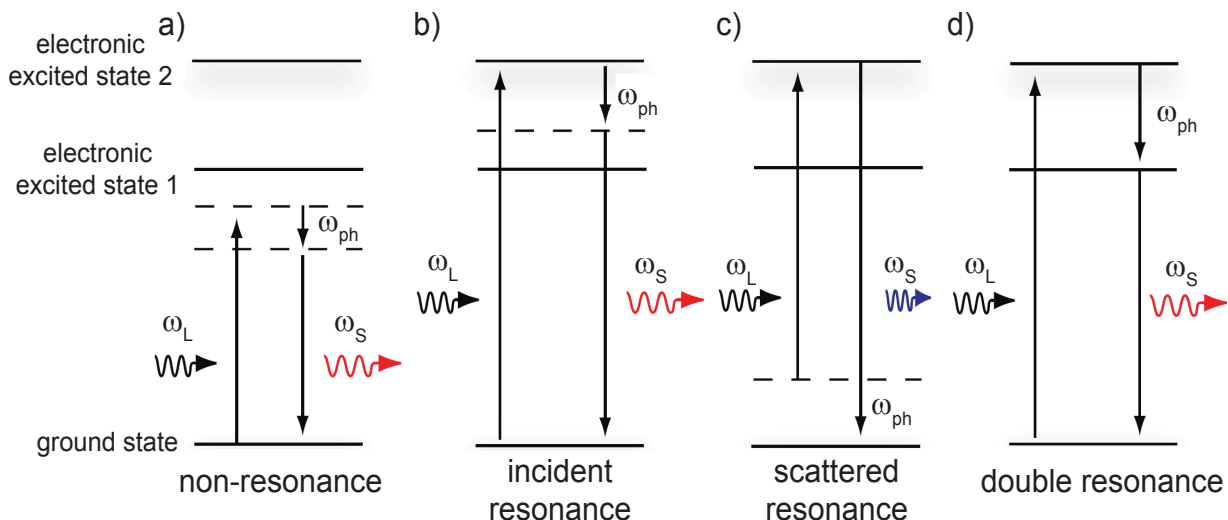


Figure 1.3: Energy level diagrams of Raman scattering processes: a) non-resonant Stokes Raman scattering b) Stokes Raman Scattering: Creation of a phonon c) Anti-Stokes Raman scattering: A phonon is annihilated during the process. The Raman scattering processes in b) and c) are resonant Raman processes with respect to the incoming and scattered light, respectively. d) Double Resonant Raman scattering, where both incoming and scattered light are in resonance with electronic transitions. Dashed lines indicate virtual states, while solid lines correspond to electronic states. Figure adapted from ref. [45].

incident and scattered resonance can be determined from perturbation theory [47]. The Raman signal can be enhanced by up to three orders of magnitude [67].

The measurement of graphene's Raman spectrum [57] was a big step towards understanding the physics of graphene. It was realized, that the Raman mode frequency is influenced by field or chemical doping as well as strain and stress. Other modes only appear in the spectrum when defects are present. An important aspect to understand the Raman spectrum of graphene is its dispersion relation of phonons. Each atom has three degrees of freedom. As there are two inequivalent atoms A and B in the real space lattice (see fig. 1.1a), there are six phonon branches - three optical (O) and three acoustic (A). Four of the phonon modes, two acoustic and two optical, are in-plane(i). The other two modes are out-of-plane (o). The direction of the phonon modes along or perpendicular to the C-C carbon bonds indicates if they are transverse (T) or longitudinal (L). The dispersion relation along the high symmetry points Γ - \mathbf{K} - \mathbf{M} - Γ is depicted in fig. 1.4a. The two phonon modes iLO and iTLO give rise to the relevant graphene Raman signals. Both are highly dispersive at the Γ and \mathbf{K} points.

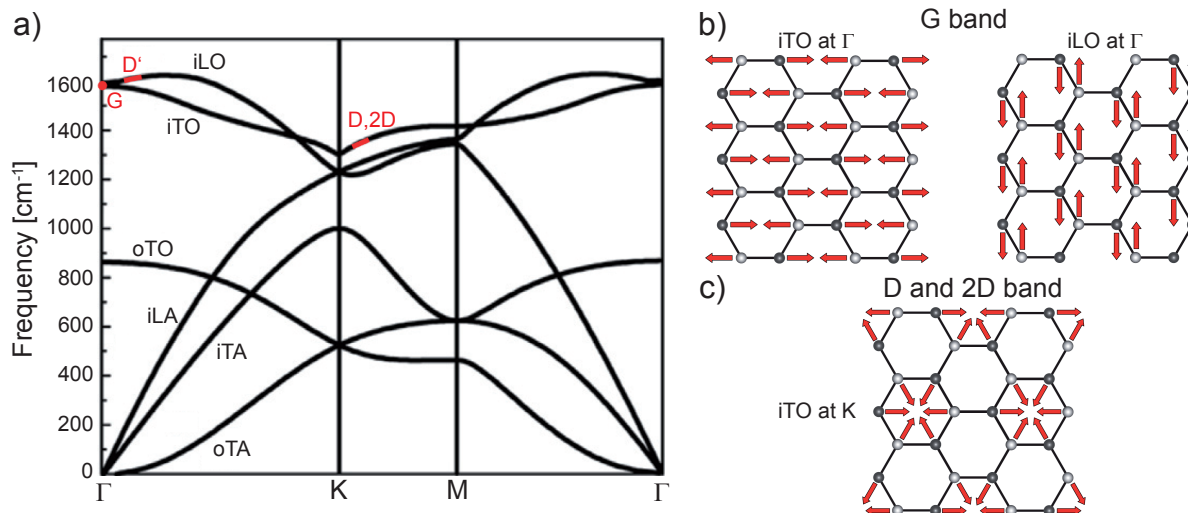


Figure 1.4: a) Phonon dispersion of graphene along the high symmetry lines of Γ -**K**-**M**- Γ of the graphene BZ. The marked positions show the phonons related to the important Raman bands. b) Scheme depicting the vibration modes of the iTO- and iLO-phonons associated with the G band at the Γ point. c) Scheme depicting the vibration mode of the iTO-phonon associated with the D and 2D band at the **K** point. Figures adapted from refs. [54, 68, 69].

Raman scattering can be further categorized by the number of phonons involved in the process. Thereby an n -phonon process exhibits $(n+1)$ intermediate states. The relevant Raman signals discussed in literature are 1- or 2-phonon processes. The order of the scattering process is defined as the position of the scattering event in the sequence of total scattering events [47, 67]. Fig. 1.5a shows the Raman spectrum of pristine (top) and defected (bottom) graphene with the significant Raman signals labeled. The main Raman processes giving rise to those signals are illustrated in fig. 1.5b-f.

The G Signal

The Raman G band ($\sim 1580 \text{ cm}^{-1}$) is a double degenerated in-plane C-C stretching mode which can be assigned to the E_{2g} symmetry group [70]. Fig. 1.4b depicts the signal's two stretching modes associated to iTO and iLO phonons. The signal arises from a first-order ($q=0$) one-phonon process at the Γ point (see fig. 1.5b). The incident photon excites an electron-hole pair. One of the two charge carriers is scattered by a phonon and subsequently recombines, emitting a photon. The G signal exhibits a Lorentzian lineshape due to the lifetime broadening between the energy levels [59, 71, 61].

The D and D' Signal

The D band vibration can be depicted as an in-plane breathing mode of the carbon rings featuring A'_1 symmetry (see fig. 1.4c). The second-order, double-resonant D band process starts with an inter-valley scattering of a photoexcited electron by an iTO phonon

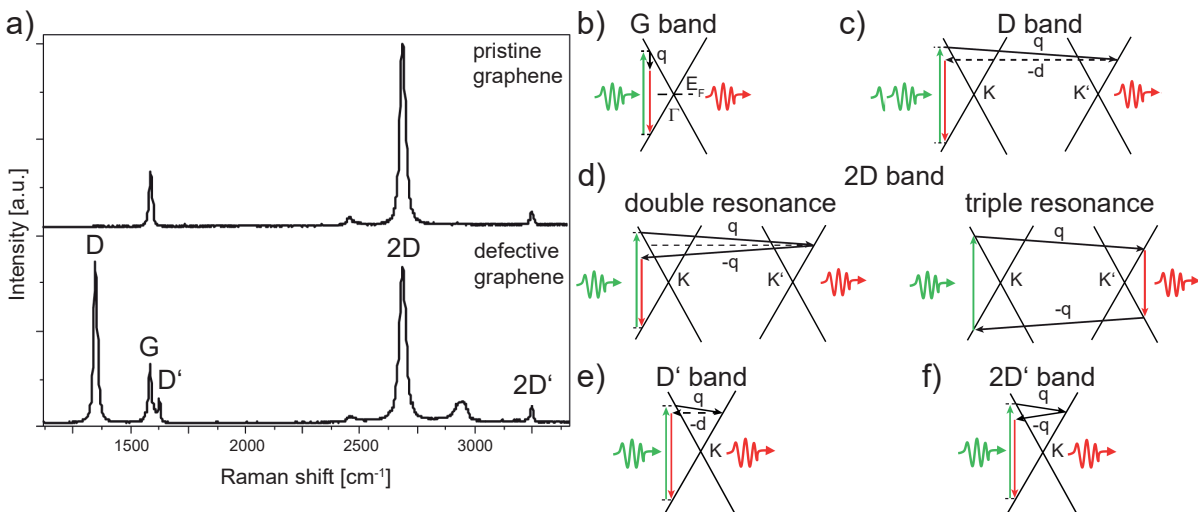


Figure 1.5: a) Raman spectra of pristine (top) and defected (bottom) graphene with labeled peaks, b-f) Scheme of the main Raman processes in graphene giving rise to the depicted Raman signals: b) G band process, c) double-resonant D band process involving scattering at a defect (horizontal dotted line), d) second-order 2D band process, which is either double (left) or triple (right) resonant, e) intravalley double resonant D' band process, f) intravalley double resonant 2D' band process. Wave arrows depict the incident (green) and scattered (red) photons. Solid arrows depict the phonon momentum. Figure adapted from ref. [54].

around the \mathbf{K} (\mathbf{K}') point. To conserve momentum, scattering at a defect (horizontal line in fig. 1.5c), that breaks the symmetry of the lattice, is necessary. Possible defects activating the D band are sp^3 defects [72], vacancy sites [73, 74], grain boundaries [75] or the graphene edges [76, 77, 78]. Because of this, the D band signal is only present at graphene edges or other defect sites. This fact is exploited for the determination of graphene quality (see also section 1.2.2). For the case of pristine graphene, central parts are lacking defects to activate the band (see fig. 1.5a, top). After recombination of the electron-hole pair the electron returns to its original location at \mathbf{K} simultaneously emitting a photon. As the process is double resonant its spectral position depends on the excitation energy. Its spectral location is at $\sim 1345 \text{ cm}^{-1}$ for an excitation at 545 nm [79].

In contrast to the D signal, the process of the D' ($\sim 1620 \text{ cm}^{-1}$) can be described as both intra-valley scattering (see fig. 1.5e) or inter-valley scattering (not shown). Thereby both electron or hole can scatter inelastically.

The 2D and 2D' Signal

The 2D signal, historically also named G' signal, is the overtone of the D signal. Like the D band its vibration mode is an in-plane breathing mode of the carbon rings with A_1' symmetry (see fig. 1.4c). The origin of graphene's most intense signal is a second-order, double

resonant Raman process around the \mathbf{K} (or \mathbf{K}') point. The process, depicted in fig. 1.5d, involves two phonons of opposite momentum q and $-q$. The double resonant process (left) is started by a photoexcited electron-hole pair. An iTO phonon inelastically scatters the electron towards the \mathbf{K}' (\mathbf{K}) point, analogue to the D band process. The electron is then scattered back by another iTO phonon to the original Dirac point and radiatively recombines considering energy and momentum conservation. To fulfill momentum conservation the two iTO phonons are required to have opposing momentum. Thus, the 2D signal does not need a defect for its activation [79]. Double resonance thereby refers to the photon (incident or scattered) and the phonon (first or second). For triple resonance (right) both electron and hole are scattered by the phonon radiatively recombine and scatter back to their initial position. Like the D band, the 2D band's spectral position is sensitive to the excitation energy. It is detected at $\sim 2700 \text{ cm}^{-1}$ [79].

The shape and the width of the signal is directly influenced by the layer number. For single layer graphene the signal resembles a Lorentzian lineshape. In presence of a bilayer, the 2D signal is slightly broader due to the 2D band's splitting into four different components at different frequencies. This fact along with the 2D/G intensity ratio ($\sim 4:1$) [57] are an indicator for the identification of single layer graphene.

Equivalent to the 2D band, the 2D' band ($\sim 3250 \text{ cm}^{-1}$) is the overtone of the D' signal and also does not need an activating defect. The scattering process is illustrated in fig. 1.5f.

1.1.3 Polarized Raman Spectroscopy of Graphene

This section provides the background knowledge about polarized Raman Spectroscopy of graphene, necessary for chapter 3. It is based on ref. [31].

Based on theoretical calculations in 2003, *Grüneis et al.* stated, that optical absorption in graphite is proportional to $|\pm (\vec{P} \times \vec{k}) \cdot \hat{n}|^2$, with \vec{P} being the polarization of incident light, \vec{k} the wave vector of the electron momentum localized near the \mathbf{K} -point and \hat{n} the unit vector orthogonal to the graphene plane [80, 81]. Thus, the term restricts the polarization to the graphene plane. The optical absorption of polarized light is absent for $\vec{P} \parallel \vec{k}$ and maximal for $\vec{P} \perp \vec{k}$. This circumstance is expressed as a node in the amplitude of the transition matrix element for optical absorption. This nodal structure of the absorption coefficient is unique for graphene. Other materials exhibit a quadratic low energy dispersion relation for electrons.

The node structure can not be observed by simple absorption spectroscopy as optical absorption does not generally select the electron wave vector k , but averages all electron momenta contributing to the process instead [80]. k selection can be achieved by absorption spectroscopy on a graphene nanoribbon (finite width) [82] or at graphite edges (one-dimensional character of defect) [76].

Alternatively specific k can be selected via the 2D Raman process, that involve nodal electron-photon interaction and anisotropic electron-phonon interaction [83, 84]. This translates into a process shown in fig. 1.6a. An electron with momentum k is excited by incident light with the polarization P and is inter-valley scattered by a phonon. After the scattering event, an electron with the momentum k' recombines with a hole while emitting the scattered photon with a specific polarization[80]. The directions of k , k' and P to the line connecting the \mathbf{K} and \mathbf{K}' point can be described by the angles θ , θ' and α , respectively.

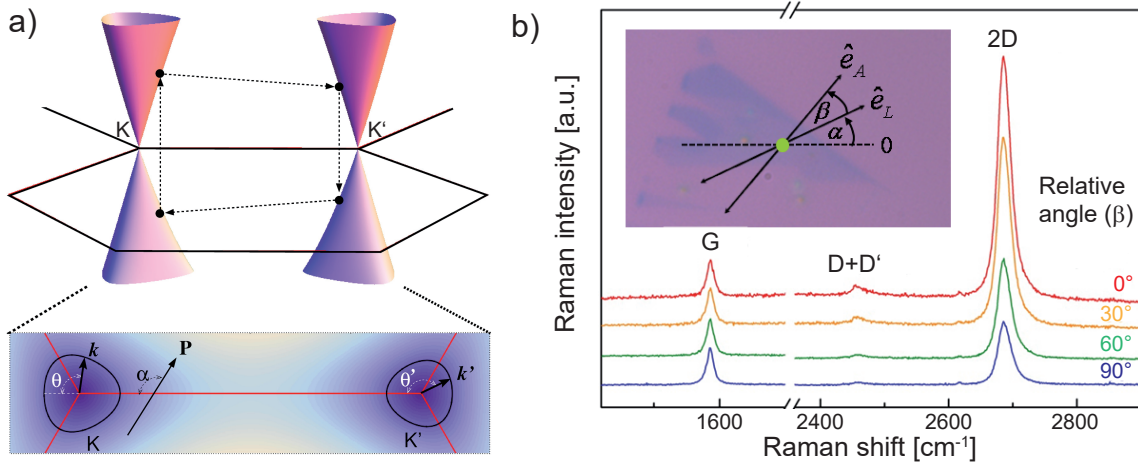


Figure 1.6: a) Scheme of the 2D Raman process: An incident laser beam excites an electron near the \mathbf{K} -point with momentum k at the left cone and is scattered to the state near the \mathbf{K}' -point with momentum k' at the right cone. An iTO phonon with momentum $k-k'$ is emitted. θ (θ') expresses the angle between electron momentum k (k') and the $\mathbf{K}-\Gamma$ direction. The angle enclosed by the laser polarization and the $\mathbf{K}-\Gamma$ direction is depicted as α . b) Polarized Raman spectra obtained for a fixed excitation polarization \hat{e}_L and a varied analyzer polarization \hat{e}_A . The orientation of both polarizations relative to the edge of the graphene flake is described by the respective angles $\alpha=0$ and β . The 2D band intensity varies for different angles β , while the G band intensity is invariant. Figure adapted from ref. [31].

The consequence of this theory is a strong polarization-dependence of the 2D Raman process. This was experimentally verified via Raman spectroscopy with polarized detection (see fig. 1.6b). The relative angle between laser polarization (unit vector \hat{e}_L) and analyzer polarization (unit vector \hat{e}_A) is defined as β . The measured spectra exhibit varying 2D signal intensities $I(2D)$ for different β . The signal is maximized for parallel excitation and detection polarization ($\beta = 0^\circ$) and minimal for the perpendicular case ($\beta = 90^\circ$). Thereby, the laser polarization relative to the graphene lattice expressed by the angle α does not influence the signal intensity. The (D+D') band shows the same behavior. In contrast to both, the Raman G band signal intensity $I(G)$ stays constant for all β and thus is polarization independent.

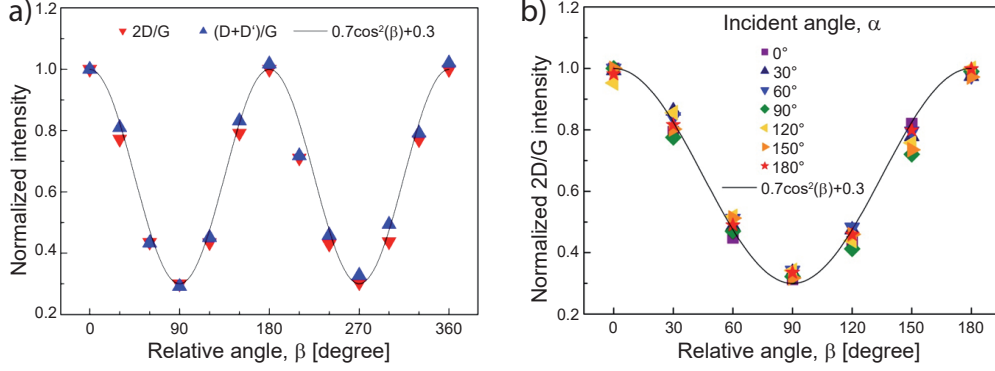


Figure 1.7: a) Raman 2D and (D+D') signal intensities normalized to the polarization independent Raman G band as a function of the polarization of the scattered light, b) Normalized 2D/G intensity ratio as a function of the relative angle β measured for different incident polarization α . Regardless of α , the normalized intensity shows the same dependence on β . Figure adapted from ref. [31].

The experimental data for increasing β over the full range of 2π is illustrated in fig. 1.7a. The polarization independence of the Raman G band is utilized by normalizing $I(2D)$ to $I(G)$, thus excluding experimental artifacts. The graph shows a curve shape following the cosine function with minima at $\beta = 90^\circ$ and 270° and maxima at $\beta = 0^\circ$, 180° and 360° . The (D+D') follows the same trend, indicating that it is subjugated to the same double resonant process leading to its dependence on polarization. Variation of incident laser polarization for different detected polarizations all result in the same trend for Raman 2D scattering (see fig. 1.7b), proving that the change of $I(2D)$ only depends on β . These experimental results prove the polarization dependence of the Raman 2D process and suggest, that the polarization directions of the incident and scattered photons are parallel.

The polarization isotropy of the G signal is explained by group theory. The graphene G band signal shows E_{2g} symmetry, which can be seen from the movement of the carbon atoms (see fig. 1.4c) [85, 86]. For incoherent scattering $I(G)$ thus can be calculated according to

$$I(G) \propto \sum_{i=1}^2 |\hat{e}_S \cdot R_i \cdot \hat{e}_L|^2 \quad (1.5)$$

where R_1 and R_2 are the double degenerate E_{2g} Raman polarizability tensors for the E_{2g} symmetry [85, 86]:

$$R_1(G) = \begin{pmatrix} f & 0 & 0 \\ 0 & -f & 0 \\ 0 & 0 & 0 \end{pmatrix}; R_2(G) = \begin{pmatrix} 0 & f & 0 \\ f & 0 & 0 \\ 0 & 0 & 0 \end{pmatrix} \quad (1.6)$$

and \hat{e}_L (\hat{e}_S) the unit polarization vector of the incident (scattered) light [86]. With $\hat{e}_L = (\cos \alpha, \sin \alpha, 0)$ and $\hat{e}_S = (\cos \gamma, \sin \gamma, 0)$ the intensity components for the parallel and perpendicular po-

larization constellations depending on α and γ can be determined. Thereby γ is the angle between the analyzer polarization and the graphene edge. Entering these informations into eq. 1.5 results in $I(G)=I_{\parallel}[\cos^2(\alpha + \gamma) + \sin^2(\alpha + \gamma)]=I_{\parallel}$, with I_{\parallel} being the Raman intensity when excitation and detection are parallel. Thus $I(G)$ neither depends on the polarization of incident light nor on the polarization of scattered light.

The origin of the Raman 2D intensity variation for different β is the interplay between the photon-electron interaction and the electron momentum dependent anisotropic electron-phonon interaction in graphene. The polarization dependence of the 2D band can be comprehended by calculation of the transition matrix elements for the absorption and electron-phonon scattering process. The differential cross-section of the 2D Raman scattering process is proportional to $|K_{ea}^{\lambda'\lambda}(E_e, E_a)|^2$, with E_e and E_a being the energies of incident and scattered photons with polarizations λ and λ' respectively. $K_{ea}^{\lambda'\lambda}$ is the appropriate high-order matrix element of the interaction between the electromagnetic field and graphene [87, 88, 83, 84, 89], which is calculated via a tight-binding approximation using a nonorthogonal single-orbital basis set for carbon π -orbitals [83, 84, 90].

The frequency of the Raman 2D signal in dependence of E_a and E_e can be expressed as $\omega_{2D} = 2\omega_{iTO} = (E_a - E_e)/\hbar$, with ω_{iTO} being the frequency of the iTO phonon. The energy of the electrons with momentum k after excitation with a 514.5 nm Ar ion laser is determined by $E^c - E^v = 2.41$ eV, with E^c representing the conduction band and E^v the valence band. The contour line thus calculated for k is depicted in fig. 1.6a (left cone). The equivalent calculation for the emission gives a value of 2.09 eV. The corresponding contour line for k' is shown in fig. 1.6a (right cone). With this data the optical transition matrix element for absorption and electron-phonon scattering can be determined.

Fig. 1.8a depicts a contour plot for the calculated optical dipole transition matrix for the process of light absorption as functions of α and θ . The node calculated by ref. [80] can be clearly seen. The probability of absorption, discerned from the contour plot, is highest when the laser polarization P and electron momentum k are perpendicular and lowest when parallel. The equivalent matrix element for the electron-phonon scattering process depending on angles θ and θ' is shown in fig. 1.8b. It shows, that the scattering is maximized for opposing k and k' and zero for the parallel case [91]. Combining both transition matrix elements for the full Raman process and considering polarized detection shows a strong polarization dependence. As can be seen in fig. 1.8c, calculations and experiment are in good agreement. Thereby, the ratio of parallel polarized Raman 2D signal intensity to its perpendicular polarized equivalent was calculated as:

$$r_{2D} = I(2D)_{\parallel}/I(2D)_{\perp} = 3.13 \quad (1.7)$$

In summary, the highest probability of a Raman 2D scattering process is obtained for opposing k and k' and P being perpendicular to k and k' . The scattered photon shows a polarization parallel to the incident polarization.

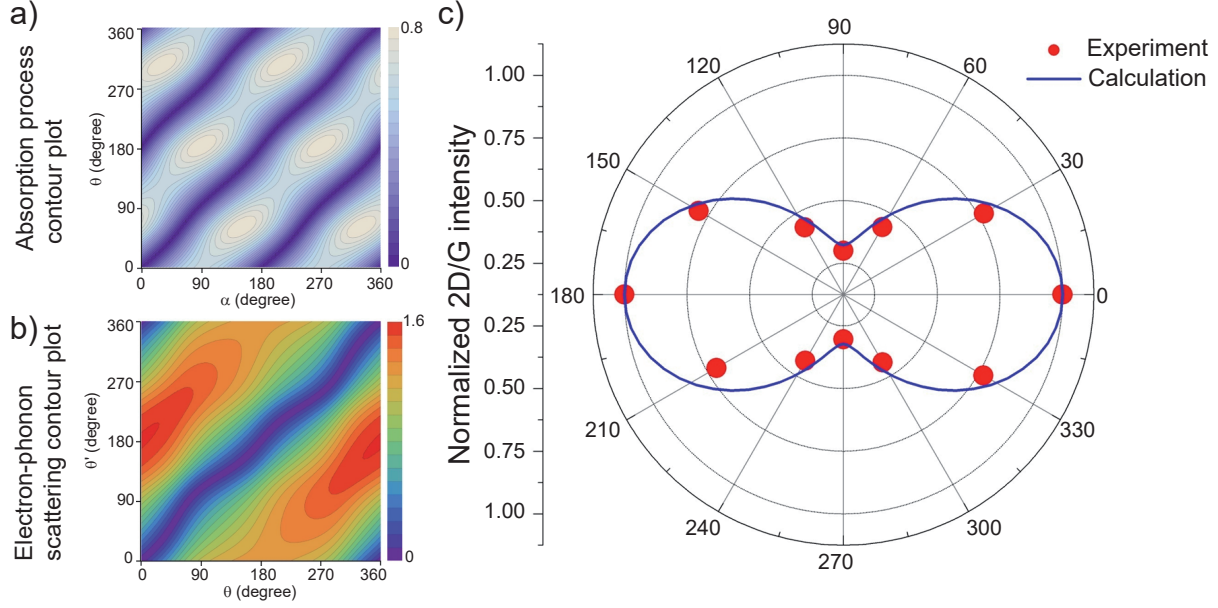


Figure 1.8: a) Light absorption process contour plot (scaling with 10^{-4} eV). The absolute value of the optical dipole transition matrix element is illustrated as functions of θ and α , b) Stokes process contour plot (scaling with 10^{-4} eV). The absolute value of the electron-phonon scattering matrix element as functions of θ and θ' , c) Polar plot of experimental and calculated 2D/G intensity ratio as a function of β . Figure adapted from ref. [31].

Inhomogeneous optical absorption and emission associated with P and k for Raman 2D scattering at single layer graphene was also found for bilayer graphene [31] as well as suspended single layer and bilayer graphene [92].

A simple heuristic model for the calculation of the signal intensities of the polarization-dependent Raman 2D process is shown in the following. It was partially applied for calculations in chapter 3. With the polarization of incident photons $\hat{e}_L = (\cos \alpha, \sin \alpha, 0)$ the absorption matrix element can be expressed as $\sin(\alpha - \theta)$. With the polarization of scattered photons $\hat{e}_S = (\cos \gamma, \sin \gamma, 0)$ the emission matrix element can be calculated by $\sin(\gamma - \theta')$.

Due to the calculations applied for fig. 1.8c, the electron-phonon scattering matrix between two electrons can be approximated. It is proportional to $\sin^2[(\theta - \theta')/2]$. The scattering intensity at an angle γ is given as

$$I(\alpha, \gamma) = \int \int_0^{2\pi} \left| \sin(\alpha - \theta) \sin^4\left(\frac{\theta - \theta'}{2}\right) \sin(\gamma - \theta') \right|^4 d\theta d\theta' \quad (1.8)$$

Considering a projection of the scattered light to an analyzer with a polarization $\hat{e}_A = (\cos(\alpha + \beta), \sin(\alpha + \beta), 0)$ (see fig. 1.6b), the resulting intensity after integrating out all relevant angles can be expressed as:

$$\int_0^{2\pi} I(\alpha, \gamma) \cos^2(\phi - \gamma) d\gamma = \frac{I_{\parallel}}{3} (2 \cos^2 \beta + 1) = I_{\beta} \quad (1.9)$$

where I_{\parallel} is the maximum Raman intensity for the 2D band when \hat{e}_A is parallel to \hat{e}_L ($\beta = 0$ or π) and $\phi = \alpha + \beta$.

1.2 Single-walled Carbon Nanotubes (SWCNTs)

In 1952 *Radushkevich* and *Lukyanovich* reported in a widely unnoticed article about the discovery of microscopic hollow cylinders, consisting of multiple carbon layers, in a transmission electron microscope (TEM) [93]. Decades later, the first single-walled species was observed independently from each other by *S. Iijima* and *Bethune et al.* [94, 95]. The SWCNT can be described as a rolled up layer of sp^2 hybridized carbon atoms with diameters between 0.5 and 50 nm. They can exhibit length in the centimeter range. Because of this rather extreme aspect ratio SWCNTs are often referred to as quasi 1D nanostructures. Their extraordinary optical and electronic properties can be derived from the 1D quantum confinement, making them promising candidates for the application as transparent thin-film transistors [26], sensors [28], photo detectors [96], energy converters and storage [30], LEDs [97].

The next section will present a short overview about structural properties of SWCNTs, followed by a segment about SWCNT Raman Spectroscopy with a highlight on defect density.

1.2.1 Structure

This section is based on refs. [98] and [45].

SWCNTs can be considered as seamless cylinders, that are rolled up from a rectangular stripe „cut out“ from a graphene layer. The roll-up direction of the graphene layer is given by the circumferential or chiral vector \vec{C}_h . The chiral vector \vec{C}_h can be expressed by graphene lattice vectors \vec{a}_1 and \vec{a}_2 as well as their corresponding scaling factors n and m with $n, m \in \mathbb{N}_0$ (see eq. 1.10). The factors n and m are also known as chiral indices, expressing the chirality of the SWCNT as (n, m) . Thereby $n \geq m$ is taken into account.

$$\vec{C}_h = n \cdot \vec{a}_1 + m \cdot \vec{a}_2 \quad (1.10)$$

The construction of a SWCNT from graphene, illustrated in fig. 1.9, is discussed using the example of a (6,5) SWCNT. The edges of the „cut out“ graphene strip are defined by \vec{C}_h (red vector) and the translation vector \vec{T} (black vector). The four corners are labeled O, B, B' and A. The width and height of the SWCNT unit cell can be associated with the length of the two vectors. The strip is rolled up along the roll-up vector \vec{C}_h so that the corner points O and A as well as B and B' coincide, forming the SWCNT unit cell.

\vec{C}_h is connected with the diameter of the SWCNT by:

$$d = \frac{|\vec{C}_h|}{\pi} = a \frac{\sqrt{n^2 + m^2 + nm}}{\pi} \quad (1.11)$$

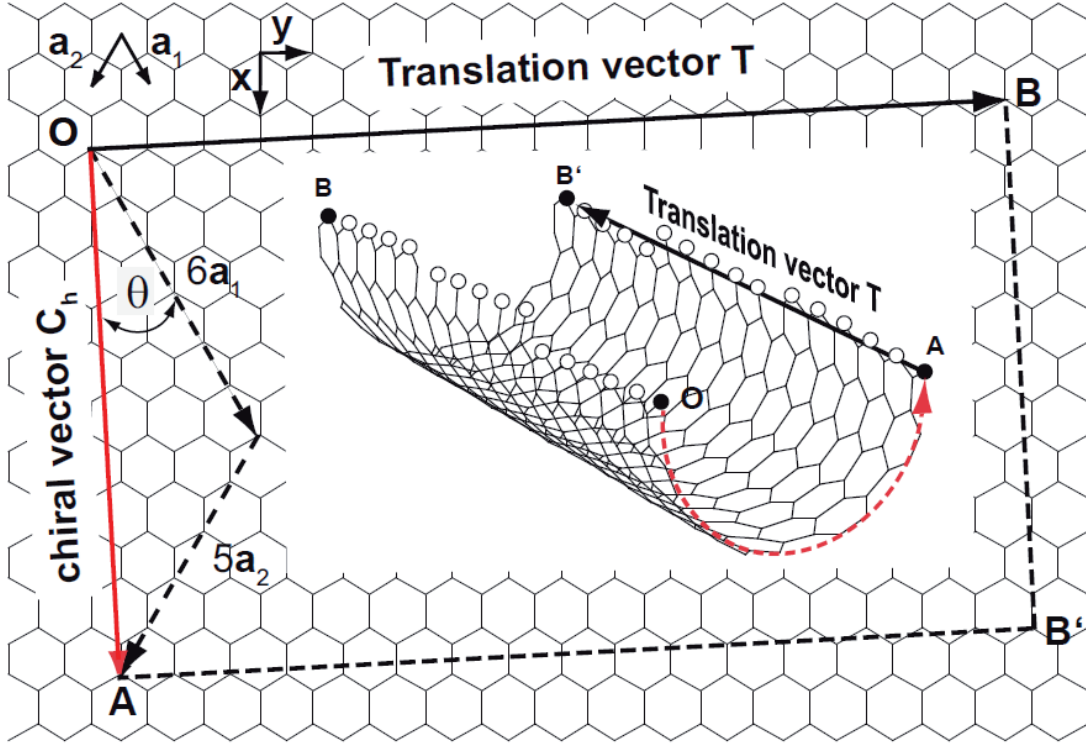


Figure 1.9: Construction of a (6,5) SWCNT unit cell. The unit cell can be constructed by rolling up a rectangular stripe of graphene. The edges of the sheet are defined by the chiral vector \vec{C}_h and the translation vector \vec{T} perpendicular to \vec{C}_h . The chiral vector is defined by the graphene lattice vectors \vec{a}_1 and \vec{a}_2 . For the case of a (6,5) SWCNT: $\vec{C}_h = 6 \cdot \vec{a}_1 + 5 \cdot \vec{a}_2$. Rolling up the rectangular sheet, so that point O coincides with point A and point B with point B, resulting in the quasi-1D cylindrical unit cell of the SWCNT. Figure is adapted from ref. [99, 45]

The directional relation of the chiral vector \vec{C}_h to graphene lattice vector \vec{a}_1 is given by the chiral angle θ_{Ch} :

$$\theta_{Ch} = \arccos \frac{2n + m}{2\sqrt{n^2 + m^2 + nm}} \quad (1.12)$$

Nanotubes can be categorized into three different groups, distinguished by the relation of their chiral indices:

- armchair nanotubes: $n = m, \theta_{Ch} = 30^\circ$
- zig-zag nanotubes: $n = 0$ or $m = 0, \theta_{Ch} = 0^\circ$
- chiral nanotubes: $n \neq m \neq 0, 0^\circ < \theta_{Ch} < 30^\circ$

The names of the SWCNT categories are derived from the characteristic structural pattern of the graphene stripe's edge. Regarding chiral SWCNTs, one needs to distinguish between the right-handed and the mirrored left-handed form. They can be distinguished via circular dichroism [100]. A separation of both forms in a racemic mixture is attained with different chiral wrapping agents [101].

SWCNTs can be further classified by their conducting behaviour, which can be distinguished by their chiral index as well. This is depicted in fig. 1.10. All circles represent end points of \vec{C}_h with the chirality (n,m) . A SWCNT shows metallic conductivity (black circles), when $(n - m)$ is an integer multiple of three. For all other cases the SWCNT is semiconducting (white circles). Following that rule, all armchair SWCNT are metallic. In the figure metallic SWCNTs are illustrated as black circles.

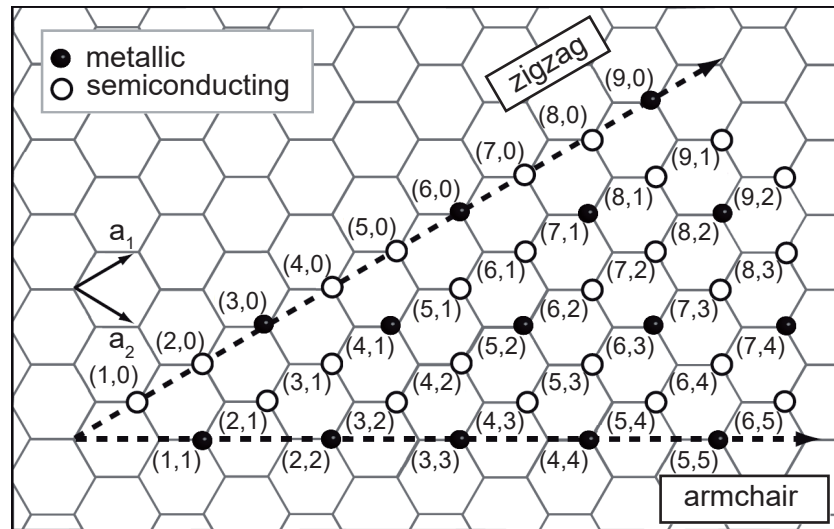


Figure 1.10: The chiral index (n,m) determines whether SWCNTs are metallic (black circles) or semiconducting (white and grey circles). All SWCNTs with the relation $(nm) \bmod 3 = 0$ exhibit metallic properties. This is condition is fulfilled for all armchair SWCNTs with $n = m$. Figure is adapted from ref. [45]

The length of the SWCNT unit cell is given by the translational vector \vec{T} :

$$\vec{T} = \frac{2m + n}{d_r} \vec{a}_1 = \frac{2n + m}{d_r} \vec{a}_2 \quad (1.13)$$

with d_r being the highest common divisor [47].

With the equations for the diameter (eq. 1.11) and the length (eq. 1.13) of the unit cell, the number of graphene hexagons per unit cell N_h can be determined. It is given by the ratio of cylindrical surface area of the SWCNT S_t and the area of a graphene unit cell S_g :

$$N_h = \frac{S_t}{S_g} = \frac{2(n^2 + m^2 + nm)}{d_R} \quad (1.14)$$

The number of carbon atoms per unit cell is given by $2 \cdot N_h$ as each graphene unit cell consists of two carbon atoms.

Optical Properties

Besides displaying photoluminescence at NIR wavelengths due to their direct band gap, semiconducting SWCNTs also show strong Raman scattering. This can be explained by resonance enhancement (see also section 1.1.2).

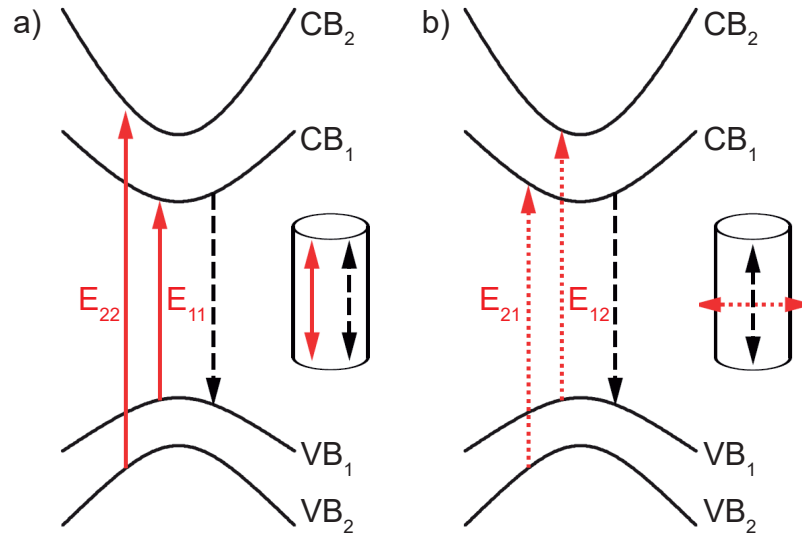


Figure 1.11: Schematics of the SWCNT band structure with a band gap between the highest valence band VB_1 and the lowest conduction band CB_1 . a) scheme depicts the dominant transitions E_{11} and E_{22} (red solid arrows) polarized parallel to the nanotube axis and the emission (black dashed arrow), b) scheme depicts the less prominent transitions E_{12} and E_{21} polarized perpendicular to the nanotube axis. The insets illustrate the orientation of the excitation (red arrows) and emission (black dashed arrows) dipole moments and their orientation with respect to the nanotube axis. Figure is adapted from ref. [102].

The basic emission and absorption properties of SWCNTs can be well approximated by zone-folding of the graphene electronic band structure in the context of a free carrier model [103]. The optical resonances for semiconducting SWCNTs are dominated by excitons. The scheme of the SWCNT band structure can be derived (see fig. 1.11). The E_{11} transition occurs between the highest valence band VB_1 and the lowest conduction band, the transitions connecting the second highest valence band VB_2 and the second lowest conduction band CB_2 is labeled E_{22} . These two predominant optical transitions (red solid arrows) are polarized parallel to the SWCNT axis (see fig. 1.11a). In contrast, the optical transition with unequal indices, are polarized perpendicular to the SWCNT axis (see fig. 1.11b) [102, 104]. Subsequent relaxation mainly occurs from CB_1 to VB_1 (Kasha's rule). The emitted photon (photoluminescence) is polarized along the SWCNT axis, like the absorbed photon (black dashed arrows in fig. 1.11a, b).

1.2.2 Raman Spectroscopy of SWCNTs

This section is based on refs. [45] and [54].

As mentioned before, Raman spectroscopy is a well established method for the characterization of nano carbon material. For SWCNTs, information about specific properties such as phonon dispersion [105], length, type and chirality can be extracted [106].

The resonance conditions are similar to those described before for graphene Raman spectroscopy. Also the processes giving rise to the G, D and 2D bands are equivalent to their counterparts in graphene (see section 1.1.2). The G band (1580 cm^{-1}), observable for all graphitic materials, exhibits a split into the two sub-bands G^+ and G^- [107]. The D band (1350 cm^{-1}), like for graphene, needs a defect for activation. Thus, the defect density can be determined [108]. The 2D band in SWCNTs is usually labeled as G' band ($2600 - 2700\text{ cm}^{-1}$). Due to its vibrational mode the RBM band (radial-breathing mode) is connected to the diameter of the SWCNT.

A SWCNT specific Raman band is the radial-breathing-mode (RBM), observed at $100 - 400\text{ cm}^{-1}$. The symmetric mode is associated to simultaneous vibrations of the carbon atoms in radial direction to the SWCNT axis. It is inversely proportional to the SWCNT diameter d_t . The relation is given by:

$$\omega_{RBM} = \frac{C_1}{d_t + C_2} \quad (1.15)$$

For isolated, semiconducting SWCNTs on an Si substrate, the C parameters are given by $C_1 = 248\text{ cm}^{-1}$ and $C_2 = 0\text{ cm}^{-1}$. This relation is utilized for the determination of the SWCNT chirality. This is achieved by performing resonance Raman experiments, recording RBM intensities for different excitation wavelengths [109].

Defect Density and the $I(D)/I(G)$ Ratio

Disorder in graphene-like materials expresses itself in the form of symmetry-breaking elements in the hexagonal carbon lattice. As a direct consequence, disorder-induced Raman processes are activated, giving rise to the Raman D and D' band (see section 1.1.2 for more details on the process). With the D band intensity $I(D)$ being stronger than $I(D')$ signal, probing the $I(D)/I(G)$ ratio is a good measure to characterize the defect density of nanographitic materials. Normalization by the disorder-independent $I(G)$ is necessary to compare different spectra.

The term defect relates to a number of disorders, ranging from structural and electronic perturbations (e.g. carbon vacancy sites, grain boundaries) to adatoms physisorbed on the surface, covalently bound functional groups and edges of the material. Artificial generation and increase of the D band include mechanical deformation (strain, twist) and doping of sp^3 -hybridized carbon atoms (e.g. chemical functionalization). In general, the fabrication and processing of the material has a high impact on the defect density of the material.

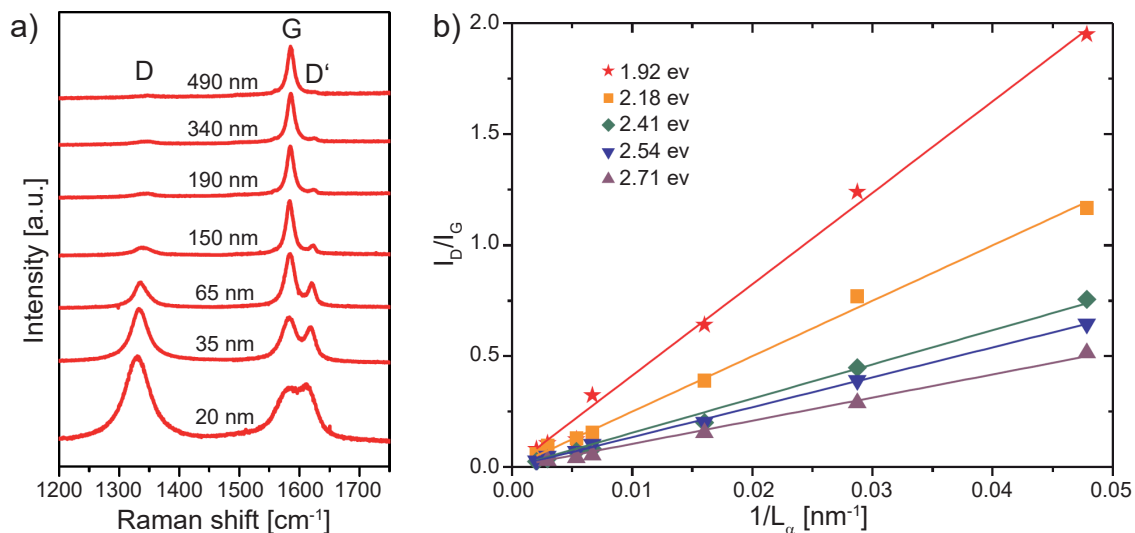


Figure 1.12: a) Raman spectra of nanographite samples with different crystallite sizes L_α recorded with an excitation energy of 1.92 eV. b) Plot of the intensity ratio I_D/I_G for nanographite samples as a function of $1/L_\alpha$ for five different laser excitation energies (see legend). Figure adapted from ref. [110, 54].

When discussing the Raman defect density of nano carbon materials, usually the work of *Tuinstra* and *Koenig* in 1969 is considered [70]. It focuses on the study of crystallite borders. This type of defect can be categorized in the group of one-dimensional defects. By combined x-ray diffraction and Raman studies it was discovered, that $I(D)/I(G)$ is inversely proportional to the crystallite size L_α . The Raman spectra, exhibiting the dependency of disorder-induced Raman D and D' bands on the crystallite size L_α are shown

in fig. 1.12a. The mentioned inverse proportionality between $I(D)/I(G)$ and L_D is clearly shown for varying excitation energies in fig. 1.12b. This dependency was later labeled as Tuinstra Koenig relation[70, 111]:

$$\frac{I(D)}{I(G)} = \frac{C(\lambda_{ex})}{L_D} \quad (1.16)$$

with $C(\lambda_{ex})$ being a coefficient depending on the excitation wavelength λ_{ex} .

The simplest type of defects in nanographitic material is the point-defect. It is highly localized in real space and thus exhibits an extremely broad spatial frequency spectrum. This means, that for reciprocal space they are highly delocalized, thus providing the extra momentum necessary to fulfill the selection rule in one-phonon processes ($q \approx 0$). *Lucchese et al.* systematically increased the amount of point-defects by Ar^+ bombardment of single layer graphene [73]. The defect density n_D was subsequently determined by scanning tunneling microscopy (STM).

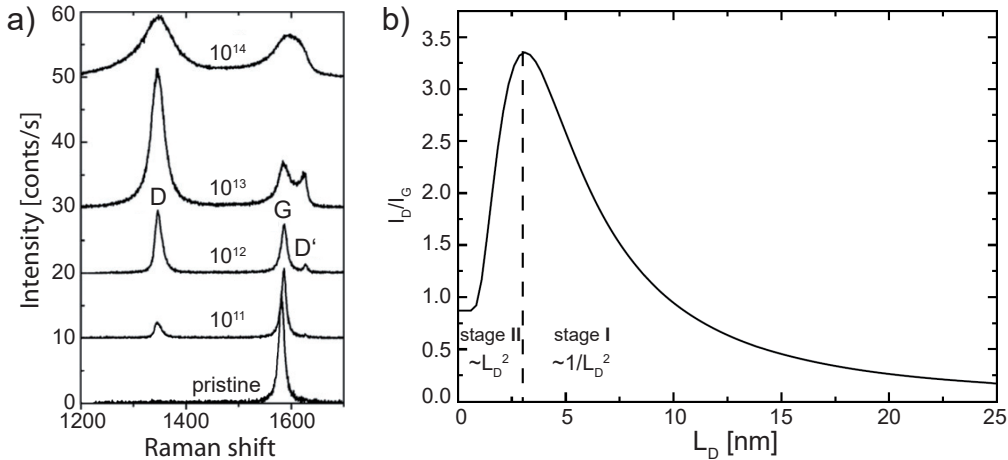


Figure 1.13: a) Raman spectra of SLG samples exposed to Ar^+ ion-bombardment with distinct ion doses. The data were obtained with an excitation energy of 2.41 eV. The ion doses (in units of $\text{Ar}^+ \text{cm}^{-2}$) are indicated next to each respective spectrum, b) The plot I_D/I_G as a function of the average distance between point defects L_D for samples exposed to distinct Ar^+ doses. Figure adapted from ref. [73, 54].

Fig. 1.13a shows Raman spectra of Ar^+ bombarded graphene for increasing ion doses. The spectrum of graphene (bottom) before the bombardment indicates, that there are almost no defects present. The activation of the D and D' band due to the bombardment is clearly visible. With increasing ion doses the D/G intensity ratio increases appropriately. The last spectrum (top) depicts highly disordered graphene, that is close to amorphization, which is reflected in the broadened peaks. In fig. 1.13b the I_D to I_G ratio depending on the average distance between defects L_D is plotted, quantifying the degree of disorder. As can

be seen, I_D/I_G first significantly increases peaking at ~ 4 nm and subsequently decreases. For the dependency of I_D/I_G to the crystallite size L_α , two ranges can be distinguished [55]: A low-disorder (stage I) with $I_D/I_G \sim 1/L_D^2$ and a high-disorder regime (stage II) with $I_D/I_G \sim L_D$.

The mechanism, that gives rise to these two stages, is illustrated in the D band activation model in the inset of fig. 1.14a [73]. The model suggests, that the ion impact on graphene generates two different affected areas. The smaller area S (red) with radius r_S is structurally disordered upon impact. Area A (green) is constructed by the radius r_A subtracted by area S. Within this zone, photoexcited electron-hole pairs are close enough to the defect site for the defect-induced Raman process to be activated. To put it another way, only electron-hole pairs inside area A are able to reach the defective site during the time interval of the Raman process. Thus, $r_A - r_S$ corresponds to the correlation length of photoexcited electrons, that participate in the double-resonance process generating the D band.

The activation model is supported by stochastic simulations corresponding to increasing degree of disorder (see 1.14a-d). The resulting images were calculated for the same ion doses used for the measurement of the top four Raman spectra of fig. 1.13a [73]. The D-activated area, covered in green, increases with rising disorder until a maximum value (compare 1.14a-c). This corresponds to the increasing I_D/I_G ratio in the three middle spectra (bottom to top). The top spectrum shows a decrease of I_D/I_G . This is in agreement with the simulation in fig. 1.14d, where area A is being replaced by area S. The results of the calculation (solid line in fig. 1.13b) thus fit with the experimental data.

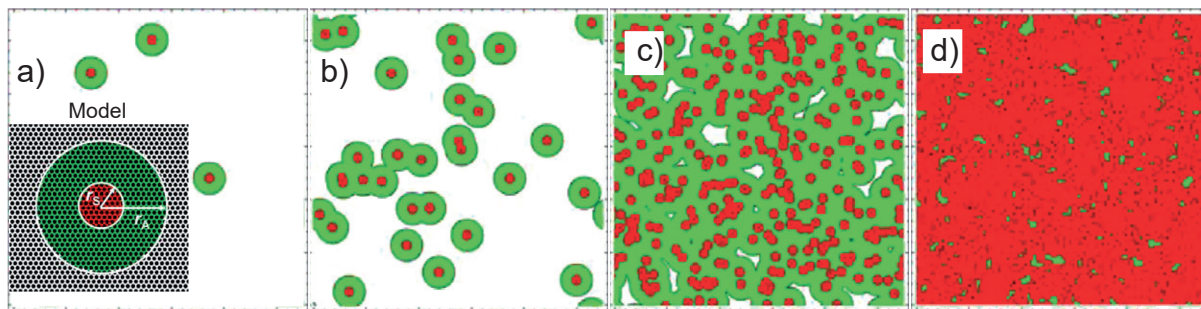


Figure 1.14: Simulation of point-defects created by the impact of an ion on the graphene sheet featuring two distinct regions: the activated A-region (green), and the structurally disordered S-region (red). The respective radii r_A and r_S are measured from the ion impact point. a) - d) Snapshots of the simulation for the structural changes in the graphene layer of different defect concentrations: a) $1011 \text{ Ar}^+ \text{ cm}^{-2}$; b) $1012 \text{ Ar}^+ \text{ cm}^{-2}$; c) $1013 \text{ Ar}^+ \text{ cm}^{-2}$; d) $1014 \text{ Ar}^+ \text{ cm}^{-2}$, corresponding to the four top spectra in fig. 1.13a. Figure adapted from ref. [73, 54].

An investigation of the defect density from recycled SWNTs is part of this work (see chapter 4).

Chapter 2

Experimental Approach

This chapter provides details about the sample preparation and their optical investigation from an experimental point of view. In the first part, the fabrication of SWCNT dispersions, Au nanorods and graphene (exfoliated and chemically grown) and their subsequent deposition on a glass substrate are described. In addition, the results of a statistical TEM study on the Au nanorods are shown. In the second part, details about the experimental setup are presented. Setup components are listed and specified. The final part gives experimental insight about back focal plane imaging, an optical investigation technique, that provides information about the angular distribution of radiation. A theoretical description of radiation pattern formation in the back focal plane and their simulation is given. Subsequently, information about experimental realization and requirements for the microscope objective are provided.

2.1 Sample Preparation

For the optical investigation with the laser scanning confocal microscope setup described in section 2.2, the substrate is required to be thin and transparent, because of the high NA objective's low working distance and the setup's backscattering geometry, respectively. As substrate material 130 - 160 μm thick borosilicate glass coverslides (D 263TM) with a refractive index $n_D = 1.52$ at $\lambda_{exc} = 589\text{ nm}$ provided by the companies Marienfeld and Menzel-Gläser was used.

2.1.1 Single-walled Carbon Nanotubes

The SWCNT raw material, used for this work, was fabricated by the chemical vapor deposition (CVD) method involving a cobalt-molybdenum catalyst (CoMoCat [112, 113]). Thereby, CoMoCat SWCNTs are enriched with the (6,5) chirality resonant at $\lambda_{exc} = 565\text{ nm}$, but also contain smaller fractions of (6,4), (8,3) and (9,1) chiralities.

Before the SWCNTs can be deposited on the glass substrate, the raw material needs to be dispersed. Because of its hydrophobic nature, SWCNTs are not soluble in aqueous solutions. In addition, strong van-der-Waals forces between the SWCNT's unpolar side-walls lead to the clustering of SWCNTs. These hydrophobic effects can be counteracted by treatment with surfactants (surface active agents) and sonication in an aqueous solution. In this work, the tensides sodium dodecyl sulfate (SDS) and sodium dodecyl benzenesulfonate (SDBS) act as surfactants. During the dispersion process the tenside molecules enclose the SWCNT in a micelle structure. Thereby their hydrophobic hydrocarbon chain is oriented towards the SWCNT, while their hydrophilic head group associates with the aqueous solution. Sonication leads to the crushing of SWCNT agglomerates into smaller bundles and isolated SWCNTs. Subsequent centrifugation separates dissolved isolated SWCNTs from large SWCNT clusters. Furthermore side products, catalyst remnants and other impurities from the synthesis process are thus removed. A study, depicting the development of a material-efficient method for the fabrication of SWCNT dispersions, discusses the processes regarding the SWCNTs during the sonication step. This work is presented in chapter 4.

Dispersions for this investigation were provided by **T. Ackermann** (University of Stuttgart and Fraunhofer Institute for Manufacturing Engineering and Automation, Stuttgart). They were prepared by sonication of CoMoCat CG200 SWCNTs (0.1 w%) in aqueous SDBS solution (0.2 w%) under ice bath cooling for 2 min (sonicator *Sonopuls HD-3200*, Bandelin) with a power of 100 W and an on/off pulsation rate of 0.5 s/0.5 s. The resulting sample was centrifuged for 20 h at 9krpm (centrifuge *Universal 320R*, Hettich). The solution was separated from the precipitate by decantation. As an additional purification step the centrifuged dispersion was filtered with a 5 μm pore size syringe filter followed by a filtration with a pore size of 1.2 μm . The samples were characterized by absorption spectroscopy (UV/Vis Spectrometer *T80+*, PG Instruments Ltd).

In order to achieve low area coverage for the topographical analysis, glass coverslides were dip-coated up to two times in the diluted SWCNT dispersions (1:19 dilution with 0.2 w% aqueous SDBS solution, no dilution for the case of *dispersion 4*) with a withdrawal velocity of 20 mm/min (dip-coater *KSV Layer Builder*, Biolin Scientific). Tensides, disturbing the topographical analysis, were removed by additional dipping and withdrawal from deionized water. The samples were investigated with an atomic force microscope (*Dimension 3100*, Veeco) operating in tapping mode.

2.1.2 Gold Nanorods

When a plasmonic nanoparticle is photoexcited, a collective oscillation of its free electron gas is stimulated (surface plasmon). As a consequence to the electron movement a local electric field is generated, that can enhance the optical absorption and emission of objects in the vicinity of the plasmonic particle. Thereby, the strength of the enhancement depends on the spectral difference between excitation wavelength λ_{exc} and wavelength of the

plasmonic resonance λ_{res} . By reduction of $|\lambda_{exc} - \lambda_{res}|$, the coupling between the incident light and the plasmon is increased. This results in a stronger signal enhancement due to the plasmon generated electric field [114, 115]. λ_{res} is easily tunable by the geometric shape of the plasmonic particle [114]. Gold nanospheres have a fixed resonance at 530 nm for a radius up to tens of nanometers. Elongation of the nanoparticle in one dimension changes the resonance properties. The resulting nanorod resonance absorbance spectrum shows two peaks, that can be assigned to oscillations along the longer axis (longitudinal mode) and the shorter axis (transversal mode). The resonance wavelength of both modes can be adjusted by varying the nanorod's aspect ratio, which is controllable due to the conditions of the synthesis [116, 114].

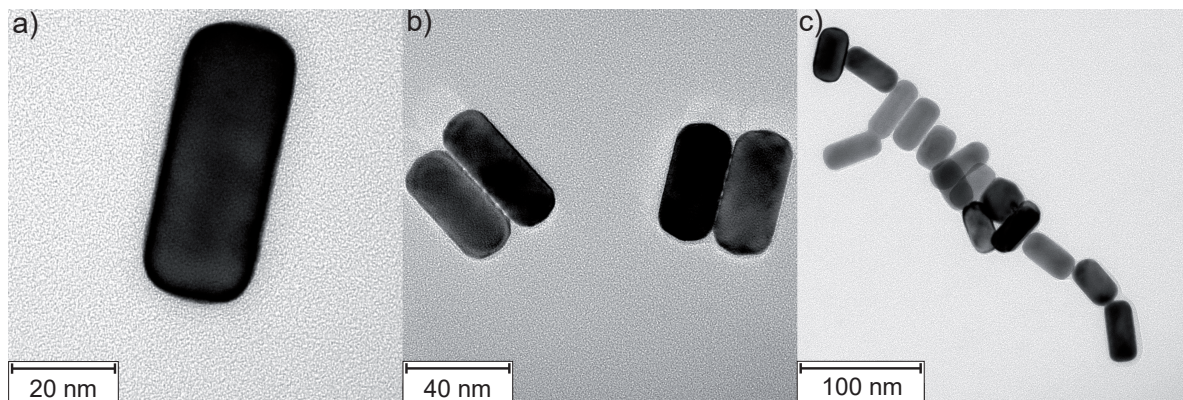


Figure 2.1: Exemplary TEM images of Au Nanorods. TEM image of a) a single Au nanorod, b) and c) Au nanorod clusters.

For the investigation of antenna-enhanced Raman radiation patterns from graphene, nanorods that are resonant at the laser excitation at 632.8 nm on glass were chosen (see chapter B). Gold nanorods with $\lambda_{res} = 630 \text{ nm} \approx \lambda_{exc}$ were synthesized in the group of **Prof. S. Mackowski** (Nikolaus Copernikus University, Torun, Poland). For the synthesis of the precursor, HAuCl_4 (25 mL, 0.05 M), Cetyltrimethylammonium bromide (CTAB) solution (4.7 mL, 0.1 M) and NaBH_4 (0.3 mL, 0.01 M) are stirred for 3 min. NaBH_4 thereby acts as a reduction agent for HAuCl_4 while CTAB stabilizes the resulting Au seeds as a ligand in solution.

In the main process CTAB (150 mL, 0.1 M), HAuCl_4 (1.5 mL, 0.05 M), L-ascorbic acid (1.2 mL, 0.1 M), 0.01 M AgNO_3 (2 mL) and Au seeds (360 μL) are mixed in a water bath at 28 °C for 2 h. Controlled growth of the nanoparticles is ensured by the mild reduction agent L-ascorbic acid. The addition of AgNO_3 decreases the amount of spherical side products. Finally the Au nanorods are separated from the unreacted product by centrifugation (9 krpm, 60 min) and redissolved in water [117, 118].

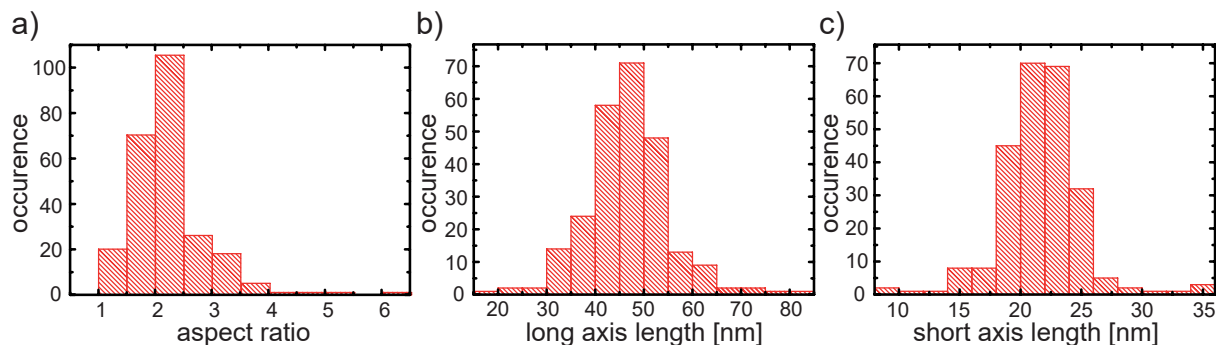


Figure 2.2: Histograms of the 630 nm resonant Au nanorod spatial features, a) aspect ratio, b) long axis, c) short axis.

The nanorods were characterized via transmission electron microscopy (TEM) operated by **Dr. S. Betzler** and absorption spectroscopy. Exemplary TEM images of single nanorods and clusters are shown in fig. 2.1. A total number of 248 Au nanorods were analyzed. Thereby nanorods have an average long axis length of 46.8 ± 8.5 nm and an average short axis length of 21.6 ± 3.3 nm. A mean aspect ratio of 2.2 ± 0.6 was observed. Histograms of both axes and the aspect ratio are shown in fig. 2.2.

In addition, Au nanorods resonating at 780 nm on glass were used as an optical antenna. An analogue statistical TEM analysis of 128 Au nanorods was performed by **R. Ciesielski** (see fig. 2.3). The nanorods exhibit an average long axis length of 41.1 ± 11.4 nm and average short axis length of 19.0 ± 4.65 nm. The observed average aspect ratio has a value of 2.23 ± 0.65 nm.

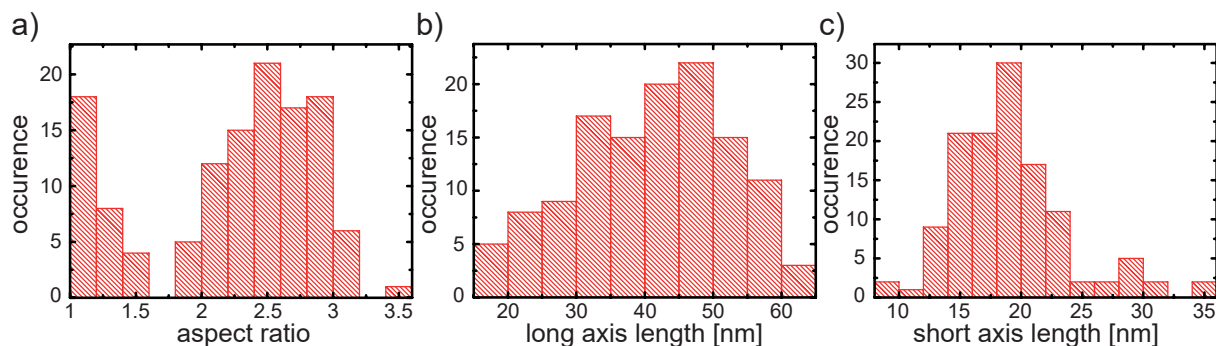


Figure 2.3: Histograms of the 780 nm resonant Au nanorod spatial features, a) aspect ratio, b) long axis, c) short axis.

2.1.3 Graphene

Two differently prepared graphene samples were investigated in this work. Exfoliated graphene exhibits high structural quality, making it adequate for the study of basic graphene properties (see also chapter 3). Usually samples prepared that way are limited in size to flakes of a few microns. For the investigation of enhanced Raman radiation patterns (see also chapter B), the enhancing plasmonic particles need to be deposited on graphene. To statistically increase the chance of localizing a single particle, extended graphene films grown by chemical vapor deposition (CVD) were used.

Exfoliated graphene samples on glass were fabricated in the group of **Prof. A. Ferrari** (Cambridge Graphene Center, University of Cambridge, United Kingdom). Graphene layers are deposited by micromechanical cleavage [32] on Si wafers covered with 300 nm of SiO₂. Single layer graphene (SLG) is identified by a combination of optical microscopy and Raman spectroscopy (Renishaw inVia at 514, 633 nm).[57, 53] SLGs are transferred onto glass by a polymer-based wet transfer process.[40] Poly(methyl methacrylate) (PMMA, molecular weight 950 K) is spin coated onto the substrate where graphite flakes are exfoliated. Then the sample is immersed in deionized water, resulting in the detachment of the polymer film due to water intercalation at the PMMA-SiO₂ interface.[40, 119] The flakes attach to the polymer and can be removed from the Si/SiO₂ substrate. The graphene film attached to the polymer is then placed onto the glass substrate and, after complete drying of the water, PMMA is removed by acetone. Success of the transfer is confirmed both optically and by Raman spectroscopy. No significant D peak is detected after transfer, showing that the process does not result in structural defects.

CVD-grown graphene samples on glass were fabricated by **J. Krauss** of Prof. S. Günther's group (TU München, Germany). For graphene growth ca. 1x1 cm² pieces were cut from as received Cu-foil (25 μm, Alfa Aesar 46986, 99.8%) and loaded into a quartz tube reactor. After evacuating the reactor system (to ~10⁻³ mbar) the Cu-foils were heated up from room temperature to 950°C in a flow of hydrogen (p(H₂)=1 mbar) within 40 min. For oxidative carbon removal the Cu foil was exposed to a highly diluted oxygen flow in an argon carrier gas (p(O₂) = 1·10⁵ mbar in p(Ar) =1 mbar). After 60 min the temperature was increased to 1075°C and the gas flow was changed to graphene growth conditions (p(H₂) = 20 mbar, p(CH₄) = 0.02 mbar) followed by a 2.5 h growth period. Graphene growth was stopped by quickly pulling the Cu-foils out of the hot zone of the reactor.

For the transfer of the as grown graphene films the Cu-samples were spincoated with PMMA solution (6 wt.% in Anisole). After drying the PMMA-protected graphene film was released from the Cu-support by bubbling transfer. This was done by gradually dipping the PMMA-graphene-Cu sandwich vertically into a NaOH-solution (7 g/L) with a platinum counterelectrode. During this dipping a current of ~20 mA is applied with the Cu-sample as cathode. The detached graphene PMMA film is cleaned with deionized water and then transferred onto glass substrates. Finally the PMMA protection layer is removed with

hot acetone.

The following table provides an overview of the samples investigated during the course of this work:

Sample	Fabricator	Chapter
Graphene (exfoliated)	Antonio Lombardo, Ferrari Group (Cambridge Graphene Center, University of Cambridge, United Kingdom)	Chapter 3
Graphene (CVD)	Jürgen Krauss, Günther Group (TU München)	Chapter B
Au Nanorods	Dawid Piatkowski, Mackowski group (Nikolaus Copernikus University, Torun, Poland)	Chapter B
CoMoCat SWCNTs	Thomas Ackermann (University of Stuttgart and Fraunhofer Institute of Manufacturing and Automation)	Chapter 4

2.2 Confocal Microscope Setup

All optical experiments were performed on a confocal microscope [120] in backscattering geometry mounted on an optical table. The sample was mounted on a piezo stage, enabling confocal imaging by rasterscanning and precise positioning of the laser focus at the sample's x,y -plane. Two different excitation wavelengths at 565 nm (confocal imaging of SWCNT networks, supplementary) and 632.8 nm, provided by a semiconductor diode laser and a HeNe gas laser, respectively. The laser's polarization was adjusted via a liquid crystal retarder (LCR), aligned with an analyzer (An). Before coupling the laser beam into the microscope, the beam was expanded consecutively to make use of the full NA of the objective (Obj). Deviations from the laserline in the wavelength regime, resulting e.g. from fluorescence of the laser gain material, were suppressed by a narrow bandpass filter (BP). Stray light was blocked by a 25 μm pinhole (PH₁) acting as a spatial filter.

Inside the microscope, the excitation (green, see fig. 2.4) and detection beampath (red, see fig. 2.4) are separated by a dichroic beamsplitter (BS). Depending on the excitation wavelengths two different beamsplitters were used: The pellicle 33:67 (Thorlabs) was implemented for the excitation wavelength $\lambda_{exc} = 565$ nm and the Z633rdc (Chroma) for $\lambda_{exc} = 595$ nm or 632.8 nm. The latter is retaining $\sim 99.5\%$ of s - and p -polarization, which is important for the polarization-dependent measurements realized in chapter 3. Focusing of the laser and collection of the signal was provided by a high NA oil immersion objective (CFI Planapochromat VC 60x, NA=1.4, Nikon). For experiments, that require a variable NA (see section 3.3), an oil immersion objective with adjustment ring was applied (CFI S-Fluor, NA = 0.5 - 1.3). Polarized detection was achieved by the implementation of an analyzer (An) between beamsplitter and the tube lens (TL), integrated in the microscope. By rotation of the analyzer the desired detected polarization was selected.

Graphene Raman back focal plane imaging required the addition of a 300 μm pinhole (PH_2) at the focus of TL for reduction of background signal consisting of Raman contributions from optical elements and immersion oil. At a distance of $2 \cdot f_{TL} = 400 \text{ mm}$ the Bertrand lens (BL) was added to collimate the beam. The back focal plane image was recorded with a charged coupled device (CCD) camera (Newton DU-920-OE, Andor Technology) at a distance of f_{BL} from the Bertrand lens.

Back focal plane and real space imaging could be selected via a flippable mirror (FM_1). Another flippable mirror (FM_2) separates the beam paths for confocal imaging and spectroscopy. For confocal imaging the signal is focused on the chip of an avalanche photo diode (APD) with L_6 . The signal is converging on the entrance slit of a spectrometer (Shamrock SR-303i, Andor Technology) coupled to a CCD camera (iDUS DU-420A-OE, Andor Technology) via L_7 .

The desired spectral range for confocal and backfocal plane imaging was selected with optical filters. To block the laser signal, a longpass filter, matching the wavelength of the excitation source, is added. Possible positions for the longpass filters, depending on the detection method, are labeled as LP in the sketch of the microscope setup (see 2.4). Analogue, the position of the bandpass filter (700 nm for Graphene and SWCNT Raman G, 760 nm for Raman 2D/G', $\lambda_{exc} = 632.8 \text{ nm}$) are depicted in fig. 2.4.

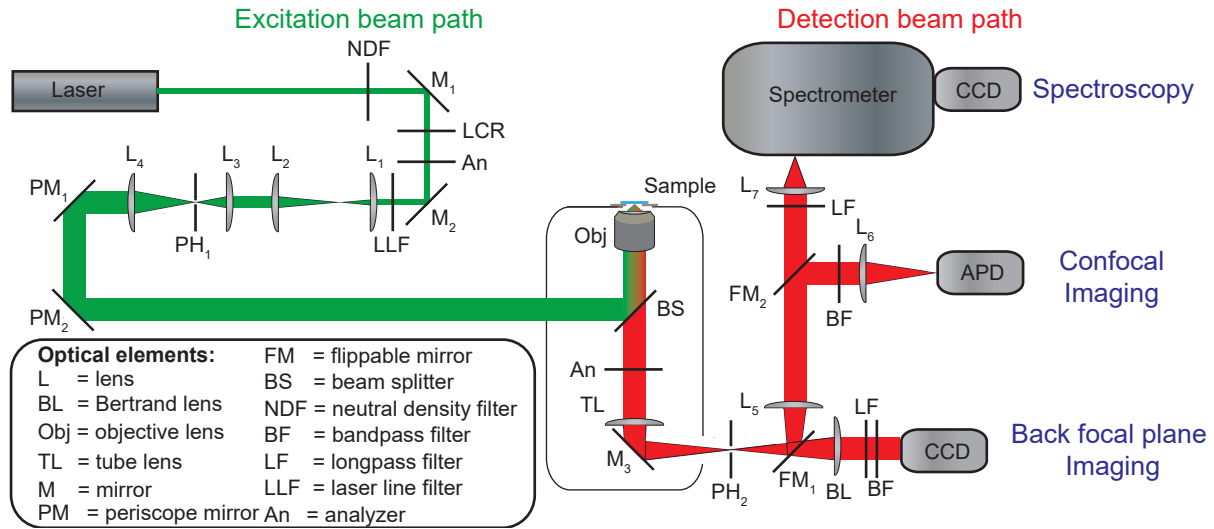


Figure 2.4: Scheme of the confocal microscope setup with excitation beam (green) and detection beam path (red). The detection methods back focal plane imaging, confocal imaging and spectroscopy are labeled accordingly. Abbreviations of utilized optical elements are explained in the key, implemented in the illustration.

The following table shows detailed information about the equipment (e.g. model number, technical data, distributor) used for the optical setup:

Equipment	Distributor
Optical microscope Eclipse TE2000 with TL ($f = 200$ mm) and M_3	Nikon
Objective, CFI Planapochromat, 60x magnification, NA = 1.4, oil immersion	Nikon
Objective, CFI S-Fluor, 100x magnification, variable NA (0.5 - 1.3), oil immersion	Nikon
lenses, $f(L_1, L_3, L_6, L_7) = 30$ mm, $f(L_2, L_4) = 70$ mm, $f(BL, L_5) = 100$ mm	Linus
Pinhole, diameter (PH_1) = $25 \mu\text{m}$, diameter (PH_2) = $300 \mu\text{m}$	Thorlabs
Beamsplitter Pellicle BP133, R[%]/T[%] = 33:67 @ 635 nm	Thorlabs
Beamsplitter Z633rdc, polarization retaining, central wavelength @ 645 nm	Chroma
Neutral density filters	Thorlabs
Silver Mirrors ($M_1, M_2, PM_1, PM_2, FM_1, FM_2$)	Thorlabs
Polarization filter IR 1100 BC4 CW02	CODIXX
Longpass filter LF, LP02-633RU-25, 633 nm Razor Edge [®] , ultrasteep longpass edge filter	Semrock
Longpass filter, 580 nm	Chroma
Bandpassfilter BF, central wavelength @ 700/760 nm, FWHM = 10 nm	Thorlabs
Optical Table	Newport
x,y-piezo stage PI-527	Physik Instrumente
Liquid Crystal Retarder LCR-1-Vis, 450 - 650 nm	Thorlabs
Laser: 632.8 nm HeNe, 35 mW	Thorlabs
Laser: 594 nm HeNe, 5 mW	Thorlabs
Laser: Sapphire 568 nm diode, 50 mW	Coherent
APD: COUNT-250C	Laser Components
APD: PDM-20	Micro Photon Devices
Spectrometer: Shamrock SR-303i	Andor Technology
CCD camera: Newton DU-920-OE (BFP Imaging)	Andor Technology
CCD camera: iDUS DU-420A-OE (Spectroscopy)	Andor Technology

2.3 Back Focal Plane Imaging

Back focal plane imaging is a modern microscopy method, that extracts the angular distribution of the emitted signal at the microscope objective's back focal plane. The obtained intensity map provides information about various material properties like the nature of emissive states (dipolar [22] or multipolar character [121]), the polarization state [122, 24], the coupling of the sample material to the substrate and the surrounding atmosphere [22, 24], the spatial coherence length [123] and the coupling to plasmonic particles (antenna effect) [23, 124, 125].

The following section deals with the question, how radiation is gathered and intensity is distributed in the back focal plane of a microscope objective. Subsequently the calculation of radiation patterns originating from dipolar emitters is presented. The third section provides information about the microscopic imaging of radiation patterns and its experimental realization. Connected to the experimental realization, the final section discusses required properties of the microscope objective for an optimal measurement of radiation patterns. Information in both sections is based on refs. [22, 98, 126].

2.3.1 Theoretical Description of Radiation Patterns in the Back Focal Plane

The radiation of an emitter in a uniform medium with refractive index n_1 depends on the emitters properties. Hence, the medium has no influence on the angular distribution of the radiation. For instance the radiation of a point-dipole in a uniform medium can be seen as the emission of a Hertzian dipole: the radiation exhibits radial symmetry with respect to the dipole momentum \vec{P} . The intensity is strongest for emission perpendicular to \vec{P} .

Most high resolution measurements, however, are performed on a dielectric substrate. The radiation of a dipolar emitter on a dielectric with refractive index n_2 and surrounding medium $n_1 < n_2$ is changed due to the scattering of the emitted photons at the interface. The point-dipole radiates into different areas (see fig. 2.5). The overall power of the radiation P_{tot} can be split into radiation, emitted into the upper halfspace, into the forbidden zone of the lower halfspace, the allowed zone and radiation dissipated into the surface. The radiation fractions are labeled P_u , P_f , P_a and P_n , respectively [127] (see eq. 2.1). The critical angle θ_{crit} with the surface normal allows the differentiation of the allowed and forbidden zone and is given by $\theta_{crit} = \arcsin(n_1/n_2)$. Radiation with an emission angle $\theta < \theta_{crit}$ is assigned to the allowed zone. Light emitted into the forbidden zone fulfills the condition for total internal reflection $\theta > \theta_{crit}$.

$$P_{tot} = P_u + P_f + P_a + P_n \quad (2.1)$$

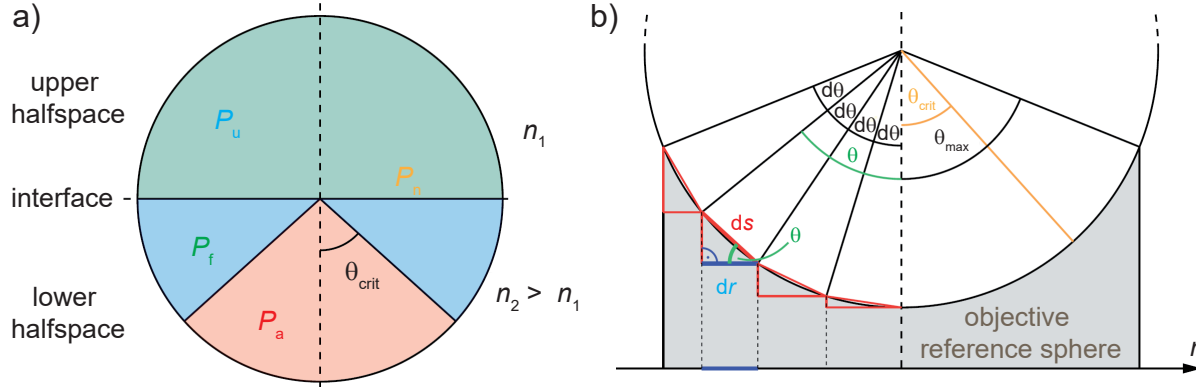


Figure 2.5: a) Illustration of the different angular zones of radiation for the case of an emitter, that is placed on a dielectric substrate. In the scheme the emitter is in the center of the circle. Fractions of the total emitted power P_{tot} are radiated into the upper half-space (P_u), the forbidden zone of the lower half-space (P_f) for $\theta > \theta_{crit}$, and the allowed zone (P_a) for $\theta < \theta_{crit}$. A fourth fraction of radiated power (P_n) dissipates into the surface of the dielectric, b) Scheme illustrating the projection of the angular emission in the allowed zone via an imaging lens onto its BFP. The emitter is in the center of the emission sphere. The critical angle θ_{crit} and maximal collection angle of the lens θ_{max} are illustrated as well. Figure adapted from refs. [98, 115].

This model can be applied to the present microscope geometry (see fig. 2.4). Light emitted into the allowed zone P_a and a fraction of P_f are collected by the microscope objective. For the determination of the intensity distribution in the back focal plane of the objective, which depends on the emission angle θ (see fig. 2.5b), the Weyl representation can be used. It states, that spherical waves, which are sent out by the emitter, decompose into plane waves and evanescent waves [128]. The approximation can be applied for planar microscope objectives [22], that are corrected for the optical aberration of Petzval field curvature [129]. Thus, the intensity distribution in the back focal plane of the microscope objective is related to the emitting electrical field E_{emit} . This is given by:

$$I_{BFP} \propto \frac{1}{\cos \theta} |E_{emit}|^2 \quad (2.2)$$

Fig. 2.5b illustrates the projection of the emission in the allowed zone onto the BFP of the microscope objective. Same amounts of power are radiated into equally sized angular zones $d\theta$, captured on ds of the objective and projected onto the area dr of the BFP. With increasing emission angle θ , same amounts of power are concentrated in decreasing dr . The apodization factor $\frac{1}{\cos \theta}$ corrects for this, thus ensuring the conservation of energy during the projection onto the BFP [22]. This dimensionless term is derived from the trigonometric relation $dr = \cos \theta ds$ (see fig. 2.5b).

2.3.2 Simulation of Dipolar Radiation Patterns in the Back Focal Plane

The radiation of a point-dipole, described by the Hertzian dipole model, is altered when placing the emitter on a dielectric substrate and bringing it into the focus of a high NA microscope objective. First mathematical descriptions of a single dipole on a dielectric medium were developed almost 100 years ago by *Sommerfeld*, *Hoerschelmann* and *Weyl* [130, 131, 128, 132]. The predicted radiation patterns were experimentally verified in 1984 by *Fattinger* and *Lukosz* [133]. Further calculations for this geometry by *Lieb et al.* allowed the simulation of radiation patterns for arbitrary point-dipole orientations \vec{P} [22]. In this section the theoretical steps, formulated by *Lieb et al.*, are presented and dipolar radiation patterns, calculated that way, are described.

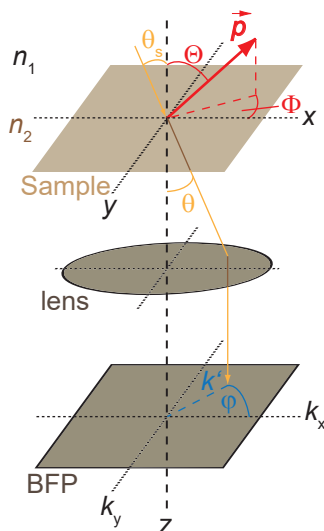


Figure 2.6: Schematic of the geometry used for the calculation of dipolar radiation patterns at an interface. A point-dipole with the orientation \vec{P} , described by the azimuthal angle Φ and the polar angle Θ , is situated on an interface with the refractive index n_2 . The surrounding medium exhibits a refractive index n_1 . The angular distribution of the dipolar radiation is projected onto the BFP of the microscope objective. The emitted light transmits the BFP at a point determined by the radial distance k' and the azimuthal angle in the back aperture ϕ . Both are in relation with the emission angle θ . Figure adapted from ref. [22].

Fig. 2.6 shows a model describing the geometry and the involved parameters for the situation at hand. The dipole orientation \vec{P} can be expressed by the in-plane (azimuthal) angle Φ and the out of plane (polar) angle Θ . The emitter is surrounded by a medium with refractive index n_1 on top of a substrate with n_2 . The dipole is excited with the incident angle θ_S with respect to the substrate normal parallel to the optical axis z . Light is emitted

with an angle θ with regards to the surface normal in direction of z . Both incident and emission angle are in correlation with Snell's law:

$$n_1 \sin \theta_S = n_2 \sin \theta \quad (2.3)$$

According to this, complex values are allowed for θ_S . After the collection by an imaging lens, the ray is projected onto the lens' BFP. Its position in the BFP can be expressed by the azimuthal angle ϕ and the radial distance from the center k' . The relation between emission angle θ and the k -vector coordinate system in the BFP can be expressed by:

$$|k'| = 2\pi \frac{n_2}{\lambda} \sin \theta = k_0 n_2 \sin \theta; \quad \begin{pmatrix} k'_x \\ k'_y \end{pmatrix} = \begin{pmatrix} \cos \phi \\ -\sin \phi \end{pmatrix} \cdot |k'| \quad (2.4)$$

By adaption of this information with eq. 2.2, the intensity distribution of a single dipole in the BFP can be given by:

$$I_{dipole}(\theta, \phi) \propto \frac{1}{\cos \theta} (E_p E_p^* + E_s E_s^*) \quad (2.5)$$

An arbitrarily polarized plane wave can be expressed as a superposition of two orthogonally polarized plane waves. E_p and E_s are the E-field components perpendicular and parallel to the plane of incidence (plane formed by the incident ray and surface normal) with $\vec{E} = \vec{E}_s + \vec{E}_p$. p and s stand for the german words "parallel" and "senkrecht" (perpendicular) and refer to the plane of incidence. Upon the reflection or transmission at an interface, the polarizations s and p are conserved[134].

E_p and E_s are expressed as:

$$E_p = c_1(\theta) \cos \Theta \sin \theta + c_2(\theta) \sin \Theta \cos \theta \cos(\phi - \Phi) \quad (2.6)$$

$$E_s = c_3(\theta) \sin \Theta \sin(\phi - \Phi) \quad (2.7)$$

The c coefficients are given by:

$$c_1(\theta) = n^2 \frac{\cos \theta}{\cos \theta_S} t^p(\theta_S) \Pi(\theta_S) \quad (2.8)$$

$$c_2(\theta) = n t^p(\theta_S) \Pi(\theta_S) \quad (2.9)$$

$$c_3(\theta) = -n \frac{\cos \theta}{\cos \theta_S} t^s(\theta_S) \Pi(\theta_S) \quad (2.10)$$

with

$$\Pi(\theta) = e^{ik_0 n_1 \cos(\theta_S) \delta} \quad (2.11)$$

Thereby, the relative refractive index is defined as $n = \frac{n_2}{n_1}$. Π is the propagation factor for the light radiating through the upper halfspace. δ is the distance of the emitter from the substrate interface.

The Fresnel transmission coefficients t^p and t^s for p - and s -polarized light are given by [135, 129]:

$$t^p = \frac{2n_1 \cos \theta_S}{n_1 \cos \theta + n_2 \cos \theta_S} \quad (2.12)$$

$$t^s = \frac{2n_1 \cos \theta_S}{n_1 \cos \theta_S + n_2 \cos \theta} \quad (2.13)$$

The shape of the dipole radiation patterns, calculated with these equations are discussed in the following. These input parameters were used to simulate the emission of a point-dipole on a glass coverslide:

- $n_1 = 1$ (refractive index of air, surrounding the emitter)
- $n_2 = 1.5$ (refractive index of glass coverslide)
- $\text{NA} = 1.4$ (NA of microscope objective)

In general a dipolar radiation pattern can be divided into two areas separated by the critical angle θ_{crit} . This border is marked by a dashed circle with the radius $\frac{|k'|}{k_0} = \text{NA} = 1$. The low NA area ($\theta < \theta_{crit}$) corresponds to the previously defined allowed zone, the high NA area ($\theta > \theta_{crit}$) is in correlation with the forbidden zone. Thereby, the latter contains the majority of the overall intensity. Because of that, experimental recording of dipole radiation patterns require high NA microscope objectives for a reasonable detection yield γ . The calculation of γ is discussed in section 3.4.

Fig. 2.7a, b and c depict the patterns resulting from the radiation of point-dipoles, that are oriented along the x-axis ($\Phi=0^\circ$, $\Theta = 90^\circ$), y-axis ($\Phi=90^\circ$, $\Theta = 90^\circ$) and z-axis ($\Phi=0^\circ$, $\Theta = 0^\circ$), respectively. The radiation pattern of a randomly oriented point-dipole is illustrated in fig. 2.7d. It can be calculated as a sum of the three previously simulated dipole patterns with \vec{P} oriented along the x-, y- and z-axis due to the symmetry of the field curvature functions in eq. 2.7.

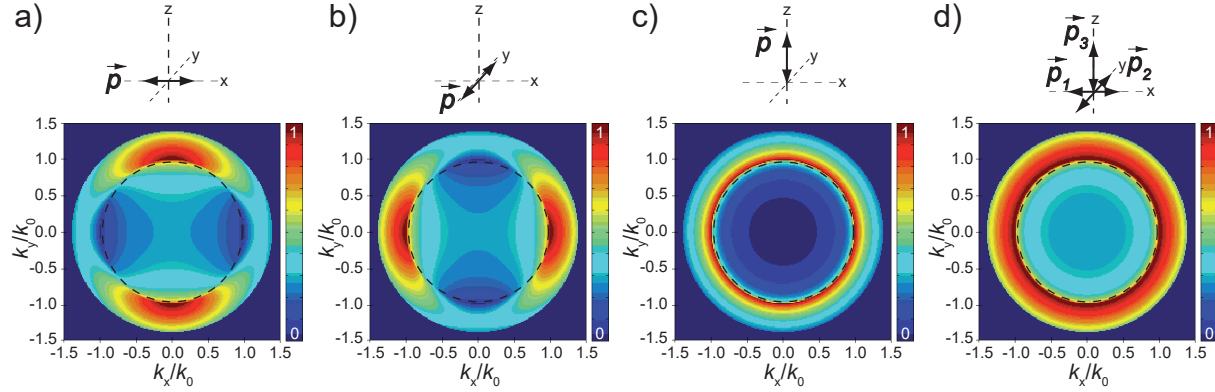


Figure 2.7: Calculated radiation patterns of dipoles on a glass/air interface for different orientations \vec{P} . The patterns are simulated according to fig. 2.6 and equations, formulated by *Lieb et al.* [22], a) x-dipole radiation pattern with $\Phi = 0^\circ$ and $\Theta = 90^\circ$, b) y-dipole radiation pattern with $\Phi = 90^\circ$ and $\Theta = 90^\circ$, c) z-dipole radiation pattern with $\Phi = 0^\circ$ and $\Theta = 0^\circ$, d) radiation pattern of a random orientated dipole with dipole components \vec{p}_1 , \vec{p}_2 and \vec{p}_3 oriented along the cartesian coordinate axes. In all images the k values corresponding to the critical angle θ_{crit} are indicated by a black dashed circle. Figure adapted from ref. [115].

The radiation patterns resulting from dipolar emitters oriented parallel to the sample plane ($\Theta = 90^\circ$) exhibit two opposing high intensity areas in the form of lobes located in the high NA area. The pattern's maxima are close to θ_{crit} . The line connecting the maxima is orthogonal to the dipole orientation \vec{P} . The two minima are also located close to θ_{crit} in the low NA area. The line connecting the minima, which are contained in two low intensity lobes, is oriented along \vec{P} . The patterns feature axial symmetry with the symmetry axis coinciding with \vec{P} .

According to the rotationally symmetric z-dipole radiation pattern, no light is emitted to the center for this case. The strongest emission is seen for $k_x^2/k_0^2 + ky^2/k_0^2 > 1$ close to θ_{crit} . The randomly oriented radiation pattern also exhibits rotational symmetry, strongly resembling the shape of the z-dipole's radiation pattern. In contrast, the contribution of the two in-plane dipoles results in an increased intensity at the center and in a broader intensity distribution of the ring in the forbidden zone.

2.3.3 Experimental Realization of Radiation Pattern Detection

The light emitted from a point in the sample plain is collimated by a lens and forms an image at the back focal plane, containing information regarding the emissive nature of the sample. This image can be treated as a Fourier transform of the image in the sample plain (real space) [98, 136]. On that account, the back focal plane image is also known as Fourier

space image. For this optical technique it is essential, that aplanatic objectives fulfill the Abbe sine condition $k = nf \sin \theta$ [129, 137]. The condition states, that light emitted from the focal point at the focal distance of the objective f_{obj} under the emission angle θ_1 leaves the objective at a distance k_1 from the optical axis parallel to it (see fig. 2.8a). Light from other positions in the sample plain with the same emission angle θ_1 have the same distance k_1 at the BFP, but are not oriented parallel to the optical axis. The distance k has a maximal value k_{max} as the diameter of the objective is limited. Thus, rays with a k exceeding k_{max} are filtered out, leading to image distortions. With this information the numerical aperture can be calculated according to:

$$NA = n_1 \sin(\theta_{max}) = \frac{k_{max}}{f} \quad (2.14)$$

Thus, the following equation can be formulated:

$$\sin \theta = \frac{kNA}{k_{max}n_1} \quad (2.15)$$

Hence, the NA is the limit of the angular range, that can be investigated.

Instead of a thin lens the first optical element in detection is an infinity corrected objective (Obj in fig. 2.4). Because of that, the back focal plane is inside the objective barrel and thus not directly accessible. The experimental detection of the Fourier space image is realized via a $4f$ -configuration using two lenses [138] (see fig. 2.8a). The integrated tube lens (TL) inside the microscope is already placed in focal distance to the first Fourier space image. In the TL's backfocal plane, an intermediate real space image is formed. A Bertrand lens (BL) [139], placed with a distance of its own focal length from the image plane, Fourier forms the second Fourier space image at its back focal plane. By installing the detector at the BL's back focal plane, the $4f$ configuration is completed.

For the experimental measurement of radiation patterns, the alignment of the optical setup is crucial. Especially the distances between optical elements along the optical axis need to be optimized. This is the factor most frequently leading to incorrect imaging [126]. The beam path of planar waves collected by the microscope objective is complementary to the beam path of light emitted from the sample plain (see also fig. 2.8b). This fact can be used for the alignment of the imaging system. The planar waves are focused at the Fourier plane of the objective. For a correctly adjusted imaging system the spot would be reimaged by the $4f$ configuration at the chip of the CCD camera. The size of the spot is limited by diffraction. Thus, a system with the appropriate element distances shows a minimal spot size of the alignment beam. This beam can be provided by a laser pointer installed above the sample. As stated above, the spot size of the alignment laser beam does only depend on the relative positions of Obj, TL, BL and the CCD camera. The angle only influences the relative position of the pattern detected on the chip of the CCD camera. Proper shielding of the detection beam path is crucial for the experimental realization. The blocked stray

results in a reduced resolution and a broadened pattern. Calculated radiation patterns of a point-dipole with $\Phi = 90^\circ$ before and after broadening are illustrated in fig. 2.9a and b. For comparison, fig. 2.9c shows a cross-section through the maxima of the respective patterns. The Airy disc diameter is $1.221\lambda/\text{NA} = 36.6 \mu\text{m}$ for the G bands emission and $39.7 \mu\text{m}$ for the 2D band emission. As a compromise, a diameter of $300 \mu\text{m}$ was selected, being larger by almost one order of magnitude.

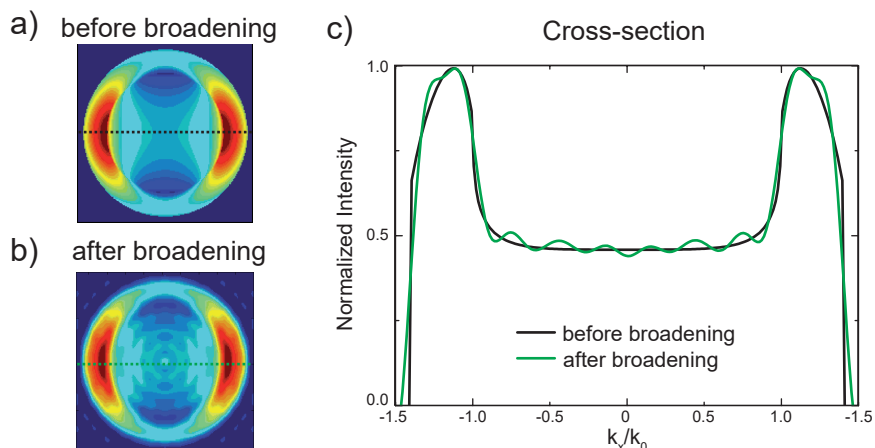


Figure 2.9: Effect of installing a pinhole in the focus of the TL on dipole radiation patterns. Placing the pinhole in the detection beampath suppresses the background signal, resulting from the microscope objective, the immersion oil and the glass substrate. Comparison between calculated dipole radiation patterns a) before and b) after mathematical broadening, c) Cross-sections of both calculated patterns through their corresponding pattern maxima.

2.3.4 Required Properties of the Microscope Objective

For experimental back focal plane imaging, the properties of the microscope objective needs to be examined carefully. *Kurvits et al.* recently analyzed several commercial microscope objectives with respect to their applicability for back focal plane imaging [126]. Their results regarding the objective (1.4 NA, 60x magnification) by the company *Nikon*, which was used during the course of this work, are presented in the following. The objective takes apochromatic and flat field corrections into account (plan apo objective). A schematic featuring the elements (23 surfaces, 8 glass types) used for this objective is shown in fig. 2.10a [140]. Each color in the scheme represents another emission angle θ . The back focal "plane" (dashed line) of the objective has a highly curved shape due to the complex refraction at the densely packed optical elements.

As already stated before, a large NA is important to detect the majority of the dipolar emission, which is localized at angles exceeding θ_{crit} . However, a large NA of an objective

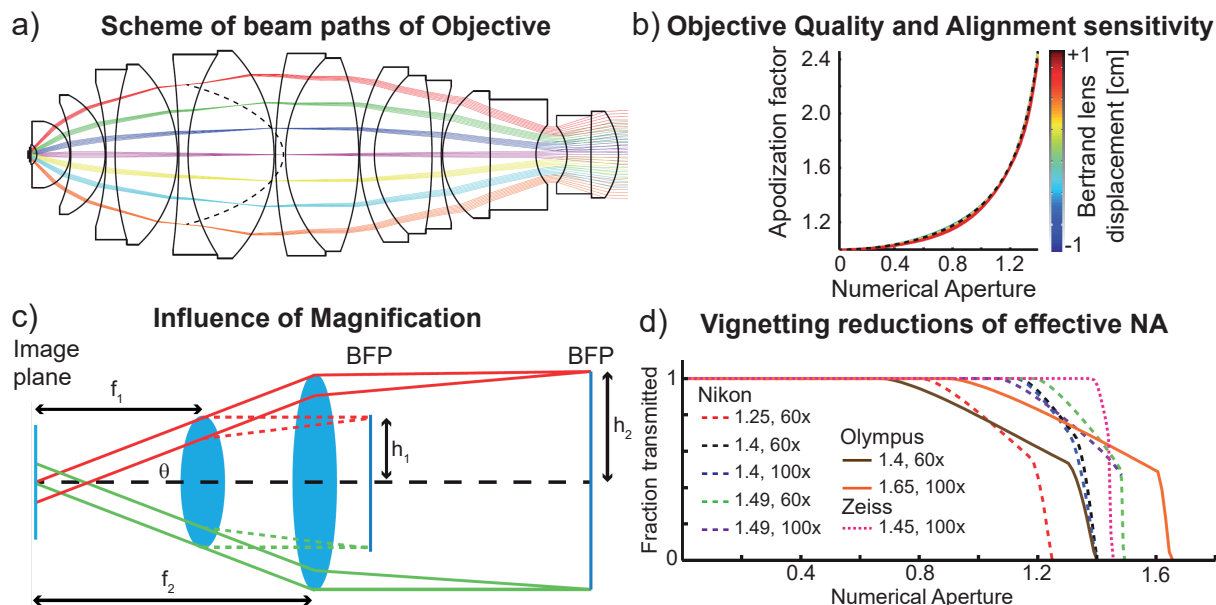


Figure 2.10: a) Scheme of the Nikon plan-apochromat objective's (1.4 NA, 60x magnification) composition. The beampath of rays emitted at different angles are illustrated by various colored lines. The objective's back focal "plane" is shown as a curved, dashed line, b) Objective quality and alignment sensitivity of the used objective. The scheme shows the graph of the Apodization factor depending on NA for different displacements of the Bertrand lens (color coded). The calculated ideal apodization factor is plotted as a black dashed line. The data was measured for a configuration with the BL placed between TL and the image plane, c) Influence of the objective's magnification on the radiation pattern size. A larger magnification has the consequence of a reduced focal length $f_1 < f_2$ and semi diameter of the radiation pattern $h_1 < h_2$, d) Vignetting reductions of effective NA. Fraction of light transmitted for full field of view for various commercially available objectives. Figures adapted from refs. [140, 126]

usually is connected to an increased image distortion. With the NA value rising towards the refractive index of the immersion medium ($n_2 = 1.5$ for immersion oil), aberrations and tolerancing errors are expected to increase. This effect can be probed by the apodization factor $\frac{1}{\cos \theta}$ as a measure for the quality of the objective (see fig. 2.10b). As image distortions are coupled to displacement and are thus difficult to correct, the apodization factor was measured in correlation with Bertrand lens defocusing between -1 to 1 cm (color coded). The data for the used objective shows good agreement with the ideal apodization factor, calculated according to ref. [141] (dashed black line). Hence, the objective has a good quality and is very insensitive to displacement of the Bertrand lens, making the objective suitable for experimental Fourier space imaging.

Besides NA and aberration corrections, it is important to consider the objective's magnification, because of its influence on the image quality and resolution. Converse to real space imaging, the detected back focal plane image is larger with a lower magnification objective with the same NA. Fig. 2.10c illustrates the influence of magnification on the BFP pattern's size for a given NA with emission angle θ . To maintain the same NA, a larger magnification $M_1 > M_2$ needs to have a reduced focal length $f_1 < f_2$. As a direct consequence the size of the BFP pattern decreases. In the scheme this is represented by the pattern's semi diameter $h_1 < h_2$. The mathematical relations, including the focal length of the tube lens f_{TL} and the refractive index of the substrate and immersion oil n_2 , are given by:

$$h = \frac{f_{TL}}{M} \left(\left(\frac{n_2}{NA} \right)^2 - 1 \right)^{-1/2} \quad (2.16)$$

The effect of the magnification on the angular resolution is further investigated by analyzing the modulation transfer function, which is defined by the observed contrast ratio at the image plane for a sine wave object of a given spatial frequency. The functions for two comparable systems are very similar. Hence, a lower magnification objective yields larger radiation patterns without loss of image quality [140, 126].

Microscope objectives generally are not equally transmissive for all collected angles. The edges of the field of view exhibit a reduced throughput. Thus, recorded radiation patterns exhibit a reduced intensity at larger angles compared to corresponding simulated patterns. This effect of vignetting is highly dependent on the collection area, which is often connected to the excitation spot size. There is almost no vignetting observable for collection from a confocal region of up to 10 μm . However, the effect is clearly observed for spot sizes beyond 50 μm . Fig. 2.10d shows the fraction of transmitted light for the whole field of view. The effect of vignetting was observed for large NA when comparing recorded and simulated Raman 2D radiation patterns of graphene (see also 3.3).

Considering all three effects, the objective installed at the microscope setup is well suited for back focal plane imaging.

Chapter 3

Raman Radiation Patterns of Graphene

*This chapter is based on the article „Raman radiation patterns of graphene“ that was published in **ACS Nano** 2016, 10, 1756.*

Its remarkable optoelectronic properties along with its atomical thickness makes graphene a versatile building block, that can be applied in various photonic and optoelectronic devices[39]. Raman spectroscopy is a non-destructive investigation tool commonly used to study the structure and electronic properties of the sample material. It is one of the most used characterization methods in carbon science and technology [142]. The measurement of graphene’s Raman spectrum [57] was a big step towards understanding the physics of graphene. The most prominent Raman bands of pristine graphene are the G and 2D bands. The 2D band Raman mechanism is closely linked to details of graphene’s electronic band structure [57, 53, 143]. This makes the 2D band sensitive to the layer number. Single layer graphene can be distinguished by a 2D/G intensity ratio of $\sim 4:1$ [57]. An additional hint towards a monolayer is a lorentzian lineshape. The bilayer displays a 2D signal split into four different components with shifted frequency. The complete graphene Raman spectrum is already well understood according to literature, but the angular distribution of the Raman scattered light has not been considered so far. However, the angular distribution of the radiation contains significant information about the emissive state, such as its dipolar [22] or multipolar [121] character, its polarization state [122, 24], its coupling to the environment [22, 24], and its spatial coherence length [123] (see also section 2.3.3). For antenna- or tip-enhanced near-field optical microscopy [23, 124, 125] the radiation pattern can be used to observe the antenna effect and its directivity [23, 144, 54]. An additional technical information, that can be extracted from the angular distribution of emission, is the detection yield achieved in an experiment. This parameter indicates the fraction collected by the objective and directed towards detection. It is given by the ratio of detected intensity to total emitted intensity I_{det}/I_{tot} .

This chapter starts with the state of the art about polarized radiation patterns (section 3.1). Based on previous knowledge about non-polarized radiation patterns, presented in section 2.3.3) the theoretical determination of polarized radiation patterns is elaborated. Subsequently, the shape of different polarization components relative to their non-polarized counterpart are discussed. The next section (section 3.2) aims at studying the angular distribution of Raman scattering from graphene and developing a quantitative model for the pattern formation. Comparison between experimental and calculated data indicates that the Raman emission can be represented as a sum of two orthogonal incoherent point-dipoles. For the G band emission the dipoles are weighted equally. In contrast, for the 2D band emission the dipoles have a weighting ratio of 3:1, which is expected from polarized Raman scattering [31, 92]. Alternatively, the 2D band emission can also be represented by the sum of three incoherent point-dipoles in a plane, each rotated by 120° respectively, which reflects the threefold symmetry of the double resonance around the \mathbf{K} and \mathbf{K}' points in the electronic band structure of graphene. The polarized 2D band patterns reveal a polarization contrast decreasing with larger collection angles due to depolarization caused by the air-dielectric interface. The dependence on the NA of the microscope objective also influences the 2D/G ratio for the case of polarized detection, that is crucial for determination of single layer graphene. The results of this work are important for quantitative analysis of Raman intensities in confocal microscopy.

3.1 State of the Art - Polarized Radiation Patterns and Depolarization

Radiation patterns for nonpolarized dipole emission are calculated according to equations reported in the work of *Lieb et al.* [22] (discussed in detail in section 2.3.3). To simulate the pattern of a polarization component of a point-dipole radiation pattern, the calculation of the E-field components E_p and E_s (eq. 3.2) need to be distinguished. For that the dipole orientation and the polarization direction of the analyzer are adjusted, matching the coordinate axis of the cartesian coordinate system. Fig. 3.1a, a modified image from chapter 2.3.3, illustrates the orientation of E_p and E_s in the BFP imaging geometry along with the plane of incidence for an emitted ray. The relationship between E_p , E_s and the field components along the coordinate axes E_x and E_y are developed via trigonometry (see fig. 3.1b):

$$E_x = E_p \cdot \cos \phi - E_s \cdot \sin \phi \quad (3.1)$$

$$E_y = E_s \cdot \cos \phi + E_p \cdot \sin \phi \quad (3.2)$$

The parallel polarized radiation pattern of a dipole is calculated by setting the E-field component perpendicular to the dipole orientation to zero. Setting the other E-field component to zero, results in the perpendicular polarized radiation pattern. Fig. 3.2a shows the nonpolarized as well as the parallel (y-polarized) and perpendicular polarized (x-polarized)

patterns for the case of a dipole oriented along the y-axis ($\Phi = 90^\circ$). The full script for the calculation of polarized radiation patterns is attached in the supplementary information A.

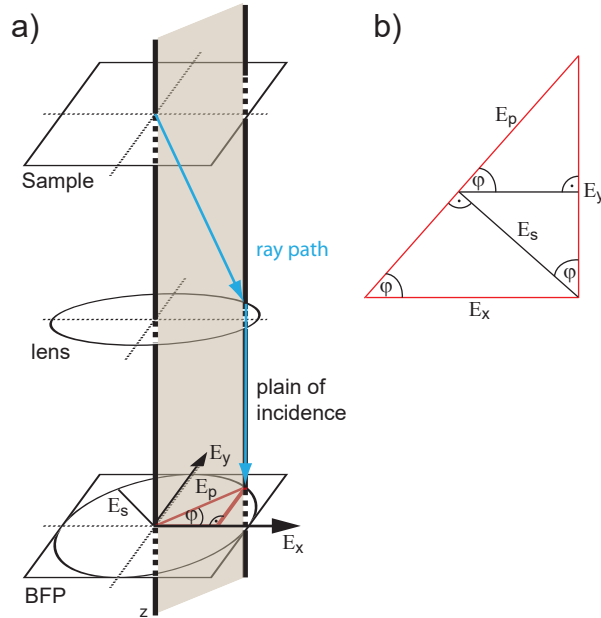


Figure 3.1: a) Back focal plane geometry with plain of incidence. Path of the emitted ray is shown in blue. Adapted from ref. [22], b) Scheme illustrating the geometrical relationships for the adjustment of the electrical field components.

The parallel polarized emission pattern strongly resembles the non-polarized pattern's shape. The high intensity lobes at angles larger than the critical angle are less extended though. The perpendicular polarized pattern shows no intensity at $NA < 1$. Intensity, that was blocked by the analyzer in the previous case, now appears in the form of four lobes in the high NA area. To verify the correct calculation, the polarized radiation pattern of a single SWCNT is considered. The photoluminescence of semiconducting SWCNTs can be viewed as the radiation of a point-dipole. These patterns were already recorded in a coworker's investigation [145]. Experimental and calculated nonpolarized and polarized radiation patterns are compared in fig. 3.2a and b. The dipole orientation of experiment and theory ($\Phi = 90^\circ$) do not exactly match, but nonetheless a qualitative agreement between experimental and calculated patterns could be determined.

The signal appearing in the perpendicular polarized pattern is unexpected, as only the E_x component should transmit the analyzer, which is set to zero for this configuration. The intensity shows a considerable fraction of 12.2% of the non-polarized pattern's intensity, localized at the high NA area. The intensity's origin is polarization mixing of the emission emerging at the air-glass interface.

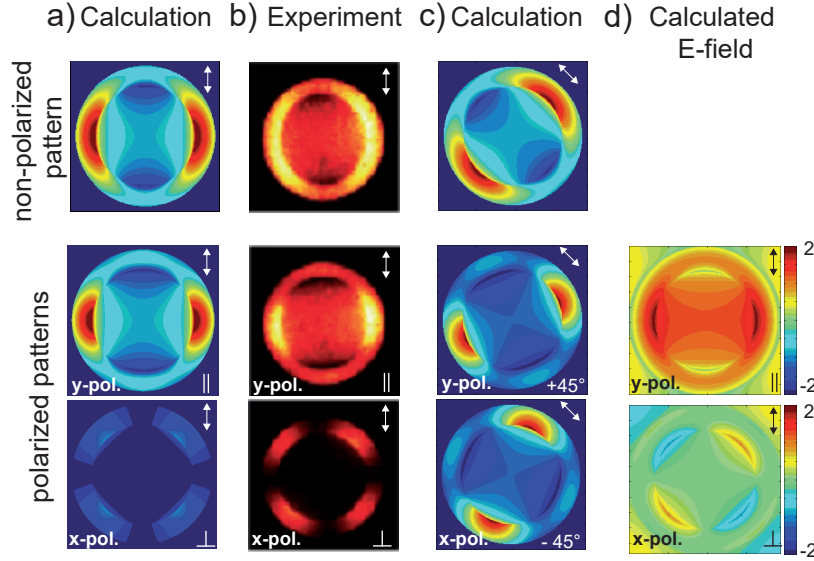


Figure 3.2: Non-polarized and polarized radiation patterns of point-dipoles. The white arrows indicate the orientation of the dipole, a) Calculated non-polarized, parallel polarized (y-polarized) and perpendicular polarized (x-polarized) radiation patterns of a point-dipole oriented along the y-axis ($\Phi = 90^\circ$). The radiation patterns are calculated with the equations reported by ref. [22], b) Experimental non-polarized, parallel polarized (y-polarized) and perpendicular polarized (x-polarized) photoluminescence pattern of a carbon nanotube oriented along $\Phi \approx 90^\circ$. Figures adapted from ref. [145], c) Calculated non-polarized, 45° polarized (y-polarized) and -45° polarized (x-polarized) radiation pattern of a point-dipole with $\Phi = 315^\circ$, d) Calculated parallel and perpendicular polarized electric field patterns for a point-dipole oriented along the y-axis ($\Phi = 90^\circ$).

The fact, that the intensity of the perpendicular polarized radiation pattern (see fig. 3.2a) is located at $NA > 1$ infers, that the extrinsic effect of polarization mixing influences signal detected at larger angles, while it is negligible for the signal at lower collection angles. Polarization mixing, also labeled depolarization, will be discussed in detail in section 3.3.

It is also possible to simulate polarized radiation patterns with a dipole to analyzer constellation other than parallel or perpendicular. This is shown for a point-dipole with an orientation of $\Phi = 315^\circ$ (illustrated in fig. 3.2c). The y-polarized pattern ($E_x=0$, "45° polarized" with respect to the point-dipole to analyzer orientation) resembles a rotated parallel polarized radiation pattern. However, the maxima do not coincide with the maxima of the non-polarized pattern, but are slightly tilted toward the x-axis. For the x-polarized pattern ($E_y=0$, "−45°" polarized) the maxima of the pattern are slightly tilted towards the y-axis. Two components contribute to the formation of the polarized radiation patterns: dipolar emission (parallel polarized radiation pattern) and depolarization (perpendicular polarized radiation pattern). To understand the tilt of the polarized radiation patterns, the phase

information of the polarized electric field patterns for the dipole emission (parallel polarized) and the depolarization (perpendicular polarized) needs to be considered. Fig. 3.2d depicts the real part of the polarized E patterns calculated for a y-dipole ($\Phi=90^\circ$). For a point-dipole with $\Phi=315^\circ$, the parallel polarized radiation pattern should be rotated by 315° . The perpendicular polarized radiation pattern is unaffected by a variation of the point-dipole orientation. The electric field exhibits a phase difference (red and blue), with opposing lobes sharing a phase. Summing up both polarized component patterns leads to constructive and destructive interference, which is the origin of the tilted patterns. More details about polarized electric field patterns are shown in the supplementary chapter A.

The intensity of the non-polarized pattern is distributed equally for the x- and y-polarized emission. This reflects, that the dipole orientation 315° is composed of equally weighted x- and y-components.

3.2 Polarization-dependent Raman Radiation Patterns of Graphene

With knowledge gained by the simulation of polarized radiation patterns, the radiation of Raman scattering of graphene is studied. Previous spectroscopic Raman investigations on graphene [31, 92] reported the polarization dependence and independence of the Raman 2D and G band respectively (details discussed in section 1.1.3). To gain more insight about the nature of the Raman radiation of graphene its angular distribution is studied.

As sample material, exfoliated graphene, fabricated as described in chapter 2, was chosen for the investigation due to its high quality and a low defect concentration. A single-layer graphene (SLG) flake was localized by confocal microscopy. In the Raman spectrum the 2D/G intensity of the flake marked in fig. 3.3a shows a ratio of roughly 3:1 identifying it as a SLG (see also fig. 3.3b) [57]. At first, the Raman G band's radiation pattern is discussed. The nonpolarized emission was recorded for two orthogonal excitation polarizations. Due to the G band's polarization independence the same pattern is expected (see chapter 1.1.3) [31]. By comparing these two patterns potential imaging artifacts can be excluded. The experimental patterns indeed showed the same result: a ring of uniform intensity with the inner border corresponding to $NA = 1$ (see fig. 3.4i) and ii)). For polarized detection the image shows two lobes on an axis orthogonal to the polarization direction of the analyzer (see fig. 3.4iii)). Rotating the analyzer by 90° also results in a rotated pattern retaining the integrated intensity (see fig. 3.4iv)). These experimental observation suggest a polarization independence consistent with previous reports [31] (see also chapter1).

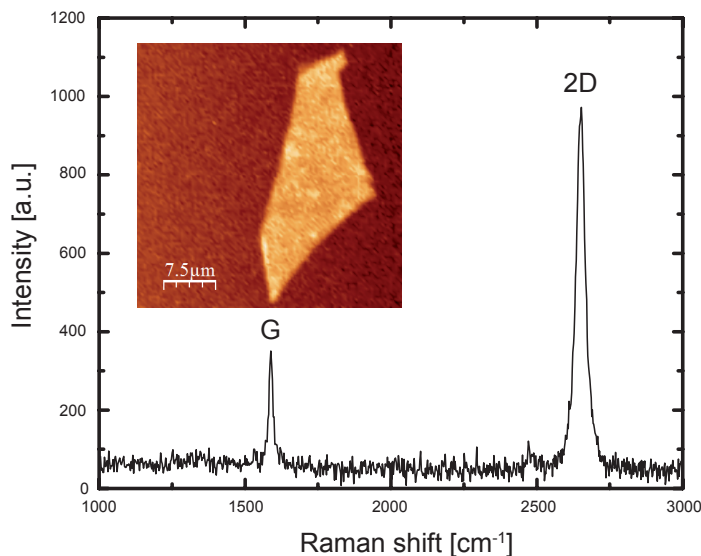


Figure 3.3: Raman spectrum of the investigated graphene flake. The inset shows a Raman 2D confocal micrograph of the studied flake.

The intensity distribution of the polarized experimental pattern (see fig. 3.4) resembles the theoretical radiation pattern of a point-dipole. This points towards the G band signal being a superposition of two orthogonal incoherent dipoles. Summing up two calculated orthogonal dipole patterns results in a radially symmetric pattern, comparable to the recorded non-polarized pattern. Quantitative agreement between calculations and experiment is attained after mathematical broadening of the calculated patterns. Comparing the corresponding cross-sections shows good agreement between experiment and theory (see fig. 3.4b). Deviations of experimental patterns from theory at low NA regions originate from difficult background correction due to a low amount of photons recorded for this area.

Fig. 3.5 a,i and ii plot the nonpolarized BFP images of the Raman 2D band recorded for two orthogonal directions of the excitation polarization. In contrast to the G band pattern, the shape of the radiation pattern depends on the excitation polarization. The axis of the recorded pattern's maxima is orthogonal to the excitation polarization similar to the radiation pattern of a point dipole. The pattern shape observed for the polarized radiation patterns (see fig 3.5a,iii and iv) also shows this feature, but unlike the polarized G band patterns, the parallel and cross-polarized patterns do not share the same integrated intensity. So the non-polarized 2D band radiation pattern can also be considered as a superposition of two orthogonal point-dipoles. However, as indicated by the different intensity of the orthogonal polarized patterns, the dipoles are weighted differently. In literature, the ratio between parallel and cross-polarized intensity $r_{2D} = I(2D)_{\parallel}/I(2D)_{\perp}$ is reported to be ~ 3 [31, 146]. So the theoretical image of the non-polarized radiation pattern can be calculated as a sum of two orthogonal incoherent dipoles with a weighting ratio of 1:3 (see fig. 3.5a,v and vi). The series of parameter-free calculations for polarized and non-polarized

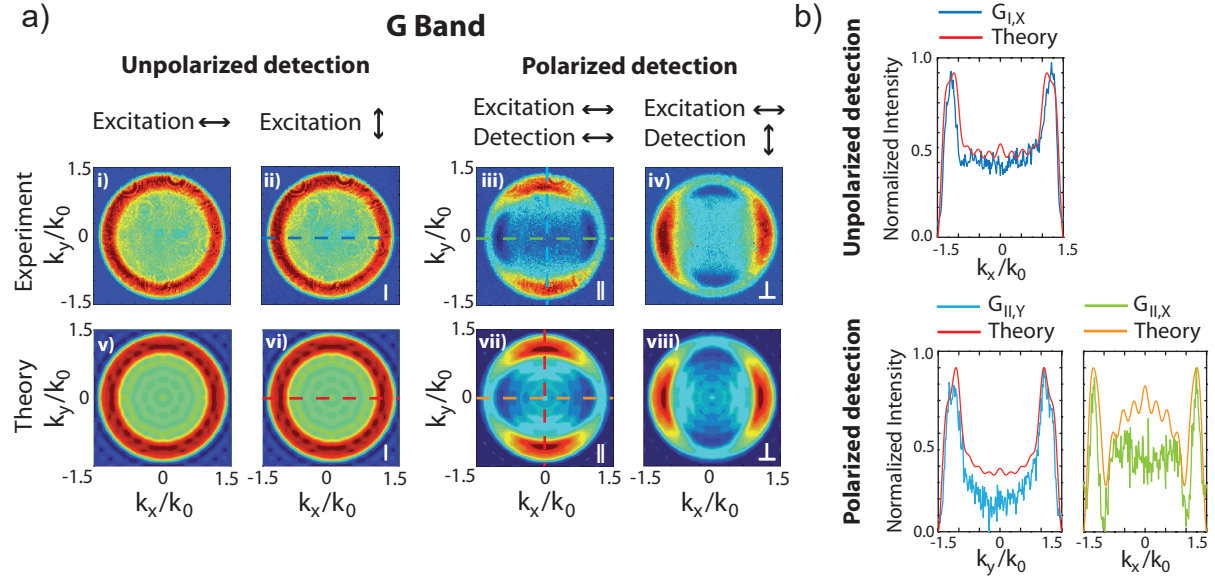


Figure 3.4: a) Experimental and calculated G peak radiation patterns with and without analyzer. The same scaling is used in each row for the experimental and theoretical data, b) Cross-sections taken through the center of the experimental and calculated BFP patterns in a). The arrows indicate the direction of polarization.

images are fitting their experimental counterparts well. The agreement between experiment and theory can also be seen in the corresponding cross-sections (see fig. 3.5b).

A different approach for calculating the 2D band radiation pattern is the superposition of three incoherent point-dipoles each rotated in-plane by 120° (see also fig. 3.6a). This model fits the symmetry properties of the double resonant Raman process around \mathbf{K} and \mathbf{K}' , which is later discussed in more detail (section 3.3). As the sample is excited with a linearly polarized beam, the intensity distributions of the three dipoles scale with the angle δ between the incident E-field and the dipole axis p : $|p \cdot E|^2 \sim \cos^2(\delta)$. Without loss of generality, one dipole is considered parallel to the excitation polarization while the other two are rotated by 120° and 240° . Thus, the two rotated dipoles are less efficiently excited: $\cos^2(120^\circ) = \cos^2(240^\circ) = 1/4$. So the radiation pattern is calculated with a dipole weighting of 1:1/4:1/4 (see also fig. 3.6b). The resulting image is in good agreement with the experiment and the image calculated with the 2-dipole model.

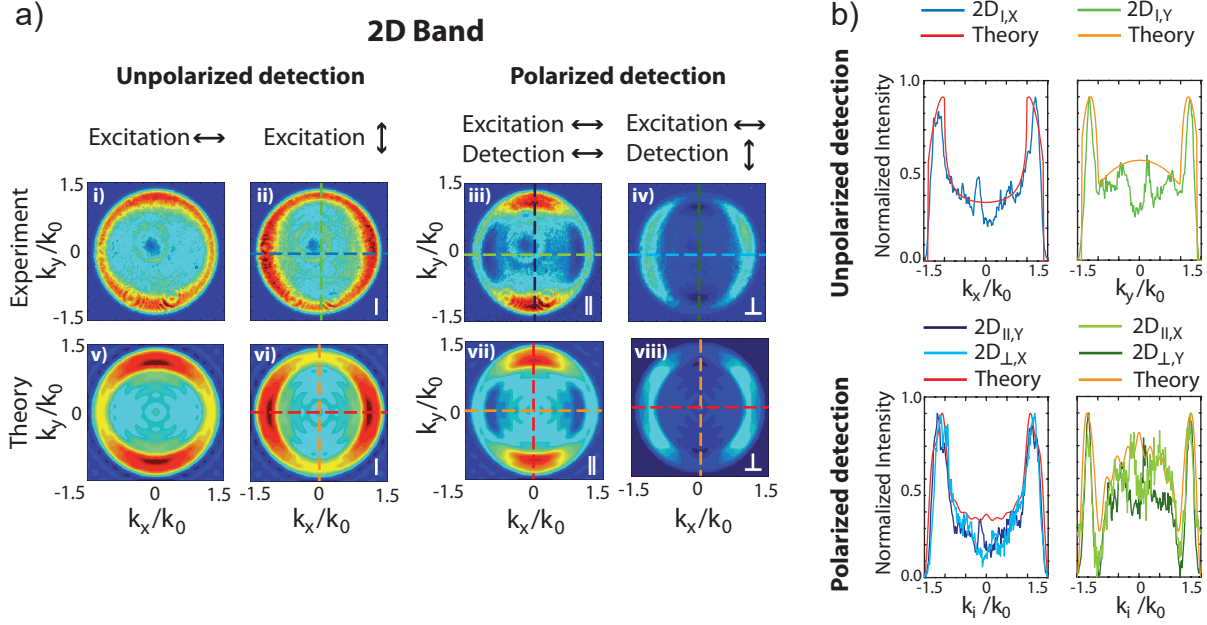


Figure 3.5: a) Experimental and calculated 2D radiation patterns with and without analyzer. The same scaling is used in each row for the experimental and theoretical data, b) Cross-sections taken through the center of the experimental and calculated BFP patterns in a).

3.3 Quantitative Raman Intensity Investigation

The ratio r_{2D} between the parallel and cross-polarized intensity of the 2D band can be calculated by integrating the intensity of the corresponding radiation patterns. The ratio extracted from experimental ($r_{2D,exp} = 2.22$) and calculated ($r_{2D,calc} = 2.02$) patterns deviate from the ratio reported in literature [31, 146] ($r_{2D,Lit} \approx 3$). The reason for that is understood after a quantitative investigation of the Raman intensity. In theory, the Raman intensity of the G band can be calculated according to the following equation [53, 31, 147, 148]:

$$I(G) \propto \sum_{i=1}^2 |\hat{e}_S \cdot R_i \cdot \hat{e}_L|^2 \quad (3.3)$$

where R_1 and R_2 are the double degenerate E_{2g} Raman polarizability tensors:

$$R_1(G) = \begin{pmatrix} 1 & 0 \\ 0 & -1 \end{pmatrix}; R_2(G) = \begin{pmatrix} 0 & 1 \\ 1 & 0 \end{pmatrix} \quad (3.4)$$

and \hat{e}_L and \hat{e}_S are the unit vectors of polarization for incident and scattered light at the focus of the microscope objective.

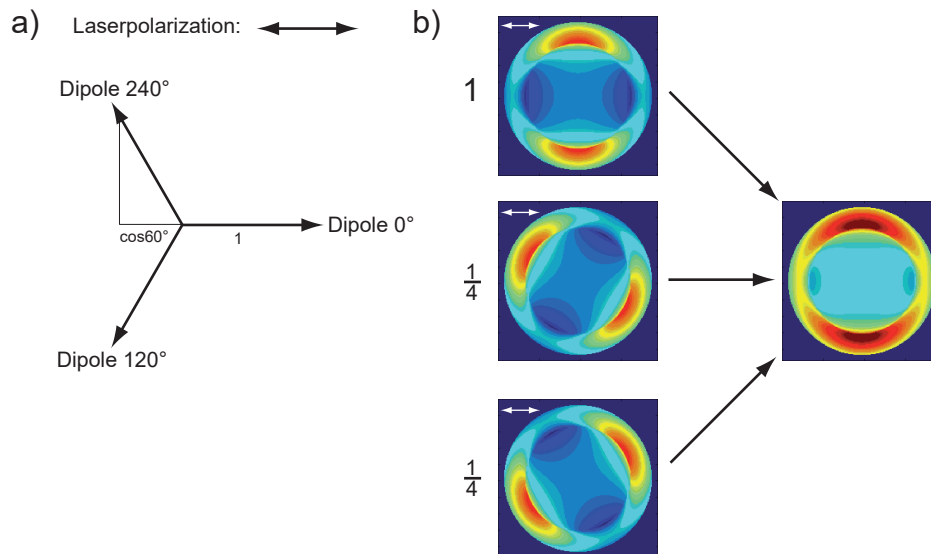


Figure 3.6: a) Scheme illustrating the excitation in the 3-dipole model. While the dipole 0° parallel to the excitation polarization shows a relative excitation strength of 100% the other two dipoles exhibit only a partial relative excitation, b) The patterns of the three dipoles summed up accordingly result in the same pattern as for the 2-dipole model.

Based on information from the previous two sections, eq. 3.3 is extended to both Raman G and 2D band. As discovered before, the Raman G emission can be viewed as a sum of two orthogonal incoherent point-dipoles, which also accounts for eq. 3.3. The dot product $R_i \cdot \hat{e}_S$ would thus be seen as the oscillation of the two orthogonal dipoles. The sum over modulus square takes into account the incoherent superposition.

As already mentioned above (see section 3.1), samples with an air-dielectric interface display the effect of depolarization, that shows an influence for $NA > 1$. This dependence of depolarization p_S on NA is quantified by the ratio between detected intensity for perpendicular $I(S)_\perp$ and parallel $I(S)_\parallel$ polarization. By integrating the corresponding radiation patterns over an increasing angular range these intensities are calculated. For the cross-polarized emission patterns the effect of p_S becomes considerable for $NA > 1$ as expected (see fig. 3.7a).

Besides depolarization of the emission emerging from the air-glass interface, it can also be caused during excitation in the focus of a high NA objective ($NA > 1$) due to tight focusing and the dielectric-air interface. The depolarization of excitation is labelled as p_L . To calculate the NA dependence of p_L , the equations describing a strongly focused linearly polarized Gaussian laser beam formulated by ref. [134] are applied. The ratio between intensity components of perpendicular $I(L)_\perp$ and parallel $I(L)_\parallel$ polarization gives $p_L = I(L)_\perp / I(L)_\parallel$. When looking at its influence in relation to NA, p_L also follows the trend of becoming more substantial at larger angles, though not as significant as p_S . Both depo-

larization effects have a stronger influence for $NA > 1$. The increasing influence of both depolarization effects are illustrated in fig. 3.7a.

For the case of the G band intensity, the effect of depolarization cancels out because of its symmetry properties as $|R_1 \cdot \hat{e}_x| = |R_2 \cdot \hat{e}_y|$. For the 2D band, however, depolarization needs to be considered. The general formula containing the influence of depolarization is shown in the following:

$$I(G; 2D) \propto \sum_{i,j,k} |\hat{e}_S \cdot P_S^j \cdot R_i \cdot P_L^k \cdot \hat{e}_L|^2 \quad (3.5)$$

with $i = 1, 2$ and $i = 1-3$ for the case of G and 2D, respectively, and $j, k = \parallel, \perp$. Depolarization matrices are developed empirically considering both p_L and p_S (see fig. 3.7a):

$$P_{S,L}^\perp = \begin{pmatrix} 0 & \sqrt{p_{S,L}} \\ -\sqrt{p_{S,L}} & 0 \end{pmatrix}; \quad P_{S,L}^\parallel = \begin{pmatrix} \sqrt{1-p_{S,L}} & 0 \\ 0 & \sqrt{1-p_{S,L}} \end{pmatrix} \quad (3.6)$$

with $p_S = I(S)_\parallel / I(S)_\perp$ and $p_L = I(L)_\parallel / I(L)_\perp$. As depolarization is neglectable for $NA < 1$, eq. 3.5 simplifies to eq. 3.3 for that case. The Raman polarizability tensors of the totally symmetric 2D phonons do not result in the polarization contrast $r_{2D} \approx 3$ reported in literature[31, 148]. This can be explained by the double resonance process and the interplay between photon-electron and electron-phonon coupling. Intervalley scattering between \mathbf{K} point and \mathbf{K}' point with six possible $\mathbf{K}-\mathbf{K}'$ and $\mathbf{K}'-\mathbf{K}$ combinations need to be considered. Symmetry reasons narrow them down to three $\mathbf{K}-\mathbf{K}'$ combinations. The double resonant intervalley scattering leads to distinct electronic populations around the three different \mathbf{K}' points, each rotated by 120° , neighbouring the \mathbf{K} points[31]. This is consistent with the 3-dipole-model described before. The corresponding three Raman polarizability tensors thus reflect the symmetries of the electronic populations caused by the double resonant Raman scattering process, given by:

$$R_1(2D) = \begin{pmatrix} 1 & 0 \\ 0 & 1 \end{pmatrix}; \quad R_2(2D) = \frac{1}{4} \begin{pmatrix} -1 & -\sqrt{3} \\ \sqrt{3} & -1 \end{pmatrix}; \quad (3.7)$$

$$R_3(2D) = \frac{1}{4} \begin{pmatrix} -1 & \sqrt{3} \\ -\sqrt{3} & -1 \end{pmatrix} \quad (3.8)$$

R_2 and R_3 are calculated by rotation of R_1 by 120° and 240° . As described for the simulation of the emission pattern the excitation efficiency of the dipoles is scaled by the ratio 1:1/4:1/4. So in contrast to the G signal, the 2D intensity is polarization dependent and thus is influenced by depolarization. Since depolarization depends on NA, r_{2D} also depends on NA, given by:

$$r_{2D}(NA) = \frac{I(2D)_\parallel}{I(2D)_\perp} = \frac{3 - 2p_S - 2p_L + 4p_S p_L}{1 + 2p_S + 2p_L - 4p_S p_L} \quad (3.9)$$

Repeating these calculations for the case of the mathematically equivalent 2-dipole model results in the same term for r_{2D} validating eq. 3.9. Using this equation for theory data (blue squares) and the corresponding intensity values extracted from recorded patterns for the experiment (red triangles), r_{2D} is plotted against NA (see fig. 3.7b). Both theory and experiment display a substantial decrease of about 30% towards larger NA caused by depolarization. Deviations between experiment and theory can be explained by artifacts from experimental realization. At small collection angles, a low detected photon rate causes bad background correction for laser scattered light, while at large angles the transmission of the microscope objective is reduced [126] (see also section 2.3.4). The large discrepancy of r_{2D} values reported in literature and in this work mentioned at the beginning of this chapter therefore can be explained by the different influence of depolarization for small (NA = 0.8 for ref. [31]) and large NA (NA = 1.4 for this work) objectives.

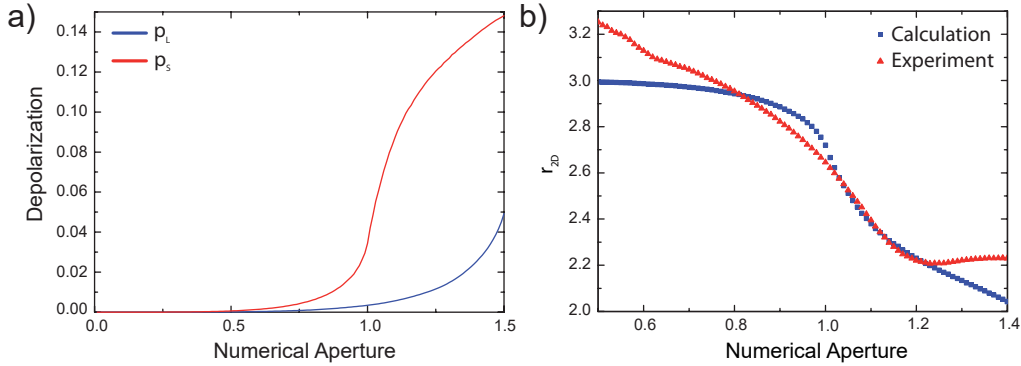


Figure 3.7: a) Depolarization of excitation p_L and emission p_S at the glass-air interface as a function of the focusing angle θ expressed by $NA = n \sin \theta$, b) experimental and calculated 2D intensity ratio for parallel and perpendicular polarized light $r_{2D} = I(2D)_{||}/I(2D)_{\perp}$. The curve is a plot of eq. 3.9.

The ratio $\rho = I(2D)/I(G)$ is frequently used in the literature for the spectroscopic determination of SLG. In the case of polarized detection $I(G)$ is independent of depolarization. In contrast, $I(2D)$ and ρ should be influenced by p_L and p_S . To prove this, a series of parallel polarized spectra with varying NA was recorded and normalized to the G peak. As illustrated in fig. 3.8, with rising NA and depolarization influence, the intensity of the 2D peak increases. ρ can be expressed by the NA-dependent r_{2D} :

$$\rho = \frac{I(2D)}{I(G)} = \frac{I(2D)_{||} + I(2D)_{\perp}}{2I(G)_{||}} = \frac{r_{2D}I(2D)_{\perp} + I(2D)_{\perp}}{2I(G)_{||}} \quad (3.10)$$

$$\rho_{||} = \frac{I(2D)_{||}}{I(G)_{||}} = \frac{r_{2D}I(2D)_{\perp}}{I(G)_{||}} \quad (3.11)$$

$$\rho_{\perp} = \frac{I(2D)_{\perp}}{I(G)_{\perp}} = \frac{r_{2D}I(2D)_{\perp}}{I(G)_{||}} \quad (3.12)$$

This definition leads to:

$$\frac{\rho_{\parallel}}{\rho} = \frac{r_{2D}I(2D)_{\perp} \cdot 2I(G)_{\parallel}}{I(G)_{\parallel} \cdot [r_{2D}I(2D)_{\perp} + I(2D)_{\perp}]} = \frac{2r_{2D}I(2D)_{\perp}}{I(2D)_{\perp}[r_{2D} + 1]} = \frac{2r_{2D}}{r_{2D} + 1} \quad (3.13)$$

$$\frac{\rho_{\perp}}{\rho} = \frac{I(2D)_{\perp} \cdot 2I(G)_{\parallel}}{I(G)_{\perp} \cdot [r_{2D}I(2D)_{\perp} + I(2D)_{\perp}]} = \frac{2}{r_{2D} + 1} \quad (3.14)$$

with ρ being the unpolarized ratio, ρ_{\parallel} (ρ_{\perp}) the polarized ratio for parallel (perpendicular) polarization. Fig. 3.8 illustrates the NA dependence of experimental and calculated ρ_{\parallel} and ρ_{\perp} normalized over ρ . The experimental data agrees with the corresponding calculated values. While the parallel polarized case ρ_{\parallel}/ρ shows a decrease with rising NA (experimentally demonstrated in fig. 3.8 a)), the opposite trend is displayed for cross-polarization ρ_{\perp}/ρ (see fig. 3.8b)).

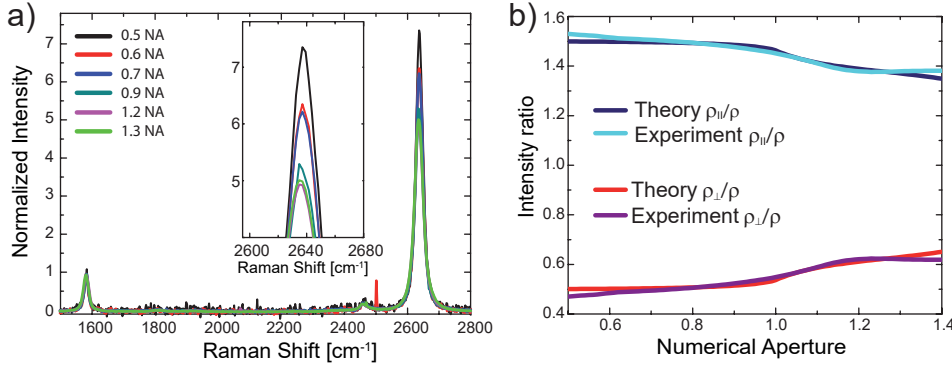


Figure 3.8: a) Parallel polarized SLG Raman Spectra as a function of NA. All spectra are normalized to $I(G)$, b) NA dependence of $I(2D)/I(G)$ with $\rho = \frac{I(2D)}{I(G)}$, $\rho_{\parallel} = \frac{I(2D)_{\parallel}}{I(G)_{\parallel}}$ and $\rho_{\perp} = \frac{I(2D)_{\perp}}{I(G)_{\perp}}$ as defined in the text.

The D peak Raman radiation pattern is expected to behave similar to the 2D band. This can be explained by it having the same directional preference for electron-phonon scattering as the intervalley resonant Raman process of the 2D band. The depolarization discussion of the $I(D)/I(G)$ ratio should therefore be equivalent. Polarized Raman scattering can be observed for linear extended defects localized in one dimension of the momentum space [54, 76, 77]. The D peak intervalley Raman process occurs for armchair edges only when the incident polarization is parallel to the edge. For perfect edges polarized Raman scattering with a contrast of 100% is expected. For the case of high NA both p_L and p_S would reduce the observed contrast. Using the values plotted in fig. 3.7a (depolarization) a polarization contrast of $(100 - 13 - 2)\% = 85\%$ would be expected for NA = 1.4 in case of perfect edges.

For fully coherent scattering, the spatial integral of the induced Raman polarization needs to be included in the modulus square of eq. 3.5 as the excitation field within the focus area is coherent. Spatially coherent Raman scattering would have an influence on the observed radiation pattern if the coherence length would be $\sim\lambda/4$. In this case, retardation effects would play a role [147, 148]. As all experimental patterns could be quantitatively described with the emission of point-dipoles, the coherence length is expected to be substantially smaller [147, 148]. It was reported that spatially coherent Raman scattering influences the near-field optical response with a coherence length of ~ 30 nm. As this value is $< \lambda/4$ our treatment of SLG Raman patterns as spatially incoherent is justified. The polarized Raman 2D intensity terms depending on p_L and p_S for the coherent case, $p_{L,coherent}$ and $p_{S,coherent}$, are shown in eqs. 3.15 and 3.16.

$$I(2D)_{\parallel,coherent} = 9(1 - p_S)(1 - p_L)6\sqrt{(1 - p_S)}\sqrt{(p_L)} + (1 - p_S)p_L + p_S(1 - p_L)46\sqrt{(p_S)}\sqrt{(p_L)} + 9p_Sp_L \quad (3.15)$$

$$I(2D)_{\perp,coherent} = 2\sqrt{(1 - p_S)}\sqrt{(1 - p_L)} + 10(1 - p_S)p_L + 12\sqrt{(1 - p_S)}\sqrt{(p_L)} + 24\sqrt{(p_S)}\sqrt{(1 - p_L)} + 9p_S(1 - p_L)14\sqrt{(p_S)}\sqrt{(p_L)} + p_Sp_L \quad (3.16)$$

Using these equations, the 2D intensity ratio $r_{2D,coherent}$ depending on NA are calculated. In contrast to the incoherent case (see fig. 3.7b) the calculated curve for the coherent case, illustrated in fig. 3.9, differs widely from the experimental curve. This confirms, that the assumption of the incoherent case for the graphene Raman radiation patterns is correct, additionally.

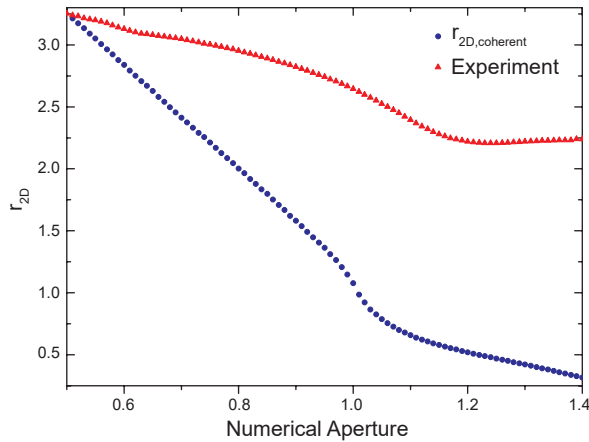


Figure 3.9: Experimental and coherent case calculation for 2D intensity ratio for parallel and perpendicular polarized light $r_{2D,coherent} = I(2D)_{\parallel,coherent}/I(2D)_{\perp,coherent}$. The curve is calculated using eqs. 3.15 and 3.16.

3.4 Fraction of Detected Light

With recorded and calculated radiation patterns the fraction of detected light γ can be derived. γ is depending on the collection angle and is given by:

$$\gamma = \frac{P_{detected}(NA)}{P_{total}} = \frac{P_{detected}(NA)}{P_{lhs} + P_{rhs}} \quad (3.17)$$

where P_{total} is the total emitted power distributed over both halfspaces and thus is calculated by $P_{total} = P_{rhs} + P_{lhs}$. As a backscattering microscope geometry is used, the upper halfspace is air and the lower halfspace is glass substrate. γ is calculated by integrating the radiation patterns from 0 to NA, followed by normalization of the patterns integrated over 4π (see fig. 3.10). The fraction of detection efficiencies for the experimental G and 2D peak have very similar NA dependencies up to NA = 1.2. The experimental curves are normalized to the calculated value at NA = 1. This value was chosen as the microscope objective's transmission for marginal rays at larger angles is lower [24, 149, 150].

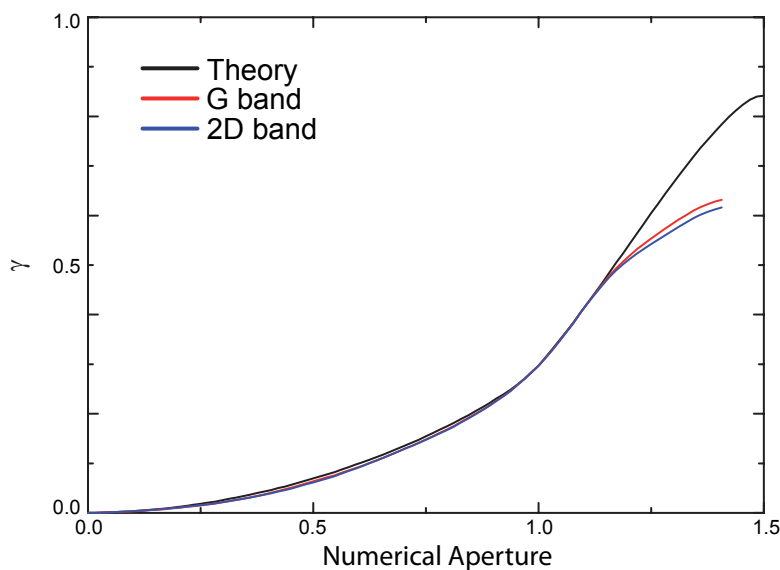


Figure 3.10: Experimental and calculated fraction of detected light as a function of NA. The experimental curves are normalized to the theoretical value at NA=1.

The Raman radiation patterns (see figs. 3.4 and 3.5) and NA dependent detection yield γ (see fig. 3.10) from graphene on glass provide a complete quantitative description of the polarized Raman signals detected in a microscope configuration. The description shown here will be useful for the discussion of signal enhancement due to plasmonic nanostructures placed in the vicinity of SLG. Plasmonic nanostructures (e.g. Au nanorods, see chapter B) can act as optical antennas and therefore influence the angular distribution of emission. To quantify the Graphene Raman signal enhanced by such an antenna, the exact knowledge of the spatial distribution of emission as well as the NA dependent fraction of detection is necessary.

3.5 Conclusion

In this chapter, the angular distribution of Raman emission from graphene was discussed. The homogeneous ring shape of the G band radiation pattern illustrates the emission's isotropic nature with respect to the excitation polarization. The emission pattern can be expressed as the sum of two orthogonal incoherent point-dipoles. The 2D band's radiation, however, is depending on polarization and can be described either as a sum of two orthogonal incoherent point-dipoles with a weighting ratio of 3:1 or as a sum of three incoherent dipoles in a plane each rotated by 120° . Examining the intensity of polarized Raman 2D radiation patterns revealed a decrease in polarization contrast with increasing numerical aperture, mainly caused by depolarization of the radiation at the air-dielectric interface. A subsequent quantitative intensity study of the Raman signal helped understanding the effect of depolarization itself and its influence on the Raman intensity in general. Considering this, a general equation for Raman intensity of graphene was developed (eq. 3.5). Insights gained in this work can be applied for optical studies on a wide range of sample materials including other thinfilm material (e.g. transition metal dichalcogenides, silicene, etc.) as well as nanotubes and nanowires. The results presented here are thus important for quantitative Raman intensity studies using high NA objectives. Scientists, using high NA setups, commonly need to consider the extrinsic effect of polarization scrambling (depolarization), that occurs in the focal region of high NA objective lenses[151].

Chapter 4

Raman Defect Study of Recycled SWCNTs

*This chapter is based on the article „Recycle it: Material-efficient dispersing of carbon nanotubes without scission“ submitted to **Scientific Reports**.*

Single-walled carbon nanotubes (SWCNTs) exhibit unique properties like mechanical stability [152], high electron mobility [153] and large electrical [154] and thermal conductivity [155]. Especially in the form of a dense network, fabricated and characterized also in this work (details in supplementary chapter), SWCNTs are a promising candidate for application in transparent electrodes[156, 157, 158], transistors [159, 160, 161], printed antennas[162, 163] and heating elements[164]. Despite this, SWCNTs are still not commonly used commercially yet. This can be explained by their energy consuming and expensive process technology: The raw material, typically synthesized by chemical vapor deposition, arc discharge or laser ablation, contains various impurities such as catalyst material, graphene and amorphous carbon. The SWCNTs in the soot of the raw material mainly occur as aggregates. To obtain single SWCNTs and simultaneously purify the sample, the raw material is sonicated in aqueous tenside or polymer solution. Both act as a surfactant, wrapping around individual SWCNTs and crushed agglomerates for stabilization in solution. A centrifugation step separates single SWCNTs in solution from SWCNT aggregates and impurities in the precipitate. Besides those three processing steps additional work stages like density-gradient ultra centrifugation [165, 166, 167] or chromatography [168, 169, 170] can be added to obtain material, that is sorted by chirality or length.

Besides the purity of the dispersion, there is another criterion for the use of SWCNTs in electronic devices. The SWCNT length L has a direct impact on optoelectronic performance [171]. We know from percolation theory that the critical number of sticks per area unit N_c required for percolation scales with the SWCNT length L as $N_c = 5.637/L^2$ [172, 173]. Therefore, doubling of L would lead to a reduction of N_c by factor four. That implies, that conductive films can be fabricated with substantially higher optical transmission. Additionally, because the intrinsic resistance of a SWCNT is several orders of magnitude lower

than the junction resistance between two SWCNTs, making the overall sheet resistance higher for networks consisting of long SWCNTs and increasing the conductance of the device. This makes liquid film coatings for dispersions with long SWCNTs highly desirable.

Ultrasonication causes scission of SWCNTs and scales with the power law $L \sim t^m$, with t being the sonication time and $m = 0.2-0.5$ [174, 175, 176]. Hence, a short sonication time is desired for dispersions containing long SWCNTs. However, a direct consequence of short sonication time is an increased fraction of SWCNTs that remains in the precipitate and thus results in a low dispersion yield [177, 178]. As the fabrication of SWCNT dispersions is energy-consuming and the raw material expensive, a high dispersion yield is of prime importance. Thus, the goal of this work is overcoming the scission of SWCNTs by long sonication and the poor material-efficiency for short sonication times.

A method to extract long SWCNTs in a material-efficient way is presented here. Extracting the solution and discarding the precipitate after the centrifugation step is the standard method, making it common to discard a large fraction of SWCNTs. The possibility to reutilize SWCNTs in the precipitate is investigated. Several recycled dispersions are fabricated by sonicating the previous sample's precipitate. Nanotube dispersions are characterized by atomic force microscopy (length statistics), absorption (material efficiency) and Raman spectroscopy (defect statistics). Comparison with a SWCNT dispersion sonicated for a substantially longer time, shows that SWCNTs, extracted by the presented method, have a similar dispersion yield while also having a larger mean length and lesser average defect concentration.

4.1 Recycling of Dispersed SWCNTs and their Characterization

The fabrication of SWCNT dispersions, their characterization using optical absorption spectroscopy and atomic force microscopy after deposition on a substrate and the statistical SWCNT length analysis were realized by **T. Ackermann** at the Fraunhofer Institute for Manufacturing Engineering and Automation, Stuttgart.

The original SWCNT dispersion (*dispersion 1*) was fabricated by sonicating CoMo-Cat CG200 raw material in aqueous sodium dodecyl benzenesulfonate (SDBS) solution for 20 min. Nanotube aggregates and impurities were separated by centrifugation and subsequent filtration, isolating single SWCNTs in the liquid phase. Experimental details are described in section 2.1.1. In order to investigate the usability of the precipitate as a building block for optoelectronic devices, it is redispersed instead of the initial raw material within a second sonication-centrifugation-filtration procedure with the same parameters as for the fabrication of *dispersion 1* (see fig. 4.1). The product is referred to as *dispersion 2*.

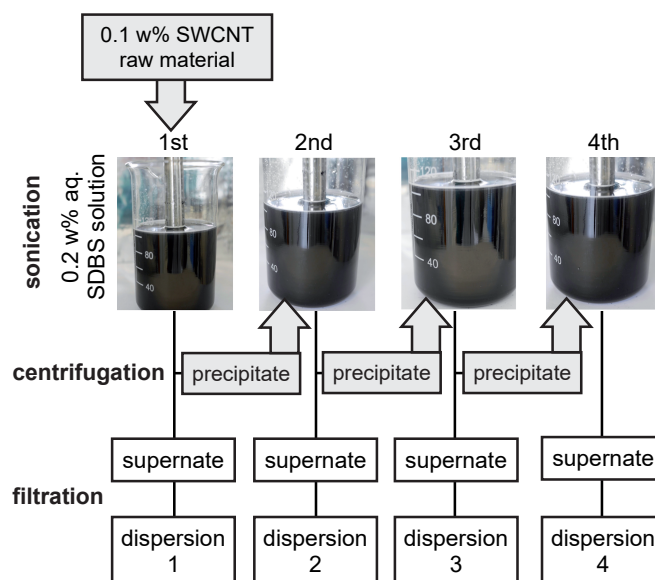


Figure 4.1: The procedure for the recycling of the precipitate from the previous sonication-centrifugation process.

The *dispersions 3* and *4* are the batches from the sonication of the precipitate from the second and third sonication-centrifugation process, respectively. That way, four purified dispersions were obtained. Moreover, a fifth dispersion with direct sonication of the initial raw material for 80 min was fabricated in order to compare the dispersions obtained via the recycling procedure with regard to material-efficiency and scission of SWCNTs (*80 min dispersion*).

The samples were then characterized via absorption spectroscopy. The linear relation between absorbance and carbon concentration, given by Lambert Beer's law, however is not valid for too high concentrations. This is due to high analyte concentrations leading to an altered refractive index, which causes a different absorbance. The same effect can be explained by a variation of the molecule charge distribution because of a larger proximity and density of adjacent molecules. Besides these, there are various other reasons for a nonlinear absorbance to concentration relation including instrumental deviations [179, 180]. In order to obtain validity of Lambert-Beer's law, the samples were diluted by 1:9 with 0.2 w% aqueous SDBS solution. The absorbance of the M_{11} transition peak at 656 nm was chosen as a reference. Fig. 4.2a illustrated the absorption spectra of the five fabricated dispersions. All spectra exhibit the same shape, displaying that the samples have the same chemical composition and are thus comparable in terms of absorbance. The *80 min dispersion* shows substantially stronger absorption than the others, implying that its dispersion yield is the largest. This confirms the proportionality between sonication time and dispersion yield mentioned above. Out of the four batches processed by the recycling method, the sample resulting from the first recycling step, *dispersion 2*, shows the

strongest absorbance. This proves, that quite a large number of SWCNTs remain in the precipitate after the first sonication step. Further use of precipitates would thus lower costs significantly, improving industrial scalability of SWCNT dispersions while the quality of the SWCNTs is retained.

The large dispersion yield of *dispersion 2* can be explained by the mechanism illustrated in fig. 4.2c. In the initial raw material the SWCNTs are aggregated due to van-der-Waals-forces (π -stacking). The outer SWCNTs (represented as white cross sections) are encapsulated by the nonpolar carbon chain of the SDBS molecules. The van-der-Waals forces attracting the SWCNT to the agglomerate are weakest for outer SWCNTs, because of the reduced number of surrounding SWCNTs. In addition, the outer SWCNTs are already partially stabilized in solution by surfactants, making these SWCNTs more likely to be separated by cavitation. Therefore the outer SWCNTs are separated as individual SWCNTs or small bundles consisting of few SWCNTs. These are light enough in order to remain in the dispersion after centrifugation. *Strano et al.* have proposed a mechanism for the adsorption of the surfactants on the outer SWCNTs [181]. Thereby cavitation induces unzipping of the SWCNTs from the end of the tubes, allowing surfactants to diffuse into the free space between the aggregate and the exfoliating outer tube (inset in fig. 4.2c).

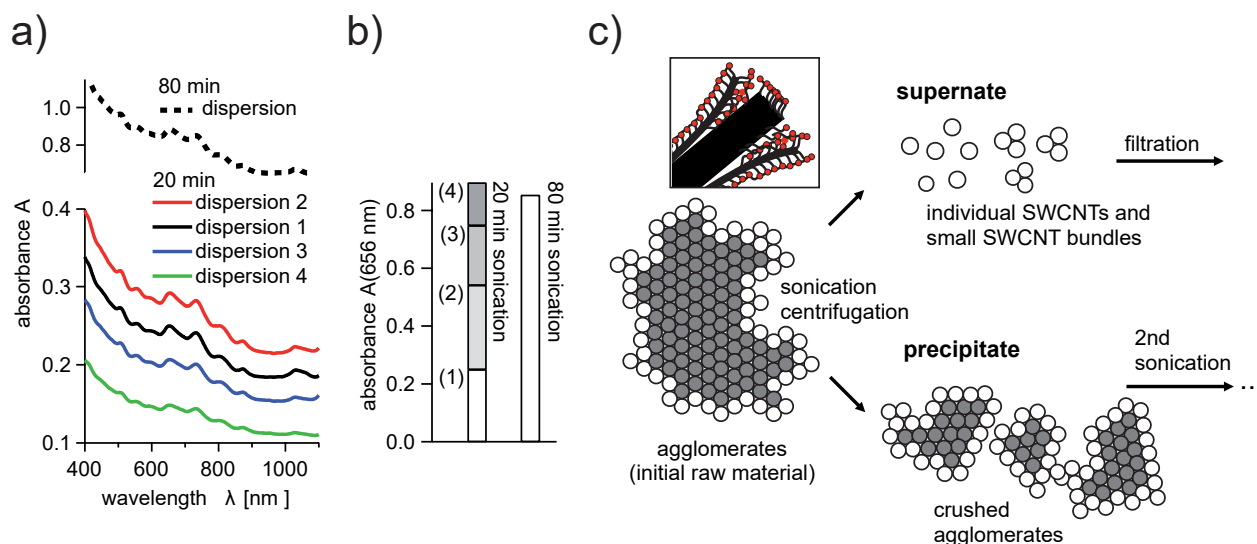


Figure 4.2: a) Absorption spectra of the different dispersions from fig. 4.1 b) The summarized absorbance of dispersions 1-4 compared to direct sonication for 80 min, c) Proposed mechanism for the unexpected optimum of the dispersion efficiency. The sketch represents the cross sections of the SWCNT bundles. White circles represent the outer SWCNTs. The inset shows the mechanism proposed by *Strano et al.* [181], where the outer SWCNTs unzip from the bundle end. The colored particles represent the surfactants.

Thus, dispersion efficiency is determined by surface to volume ratio of the aggregates. During the first sonication the aggregates shrink. The precipitate used for the first recycling step therefore should contain smaller aggregates compared to the raw material. As a direct consequence, the overall surface of the aggregates as well as the amount of outer SWCNTs is larger. Hence, more individual SWCNTs should be isolated during the second sonication, which is in agreement with the experimental observations. From the other two recycling steps less material is extracted compared to material dispersed from the raw material. This is due to the amount of dispersable SWCNTs was significantly lowered by the first two sonication steps.

The relative absorbance of the dispersions at the reference point is illustrated in fig. 4.2b. The summed up absorbance of the individual dispersions obtained during the recycling process is similar to the absorbance of the *80 min dispersion*. The dispersion yields of the standard and the recycling procedure are thus comparable.

Besides the dispersion yield the average length of SWCNTs in dispersions is a subject of interest, as a reduced length of SWCNTs in a dense network leads towards a lower overall conductivity of the network[171]. The length of the SWCNTs in the dispersions were statistically determined via atomic force microscopy (AFM). The preparation of the samples for the topographical analysis is described in section 2.1.1. For each sample hundreds of SWCNTs were analyzed ensuring statistical relevance. An overview of the length statistics from *dispersion 1*, *dispersion 4* and the *80 min dispersion* are illustrated in fig. 4.3. The histograms of *dispersion 1* and *4* show a similar distribution of SWCNT lengths within the range between $0.3\ \mu\text{m}$ and $3.0\ \mu\text{m}$. Both samples have a similar mean length of about $1.0\ \mu\text{m}$. Compared to that, the length distribution of the SWCNTs from the 80 min dispersion is less expanded and mainly below a length of $0.8\ \mu\text{m}$. The mean length is nearly a third of the previously observed average length at a value of $0.32\ \mu\text{m}$. The shorter lengths of the *80 min dispersion* originate from significant scission due to longer sonication time, as expected. The SWCNTs of *dispersion 4* were also sonicated for 80 min in total, but exhibit larger SWCNT lengths. This is due to a large portion of SWCNTs remaining inside the aggregate, protected from scission, until being exfoliated by sonication. Therefore there are no individual SWCNTs which are sonicated for 80 min although the aggregates are sonicated for 80 min in total. Nanotubes are efficiently shortened only when they are dispersed individually or inside thin bundles. Hence, it is necessary to consider an effective sonication time for individual SWCNTs, which has a value of 20 min for *dispersion 1* to *dispersion 4*. Because of that, the SWCNT length is constant during the recycling process shown in fig. 4.1. In conclusion, there are two simultaneous processes during sonication, that need to be considered. The crushing process severs van-der-Waals forces between SWCNTs in aggregates separating them into smaller agglomerates, thin bundles and individual SWCNTs. The SWCNTs themselves are not affected by this process. In contrast to that, in the cleaving process, the SWCNTs are shortened due to scission. The interplay between both processes is the reason for the different length statistics illustrated in fig. 4.3.

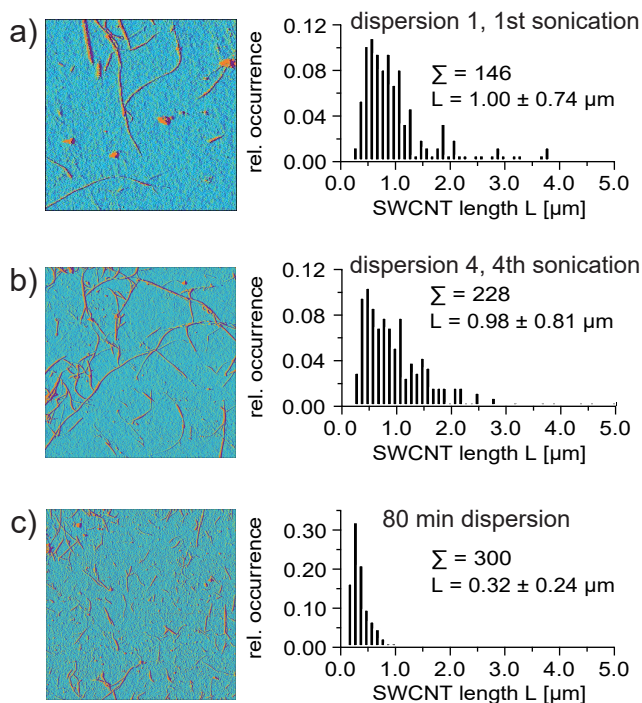


Figure 4.3: AFM micrographs of the SWCNTs extracted from *dispersion 1* (recycling process), *dispersion 4* (recycling process) and the *80 min dispersion* (standard dispersion process). The length histograms were obtained from multiple micrographs. The total occurrence is normalized to 1.

4.2 Raman Defect Study of Recycled SWCNTs

So far, it was demonstrated, that the recycling process is material-efficient. Simultaneously, multiple shorter sonications are not as abrasive with regards to conservation of SWCNT length compared to one long sonication. However, it needs to be clarified if the quality of *dispersion 1* to *dispersion 4* is similar as SWCNTs inside the aggregate might be affected by sonication leading to the introduction of structural defects. Such defects arise from hybridization other than sp^2 . Obviously such defects are expected at those SWCNT ends where the SWCNTs are cut by sonication since these ends do not form semi-spherical end caps. Thus, the defect density is higher at the ends of the SWCNTs. Therefore shorter SWCNTs are expected to exhibit higher defect density, which has been proven by the analysis of the quantum yield of semiconducting SWCNTs with different lengths[182]. Raman spectroscopy is a widely used technique for the analysis of structural defects in SWCNTs. Here, a high intensity of the D-Peak between 1300 and 1400 cm^{-1} would indicate high defect density. Hence, the recycled SWCNT dispersions are investigated by Raman spectroscopy to monitor defect density during sonication treatment as a measure for the material quality.

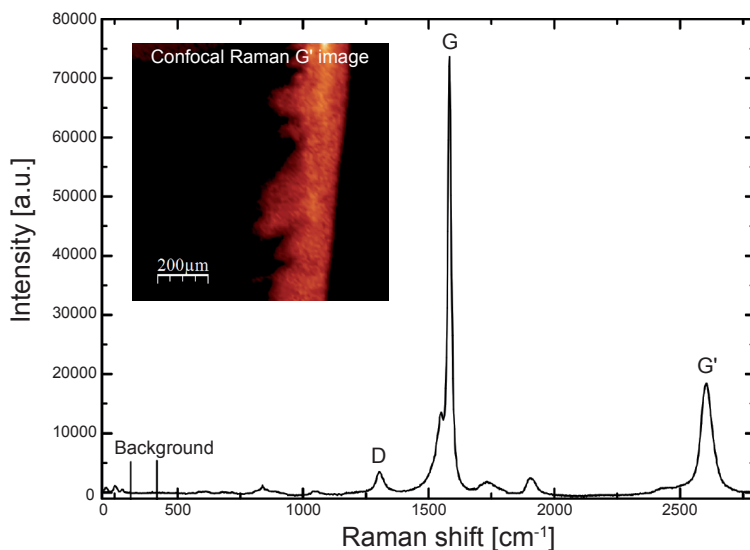


Figure 4.4: Typical raw Raman spectrum. The background count was determined from the average value of the marked area. The inset shows an exemplary confocal Raman G' image of SWCNTs self-assembled by the coffee-ring effect for the Raman investigation.

The Raman investigation was carried out on the inverted confocal microscope described in chapter 2. Droplets of diluted SWCNT solutions were dried on glass coverslides. The excitation was provided by the HeNe laser operating at 632.8 nm. To localize the SWCNTs the G' Raman signal that occurs at about 2650 cm^{-1} was spectrally selected with a band-pass filter centered at 760 nm (10 nm spectral window). The signal is detected with an avalanche photo diode (APD) while rasterscanning the sample (see inset of fig. 4.4). For each sample 50 spectra of SWCNT enriched spots on the sample were taken. The average value of the linear spectral region at $\sim 300\text{ cm}^{-1}$ was chosen for background correction (see fig. 4.4). The peak areas of the D, G and G' Raman signal were chosen and integrated.

In fig. 4.5 the histograms of D/G ratios, which is a measure for the defect concentration in SWCNTs [182, 183, 184, 185, 186, 187], are shown for different sonication treatment. The distributions of D/G ratios for the studied samples show clear peaks. To investigate the effect of increasing sonication time t on the defect concentration, a second SWCNT dispersion was produced with the same process parameters as described earlier for *dispersion 1*. This dispersion, labeled *0 min*, is resonicated for *80 min* and *180 min* with a power of 100 W. The resulting dispersions were labeled accordingly. In the D/G histogram of SWCNTs from dispersions sonicated with different t two trends were observed (see fig. 4.5a): First, a peak shift towards higher D/G ratios that can be attributed to the introduction of defects due to longer sonication (cleaving process). Second, a narrowing of the distribution. While the starting material shows a broad distribution of D/G ratios, a distinct maximum is seen for $t = 180\text{ min}$. This trend is most likely connected to the decrease in the SWCNT lengths and the narrowing of the length distribution observed in the AFM data for increasing t

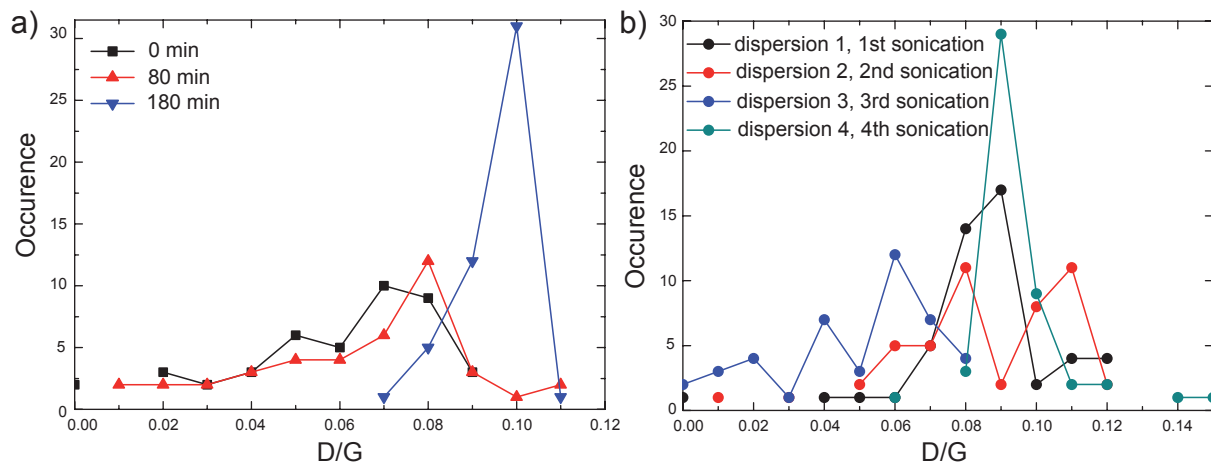


Figure 4.5: Distribution of the D/G intensity ratio of SWCNTs from a) dispersions fabricated with increasing sonication time t , b) dispersions of different recycling steps.

(see fig. 4.3). Similar results for the D/G' ratio confirm these conclusions (see figs. 4.5a and 4.6a). In summary, the increase of the defect density observed in the Raman spectra can be assigned to two effects: a larger relative amount of shorter SWCNTs and increasing defect densities within the SWCNTs. However, the change of the D/G ratio is not as clear as expected from the AFM measurements and results in literature[188, 189].

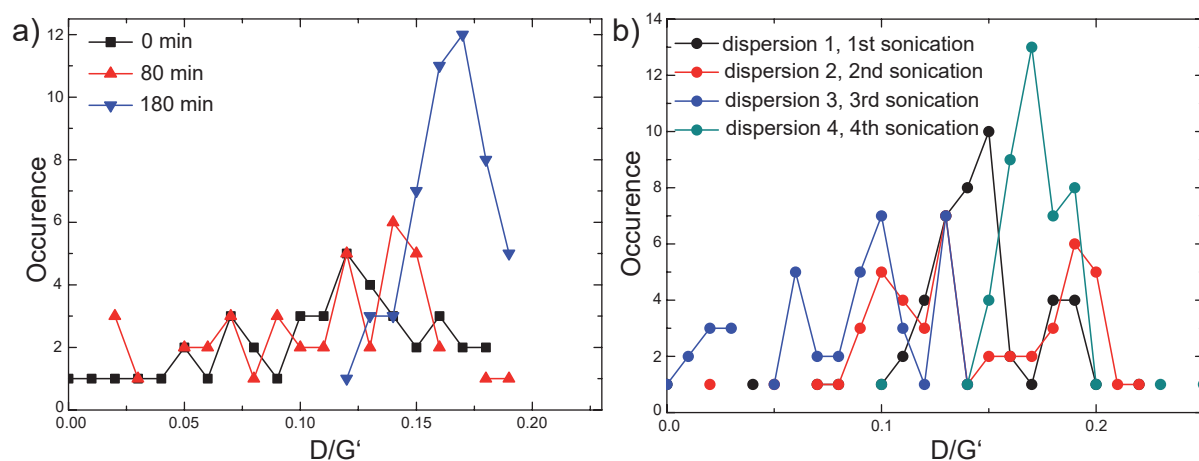


Figure 4.6: Distribution of the D/G' intensity ratio of SWCNTs from a) dispersions fabricated with increasing sonication time t , b) dispersions of different recycling steps.

The histograms of the D/G ratios of the samples recorded for the initial and last recycling step (*dispersion 1* and *dispersion 4*) both peak at around 0.09 with a slightly increased average ratio for the longer sonication time (see fig. 4.5b). Thus, the defect density of the recycled materials appears to be mostly unaffected underlining the applicability of the recycling procedure. This is in agreement with the AFM data for the recycled dispersions that do not show a variation in SWCNT length (fig. 4.3). The D/G ratio distribution for *dispersion 2* and *dispersion 3* are in a similar range, but do not show a clear maximum peak. This can be attributed to statistical noise. Thus, these results do not contradict the previously stated conclusion. The statistics of the D/G' ratio (see fig. 4.6b) are not as distinct as the ones for the D/G ratio, which can also be explained by statistical noise. The same trend is still observable, though.

4.3 Conclusion

The work presented in this chapter shows a simple processing method to produce SWCNT dispersions with a large dispersion yield. Investigations with absorption spectroscopy indicate that the sonication of the precipitate leads to higher dispersion efficiency than in case of the initial raw material. A study of the SWCNT lengths via atomic force microscopy showed that the SWCNT lengths remain constant during the recycling process. In contrast, SWCNTs exposed to long sonication showed significantly shorter lengths. Hence, SWCNTs are not shortended as long as they are agglomerated. Therefore it is possible to obtain the same SWCNT length even if the agglomerates have been sonicated multiples times. Two simultaneous sonication processes are proposed: The crushing process reduces SWCNT aggregates to thin bundles and individual SWCNTs, while the cleaving process shortens SWCNTs by scission. The introduction of defects by sonication was studied by analysis of the Raman D/G and D/G' intensity ratios. The distribution of the ratios for increasing sonication time shows that sonication-induced defects are not only the result of the cleaving process. Raman defect investigation on the recycling process revealed that the defect density is not significantly higher. As SWCNTs are expensive and most of the material remains undispersed after sonication and purification, the proposed recycling method offers a simple and cost-efficient method in order to avoid waste. This is important for both, experimental scientists who carry out experiments in labscale and especially for material engineers who work on scalable production techniques for SWCNT applications such as transparent electrodes or heating elements.

Summary and Outlook

This thesis presents investigations on graphene and SWCNTs using Raman scattering. The aim was to better understand the physical processes occurring during Raman scattering and during ultrasonication of nanocarbon materials. The study of angularly resolved Raman radiation patterns of graphene adds a new aspect to the well-investigated field of graphene Raman spectroscopy and further deepens the understanding of the material system by concentrating on the G and 2D bands. The analysis of the mechanisms occurring during sonication of SWCNTs supports the development of a material-efficient and SWCNT length conserving fabrication procedure of SWCNT dispersions. This would mark an advance towards production of the nanomaterial on the industrial level. Both investigations support the integration process of carbon nanomaterial in photonic and optoelectronic instruments.

Angularly resolved radiation patterns were measured by back focal plane imaging. The radiation pattern, that is formed in the back focal plane of the microscope objective, is thereby projected by a $4f$ configuration for detection. The recorded image is directly connected to momentum space (k-space), providing information about the emissive state. This qualifies back focal plane imaging as a method for the polarization-dependent investigation of graphene Raman scattering.

The first experimental investigation of this thesis addresses the measurement of polarized Raman radiation patterns of graphene. The angular distribution of the non-polarized Raman G band has the shape of a homogeneous ring. This result confirmed the expected isotropic nature of the signal with respect to the polarization of the incident light. Polarized radiation patterns of the Raman G band show a strong resemblance to dipolar radiation patterns. Thus, the G band can be expressed as a superposition of two orthogonal incoherent point-dipoles. The 2D band radiation pattern showed a dependence on the excitation polarization, confirming previous reported spectroscopic results [31]. The shape and intensity distribution of the polarized radiation patterns indicate, that the signal can be described as a sum of two orthogonal incoherent point-dipoles with a weighting ratio of 3:1 or as a sum of three incoherent point-dipoles each rotated by an angle of 120° . These initial results are summed up in fig. ???. The effect of depolarization caused by the air-glass interface and tight focusing with a high NA microscope objective was introduced. Considering this, 2D band Raman tensors and a formula for the determination of the Raman G and 2D intensity was developed. The quantitative intensity study of the polarized Raman

2D radiation patterns revealed a decrease of the polarization contrast with rising NA for both experiment and theory due to depolarization. The influence of depolarization in dependence to the NA is calculated, exhibiting a significant increase at $NA > 1$. This area in the radiation pattern is attributed to angles larger than the critical angle. It was shown, that the polarized Raman 2D/G intensity ratio - an important factor for the determination of single-layer graphene - is also NA dependent. The parallel and perpendicular polarized ratios showed a respective decrease and rise starting from $NA > 1$ due to depolarization. The treatment of the Raman radiation patterns of graphene as spatially incoherent was justified as the spatial coherence length of Raman scattering is substantially smaller than $\lambda/4$. In conclusion, the fraction of detected light as a function of NA was determined.

The first set of Raman tensors for the 2D band were reported. They include the particular photon-electron and electron-phonon coupling of the material. These tensors differ substantially from the often employed totally symmetric Raman tensor that only accounts for symmetry of the phonon mode. The treatment of depolarization in the formula expressing the Raman scattering intensity in graphene is a significant result of this study. This approach along with the terms for the depolarization matrices can be adopted for other low-dimensional systems including transition metal dichalcogenides and SWCNTs. Depolarization generally needs to be considered in a quantitative investigation of emitted intensity using a confocal microscope with high numerical aperture.

Based on the presented results, further investigations could focus on the measurement of Raman radiation patterns enhanced by an optical antenna deposited on graphene. Antenna-enhanced radiation patterns were already measured in a previous investigation [23, 115]. However, the experimental constellation was different as radiation from SWCNT photoluminescence was enhanced by a sharp metal tip in the vicinity of the emitter. Graphene Raman radiation patterns enhanced by a deposited optical antenna could be compared with radiation patterns presented in this thesis and in ref. [23]. *Heeg et al.* intensively studied the plasmon-enhancement of Raman scattering originating from nanocarbon systems. The enhanced Raman signal of strained graphene [190] as well as suspended [191] and unsuspended SWCNTs [192] were analyzed spectroscopically using different plasmonic enhancement systems. The proposed investigation of the angular intensity distribution would add a more detailed view on the enhancement directivity for the radiation of an unstrained emitter system to this discussion. This could provide a better understanding of the processes leading to antenna-enhancement. First experimental steps of this investigation were already conducted. The results so far will be shown in appendix B.

In the second experimental part, a simple and material-efficient processing method for the fabrication of SWCNT dispersions was presented. For this multi-step recycling procedure, precipitates from the dispersion process are redispersed consecutively for the following recycling steps. The new processing approach was compared with the analogous standard dispersion method for different dispersion properties using appropriate characterization techniques. Absorption spectroscopy revealed that similar amounts of SWCNTs are ex-

tracted with both procedures. The statistical study of the SWCNT lengths by atomic force microscopy revealed, that SWCNTs from the initial and final recycling step show similar average lengths ($\approx 1 \mu\text{m}$) and are more than three times longer than SWCNTs from the standard process. The length conservation of SWCNTs from the final recycling step was explained by their central location inside SWCNT agglomerates where they are protected from sonication. Based on these results, two mechanisms describing the sonication of SWCNTs were identified. Both are expected to occur simultaneously. The crushing process reduces SWCNT aggregates to thin bundles and individual SWCNTs. The cleaving process shortens SWCNTs, that are detached from the aggregates, by scission. The introduction of defects by sonication was analyzed by statistical Raman spectroscopy. The Raman D/G intensity ratio correlates to the defect density in the material. The distribution of the ratio for increasing sonication time showed a peak shift towards higher D/G ratios. This reflects the increased shortening of the SWCNTs (cleaving process) and by introduction of defects within SWCNTs. The narrowing of the distribution with increasing sonication time was attributed to the same trend observed for the SWCNT lengths. For the different recycling steps, the statistics exhibited a mostly unaffected defect density. Analogous to the conservation of SWCNT lengths for different recycling steps, this was explained by the protection from sonication due to the central location of the analyzed SWCNTs in the agglomerate. A further statistical Raman investigation for the D/G' intensity ratio confirmed the stated results. The experimental results are summed up in fig. ??).

The results found during this study allow for a reduction of the considerable costs for the fabrication of SWCNT dispersions and simultaneously avoids waste. In addition, SWCNTs from this process exhibit larger mean lengths. This leads to a higher conductivity of SWCNT films, which is beneficial for the optoelectronic performance of SWCNT devices [171]. The presented investigation supports experimental scientists fabricating SWCNTs in lab-scale as well as material engineers working on scalable production techniques for SWCNT applications such as transparent electrodes [156, 157, 158], transistors [159, 160, 161] or heating elements[164].

Future investigations could address the optimization of the presented recycling procedure. The investigated SWCNT dispersion properties could be improved further by the variation of experimental parameters like sonication power and time leading to longer average SWCNT length, reduced amount of sonication-induced defects and higher dispersion yield. The latter is expected to increase with a rising number of recycling steps. However, the amount of extracted SWCNTs per recycling step is expected to decrease in late steps due to the continuous reduction of SWCNTs in the precipitate with each recycling step (see absorption spectra of recycled dispersions). For the determination of the optimal number of recycling steps, economic aspects need to be considered as the material extraction for higher number of recycling steps (>6 steps) does not compensate for the energy input. The dispersions of late recycling steps are also expected to contain SWCNTs with a reduced average length and increased defect density. This could result from the low amount of SWCNTs in the initial precipitate not allowing for the formation of large SWCNT clusters,

which protect SWCNTs from scission and defect introduction (cleaving process).

Appendix A

Simulation of Polarized Radiation Patterns

Figure A.1 depicts radiation patterns corresponding to the four different in-plane point-dipoles $\Phi=0^\circ$ (x-dipole), $\Phi=90^\circ$ (y-dipole), $\Phi=45^\circ$ and $\Phi=315^\circ$. Non-polarized and polarized intensity patterns are illustrated. The polarized patterns are simulated for an analyzer orientation along the x- and y-axis. A sum of the corresponding x- and y-polarized contributions results in the non-polarized radiation pattern. For the forming of polarized radiation patterns two contributing components need to be distinguished: the dipole emission and the depolarization. These components can be isolated for analyzer orientations parallel and perpendicular to the orientation of the point-dipole. The pattern caused by the dipole emission component (parallel dipole to analyzer orientation) resembles its respective non-polarized counterpart with less extended maxima. As discussed in the main part of the thesis, the position of the extrema in the pattern depends on the orientation of the point-dipole. The pattern resulting from depolarization (perpendicular dipole to analyzer orientation) does not depend on the dipole orientation. It features four lobes at the high NA area.

Other polarized patterns are composed of both dipole emission and depolarization components. Their shape resembles a rotated parallel polarized radiation pattern. The tilt between the x- and y-polarized radiation pattern is resulting from the depolarization component. To understand the origin of the tilt, the phase of the electric field E needs to be considered. The E pattern of the dipole emission component (parallel case) shows no phase difference and resembles the shape of the corresponding polarized intensity pattern. Depending on the orientation of the point-dipole, the corresponding parallel polarized E pattern is obtained by rotating E_x of the x-dipole by the angle Φ . The four lobes of the depolarized pattern shows two phases (red and blue) with two opposing lobes having the same phase. When summing up the E patterns of the dipole emission and depolarization component the electric fields interfere constructively and destructively resulting in the tilt.

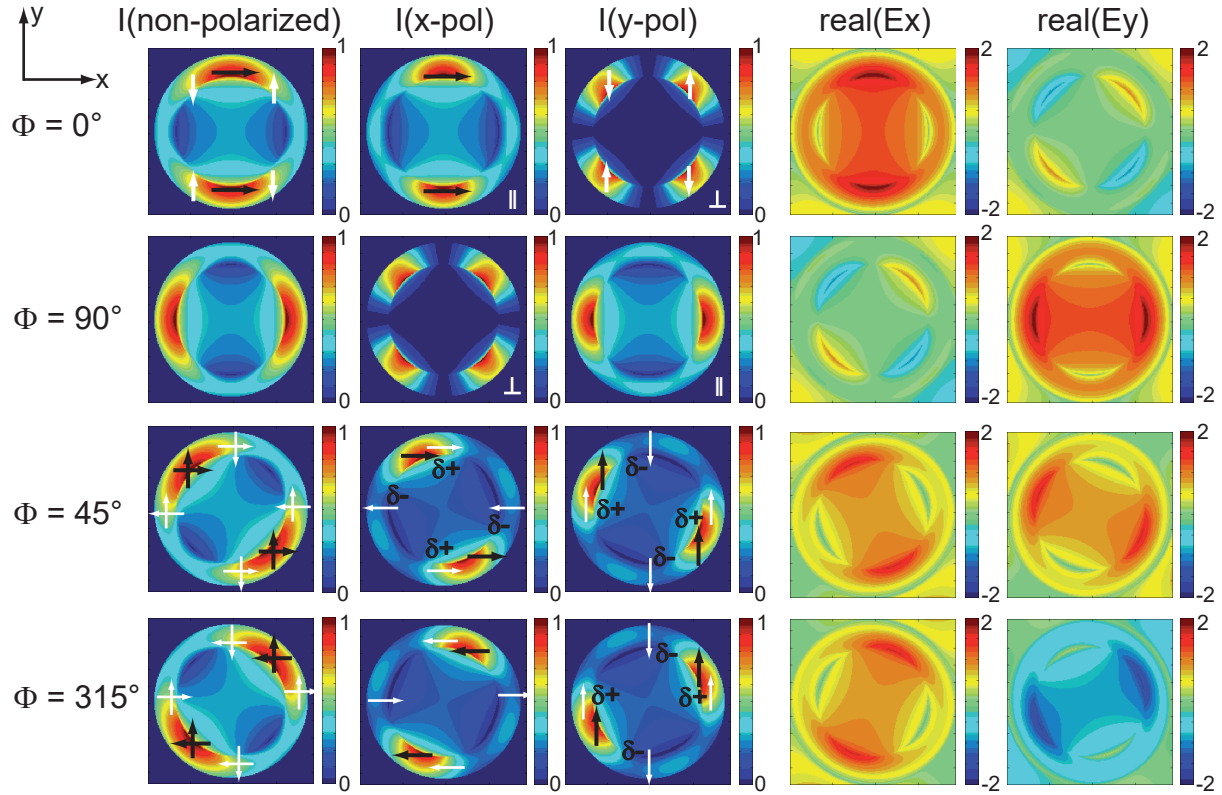


Figure A.1: Radiation patterns calculated for in-plane point-dipoles with $\Phi=0^\circ$, $\Phi=90^\circ$, $\Phi=45^\circ$ and $\Phi=315^\circ$. The first three columns show the non-polarized, x-polarized ($E_y=0$) and y-polarized ($E_x=0$) radiation patterns. Parallel and perpendicular polarized patterns show the radiation components of dipole emission (black arrows) and depolarization (white arrows), respectively. Polarized radiation patterns with a dipole to analyzer orientation other than parallel and perpendicular are formed by summing up both radiation components. The fourth and fifth column shows the real parts of E_x and E_y . The phase difference of the depolarization component explains the tilt seen for the polarized radiation patterns of point-dipoles with the orientation $\Phi=45^\circ$ and $\Phi=315^\circ$.

A more detailed discussion about non-polarized and polarized intensity patterns is part of sections 2.3.3 and 3.1.

The Matlab script to calculate the back focal plane patterns of single dipoles on a substrate according to *A. Lieb et.al. J. Opt. Soc. Am. B* 2004, 6, 1210 [22] is shown in the following. In addition, it is possible to calculate polarized (x-/y-adjustment shown in section 3.1) and summed up radiation patterns (needed for simulated Raman radiation patterns of graphene, see section 3).

programmed by Nicolai Hartmann (2013/07/18) and Harald Budde (2014/07/04)

Options

saveoption = 'none'; [option to save the resulting intensity/field maps (cases: I, E, IE, none)]

savename = 'Single_dipole';

System parameters

numberofpoints = 193; [number of points in one direction]

k_range = 1.5; [range of k space in units of $k/k_0 = \text{NA}$]

Input dipole properties

lambda = 760e-9; [emission wavelength of the dipole]

angle_inplane1 = 0*pi/180; [azimuthal angle (Φ) of the dipole]

angle_outplane = 90*pi/180; [polar angle (Θ) of the dipole]

delta = 1e-9; [distance of the dipole from the interface [m]]

n_objective = 1.518; [refractive index of the microscope objective/cover glass/oil]

n_cover = 1; [refractive index of the surrounding upper medium]

NA = 1.4; [numerical aperture of the microscope objective]

Precalculations

Parameters

$k_0 = 2\pi/\lambda$; [vacuum wavevector]

$n = n_{\text{objective}}/n_{\text{cover}}$; [relative index of refraction]

$(n = n_{\text{cover}}/n_{\text{objective}})$; [inverse n for upper halfspace]

$f = n_{\text{objective}} \cdot k_0$; [focal length of the objective]

$k_{\text{max}} = k_0 \cdot \text{NA}$; [$n_{\text{objective}}$; maximum k value for the objective lens]

Coordinate system in k-space

$k_x = \text{linspace}(-k_{\text{range}} \cdot k_0, k_{\text{range}} \cdot k_0, \text{numberofpoints})$;

$k_y = \text{linspace}(-k_{\text{range}} \cdot k_0, k_{\text{range}} \cdot k_0, \text{numberofpoints})$;

$[K_x, K_y] = \text{meshgrid}(k_x, k_y)$;

$\text{NA_mask} = (K_x.^2 + K_y.^2) \leq k_{\text{max}}^2$; [mask for maximum NA]

Creating coordinate system in angles

[PHI,RHO]=cart2pol(Kx,Ky);

THETA = asin(RHO./f);

Intensity and field calculation

THETA_S = asin((n_objective/n_cover).*sin(THETA)); [complex valued angle according to Snell's law]

Fresnel transmission coefficients

tp = (2.*n_cover.*cos(THETA_S))./(n_cover.*cos(THETA) + n_objective.*cos(THETA_S));

ts = (2.*n_cover.*cos(THETA_S))./(n_cover.*cos(THETA_S) + n_objective.*cos(THETA));

Propagation factor

PI = exp(1i.*k_0.*n_cover.*cos(THETA_S).*delta);

c coefficients

c1 = (n.^2).*(cos(THETA)./cos(THETA_S)).*tp.*PI;

c2 = n.*tp.*PI;

c3 = -n.*(cos(THETA)./cos(THETA_S)).*ts.*PI;

E-fields

Ep1 = (c1.*cos(angle_outplane).*sin(THETA))+(c2.*sin(angle_outplane).*cos(THETA).*cos((PHI - angle_inplane1)));

Es1 = c3.*sin(angle_outplane).*sin(PHI - angle_inplane1);

Adjustment of x/y-components of E-field

Ex1 = Ep1.*cos(PHI) - Es1.*sin(PHI);

Ey1 = Ep1.*sin(PHI) + Es1.*cos(PHI);

Polarized detection

Ey1 = 0; or Ex1 = 0;

I1 = (1./cos(THETA)).*((Ex1.*conj(Ex1)+Ey1.*conj(Ey1)));

Calculations for the 2nd Dipole

Parameters

angle_inplane2 = 90*pi/180; [azimuthal angle (Phi) of the dipole]

E-fields

Ep2 = (c1.*cos(angle_outplane).*sin(THETA))+(c2.*sin(angle_outplane).*cos(THETA).*cos((PHI - angle_inplane2)));

Es2 = c3.*sin(angle_outplane).*sin(PHI - angle_inplane2);

Adjustment of x/y-components of E-field

$$E_{x2} = E_p^2 \cdot \cos(\text{PHI}) - E_s^2 \cdot \sin(\text{PHI});$$

$$E_{y2} = E_p^2 \cdot \sin(\text{PHI}) + E_s^2 \cdot \cos(\text{PHI});$$

Polarized detection

$$E_{y2} = 0; \text{ or } E_{x2} = 0;$$

$$I_2 = (1./\cos(\text{THETA})) \cdot ((E_{x2} \cdot \text{conj}(E_{x2}) + E_{y2} \cdot \text{conj}(E_{y2})));$$

Summing up Dipole1 and Dipole2

$$I = I_1 + I_2; \text{ [equally weighted dipoles]}$$

$$\text{or } I = (I_1 + 1/3 \cdot I_2); \text{ [differently weighted dipoles]}$$

Adjustments

$$I = I \cdot \text{NA_mask};$$

$$\text{Int_I} = \text{sum}(\text{sum}(I));$$

Plotting

```
figure(108)
sp01=pcolor(Kx./k_0,Ky./k_0,I); caxis ([0 5]);
sp01cb = colorbar;
title(['intensity map integral: ' num2str(Int_I)])
xlabel('k_x/k_0');
ylabel('k_y/k_0');
set(get(sp01cb,'ylabel'),'String', 'intensity [a.u.]');
shading flat
axis image
colormap jet
```

```
figure(102)
sp02=pcolor(Kx,Ky,real(Ep));
sp02cb = colorbar;
vtitle('Re(E_p)')
xlabel('k_x [m^-1]');
ylabel('k_y [m^-1]');
set(get(sp02cb,'ylabel'),'String', 'amplitude [a.u.]');
shading flat
axis image
colormap jet
```

```
figure(103)
sp03=pcolor(Kx,Ky,real(Es));
sp03cb = colorbar;
```

```

title('Re(E_s)')
xlabel('k_x [m^-1]');
ylabel('k_y [m^-1]');
set(get(sp03cb,'ylabel'),'String', 'amplitude [a.u.]');
shading flat
axis image
colormap jet

```

Saving

Switch saveoption

```

case 'I'
savenameI = [savename '_I.txt'];
save(savenameI,'I','-ascii')
case 'E'
savenameEp = [savename '_Ep.txt'];
savenameEs = [savename '_Es.txt'];
Ep = real(Ep);
Es = real(Es);
save(savenameEp,'Ep','-ascii')
save(savenameEs,'Es','-ascii')
case 'IE'
savenameI = [savename '_I.txt'];
savenameEp = [savename '_Ep.txt'];
savenameEs = [savename '_Es.txt'];
Ep = real(Ep);
Es = real(Es);
save(savenameI,'I','-ascii')
save(savenameEp,'Ep','-ascii')
save(savenameEs,'Es','-ascii')
case 'none'

```

The following table lists the specifications of the **tube lens**, integrated in the optical microscope Eclipse TE2000 (Nikon), with r , d and h being the radius of curvature, the thickness and the semi diameter height, respectively [193, 194, 195, 196, 197, 140, 198, 199, 200, 201, 202]:

Surface	r(mm)	d(mm)	h(mm)	Glass	Manufacturer
1	75.043	5.1	15.9385	E-SK10	Hikari
2	-75.043	2	15.9385	J-LAF7	Hikari
3	1600.58	7.5	15.9385		
4	50.256	5.1	15.9385	BASF6	Schott

The specifications of the **Nikon plan apo objective**, used for recording the radiation patterns in chapter 3 (60x magnification, 1.4 NA) are listed in the following table [140, 126]. The surfaces where an exact glass match could not be obtained, the index and Abbe number are given at the d-line instead.

Surface	r(mm)	d(mm)	h(mm)	Glass	Manufacturer
1	Infinity	0.17	0.183	1.52216, 58.80	
2	Infinity	0.15	0.39834	1.51536, 41.36	
3	Infinity	0.65	0.76209	S-NSL3	Ohara
4	-1.332	3.6	1.0598	LASF35	Schott
5	-3.716	0.1	3.6153		
6	-13.716	3.75	5.6585	GFK70	Sumita
7	-7.247	0.1	6.4791		
8	-27.891	1	7.8796	J-F5	Hikari
9	34.23	6.8	9.2544	GFK70	Sumita
10	-13.453	0.15	9.7985		
11	-84.754	1	10.2849	J-KZFH1	Hikari
12	20.048	9.4	10.8992	LITHO-CAF2	Schott
13	-16.266	0.15	11.288		
14	47.671	1.1	11.0093	J-KZFH1	Hikari
15	14.802	8	10.5143	LITHO-CAF2	Schott
16	-28.664	0.1	10.4895		
17	18.671	1.6	9.5306	J-KZFH1	Hikari
18	11.816	6.3	8.6046	LITHO-CAF2	Schott
19	-48.478	1	8.0904	1.526820, 51.35	
20	25.246	0.15	7.4167		
21	8.784	5.2	6.9181	GFK70	Sumita
22	-238.404	5	6.0015	S-LAH63	Ohara
23	4.823	3.4	3.2407		
24	-4.801	2.6	3.1155	S-LAH63	Ohara
25	204.674	3	4.2684	FD60-W	Hoya
26	-8.172		4.7147		

Appendix B

Antenna-enhanced Raman Radiation Patterns of Graphene

In the presence of an optical antenna the interaction between light and matter is strongly influenced. Modifications of the emission process include the amplification of the transition rates and the change of the spectral response. In addition, the propagation direction of incident and emitted light is varied. This particular change of the radiation characteristics can be observed in the angular distribution of emission at the back focal plane. For the case of dipolar emission the relative orientation of antenna and emitter plays a major role. *Böhmler et al.* investigated this for a perpendicular antenna-emitter orientation [23]. Photoluminescence (PL) of SWCNTs oriented in the sample plane was shown to behave like dipolar radiation. Antenna-enhancement was provided by a sharp gold tip in close vicinity above the SWCNT. The radiation of the coupled system could be divided into two dipolar components oriented along the SWCNT (x,y plane) and the antenna (z), respectively. An approach of the antenna towards the dipolar emitter was found to result in the amplification of the z-dipolar radiation component [124].

In contrast to the PL of a SWCNT, the Raman G signal of graphene shows isotropic radiation neither depending on the in-plane orientation of the graphene sheet nor on laser polarization [31, 92, 151] (see also chapter 3). However, both signals can be expressed by point-dipoles. This also accounts for tip-enhanced point-dipolar radiation [124, 23]. This implicates that an antenna-enhanced graphene Raman G radiation pattern can also be expressed by point-dipoles. Orienting the antenna in the sample plane should provide a non-uniform enhancement of the Raman G signal in the back focal plane. The antenna-effect for this experimental constellation was already investigated by *Heeg et al.* [190] considering the aspects of signal enhancement and spectral shift. However, the effect of spatial redirection still needs to be discussed. The angle-dependent radiation study of the graphene Raman G signal enhanced by optical antennas oriented in the sample plane should thus provide a better insight on the antenna-induced directivity change of radiation and antenna-enhanced Raman scattering in general.

This chapter is divided into three sections. First, optical antennas and their influence on radiation patterns will be briefly introduced. The change of propagation direction and the dipolar description of the resulting radiation pattern will be emphasized. In the following section, the deposition of gold nanorods on graphene and their localization and identification as single oriented particles will be presented. Finally, the angular distribution of the graphene Raman G signal enhanced by deposited gold nanorods will be discussed.

B.1 State of the Art - Optical Antennas and Their Influence on Radiation Patterns

The information provided in this chapter is based on ref. [115] and ref. [124].

The first antennas were built by the physicist *Heinrich Hertz* with the purpose of verifying the existence of electromagnetic waves [203]. Antennas rapidly became significant components for wireless communication with the function of sending and receiving radio waves. In general, antennas can be described as an intermediate resonator between far-field radiation and local fields. For the application of radio broadcasting, radio waves and electrical current can be transformed into each other. The working principle of an antenna is depicted in fig. B.1a.

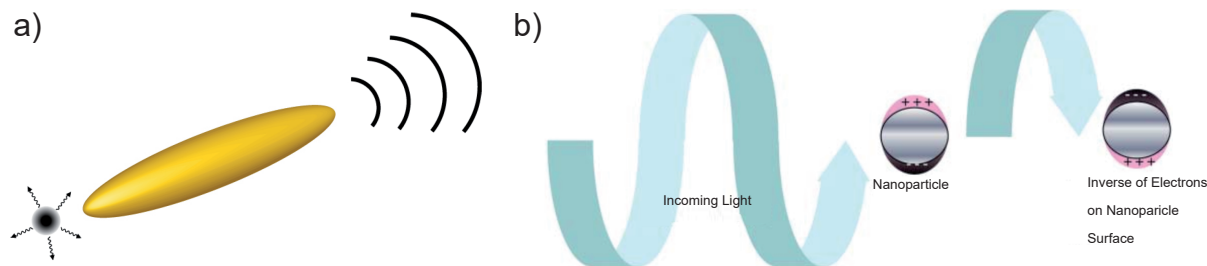


Figure B.1: Understanding optical antennas. a) Principle of an antenna: Conversion of freely propagating electromagnetic radiation into localized energy and vice versa, b) Origin of the surface plasmon resonance for nanoparticles: Incident light excites the collective oscillation of the electron gas. Figures adapted from ref. [204] and ref. [205].

This concept was transferred to near-field microscopy by *J. Wessel* [206]. For this application, antennas were required to work in the optical regime. Due to the correlation between the antenna dimensions (especially the antenna length L) and the wavelength λ of the propagating waves optical antennas need to be sized in the nanometer range. However, at this scale metals can not be considered as perfect conductors, because the penetration depth of fields into the metal is as large as the antenna size. For wavelengths much larger than the particle size, resonance conditions with surface plasmons can be set up. The interaction of surface plasmon resonant light with the free electrons in the conduction band

leads to coherent oscillations as depicted in fig. B.1b [205]. The collective electron movement generates a local electromagnetic field, which leads to the enhancement of radiation (antenna effect).

For the correlation between antenna size and wavelength at the nanometer range the effective wavelength λ_{eff} is introduced. Thereby λ_{eff} is smaller than λ of the propagating light [207]. Their correlation is given by

$$\lambda_{eff} = f_1 + f_2 \frac{\lambda}{\lambda_p} \quad (\text{B.1})$$

f_1 and f_2 are geometrical scaling factors associated with the antenna properties. λ_p is the plasmon resonance.

The enhancement process of radiation from the antenna-coupled emitter system strongly depends on antenna properties. Parameters such as material, structure, shape and size of the antenna as well as its orientation and distance relative to the emitter influence light-matter interactions.

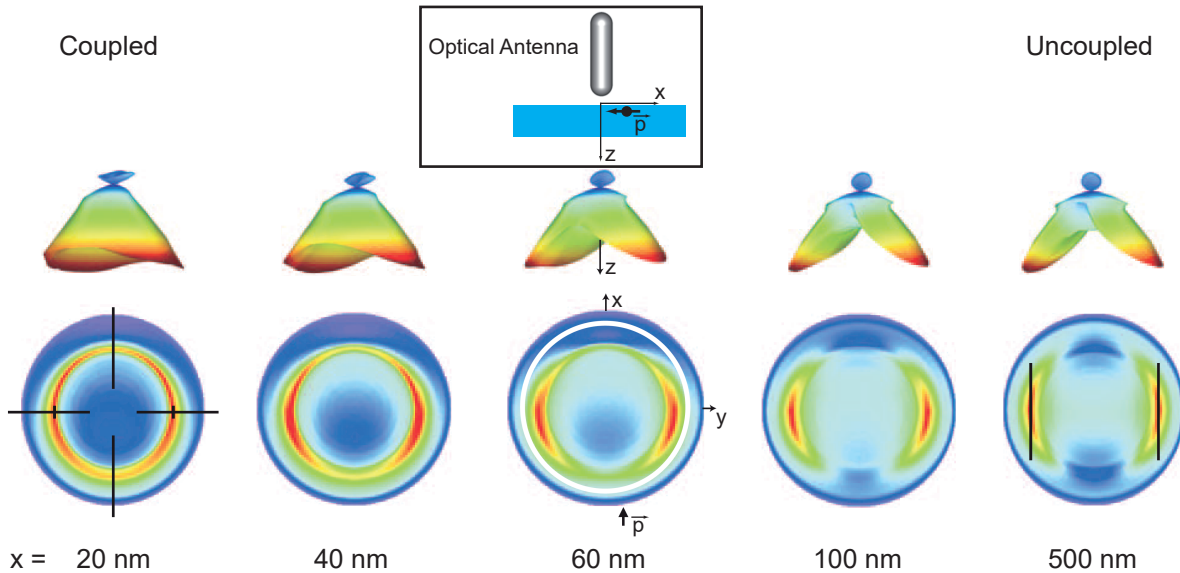


Figure B.2: FIT calculations of the electromagnetic fields from an emitter with dipole momentum $\vec{p} \parallel x$ below a z -oriented antenna with distance x from the emitter. The inset depicts the emitter situation. The top row shows three-dimensional radiation intensity patterns. The bottom row presents the intensity in the back focal plane. The white circle in the middle image encloses the emission detected with a $\text{NA} = 1.3$ microscope objective. The magnitude of the contributions polarized along x and y of the main lobes is marked in black for $x = 20$ and $x = 500$ nm (black lines). Figure adapted from ref. [124].

The correlation of antenna-emitter distance on the angular distribution of the radiation was investigated by *Taminiau et al.* [124]. Full three-dimensional finite-integration technique (FIT) electromagnetic field calculations were performed for an optical antenna situated above a point-dipole \vec{p} on a glass substrate with varying antenna-emitter distances x (see fig. B.2). The dipole is oriented along x also observable in the radiation pattern of the uncoupled emitter. With the reduction of the distance x the angular distribution gradually changes. For maximal coupling ($x=20$ nm) the radiation pattern resembles the angular distribution of a z -dipole with an almost circular polarization. Thus, the strength of the antenna-emitter coupling can be correlated to the degree of polarization which decreases for an antenna approaching the emitter. The angular emission of a coupled antenna-emitter system was found to be dominated by the antenna mode, regardless of the emitter orientation.

A more detailed description of optical antennas can be found in ref. [208].

B.2 Deposition, Localization and Identification of Single Gold Nanorods

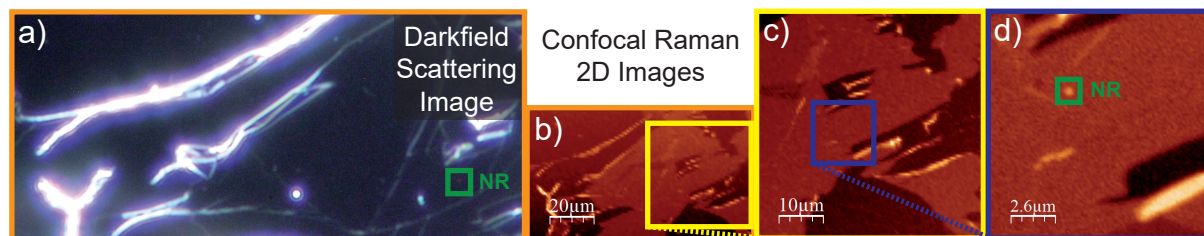


Figure B.3: Localization of a single gold nanorod deposited on graphene, a) Darkfield scattering image of a single gold nanorod (marked in green) on graphene. Cracks, introduced to graphene during sample fabrication, were visualized in overexposed images. This is used to distinguish nanorods on glass and graphene b) - d) Confocal Raman 2D images of the localized area zooming in on the nanorod.

This section shows first experimental steps towards the measurement of graphene Raman radiation patterns enhanced by a single gold nanorod. For this study, extended CVD-grown graphene was used instead of exfoliated graphene to increase the chances of successfully depositing the optical antenna (for experimental details see section 2.1.3 for graphene and section 2.1.2 for gold nanorods). Gold nanorods resonating at 630 nm on glass enclosed by cetyltrimethylammonium bromide (CTAB) ligand were chosen. Attractive electrostatic interactions of the graphene p_z orbital electrons with the positively charged ligand support the successful deposition of the gold nanorod on graphene. In addition, the attractive forces retain the nanoparticle on graphene during the removal of the excess nanorod solution from the sample. For the deposition 50 μL of the diluted (1:1000) aqueous gold

nanorod solution was dried on the sample for 5 min. Residual nanorod solution was removed with nitrogen gas.

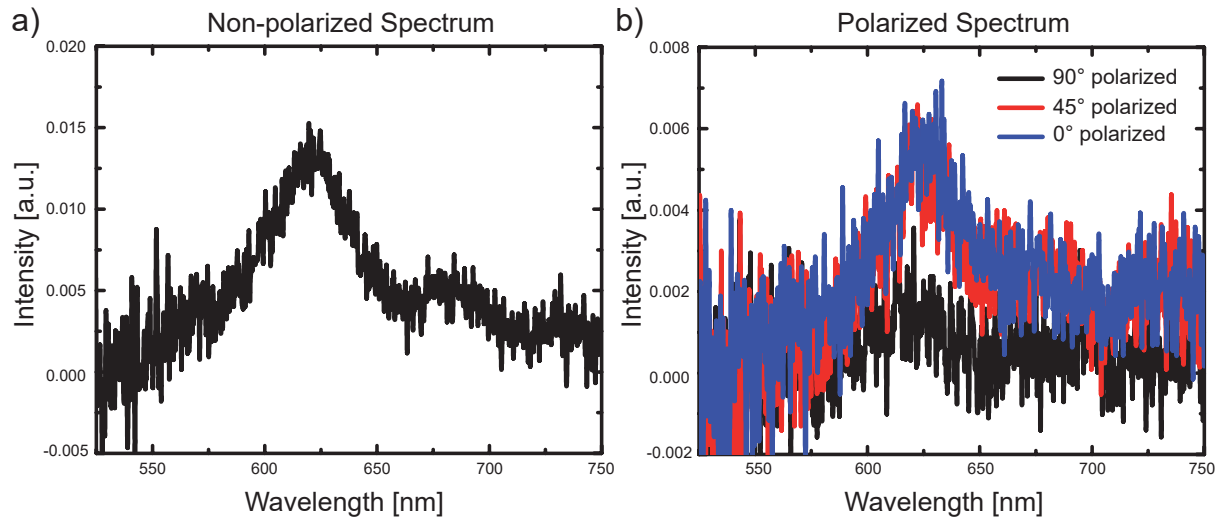


Figure B.4: a) Non-polarized and b) polarized darkfield scattering spectrum of a single Au nanorod.

For the localization of single gold nanorods on graphene the sample was investigated with a darkfield scattering microscope operated by **Dr. M. Pilo-Pais**. The large field of view and high material contrast of this microscope allowed for a fast detection of the deposited nanoparticles. In the microscope, the nanorods appear as faint red dots due to the nanorod resonance at 630 nm. Graphene cracks that originate from sample preparation (PMMA-transfer onto glass) were visualized in overexposed darkfield scattering images. This was used as a means to distinguish nanorods deposited on graphene or on glass. Further refinement of the selection process was attained by rotating an analyzer in the detection beam path of the darkfield microscope. Signals showing no intensity variation were disregarded as clusters of unoriented nanorods. Polarization-dependent behavior of the scattered light could originate from a single nanorod or clusters of oriented nanorods. A nanorod that fulfills the stated conditions is shown in a darkfield scattering image illustrated in fig. B.3a. The darkfield scattering spectrum of the nanoparticle its resonance at 625 nm (see fig. B.4a). The polarized spectrum of the nanorod for different analyzer directions showed varying intensity (see fig. B.4b). Increased intensity was observed for the analyzer directions 45° and 90°. This infers that the nanorod is oriented in the angular range between both analyzer directions. Because of the polarization-dependent behavior and the relatively low intensity compared to other investigated spots it is assumed that the enhancement of the detected signal originates from a single gold nanorod. For a clear identification as a single particle it is required to investigate the analyzed sample position by scanning electron microscopy (SEM). As the required preparation and conduction of the measurement is associated with significant changes of the sample the investigation of

radiation patterns should be completed first.

To precisely position the sample for the angle-dependent investigation enhanced Raman G band, the location of the previously studied gold nanorod was scanned with a confocal microscope. Features of the area that were observed in the darkfield scattering image could be found in the Raman 2D scattering image confirming the correct confocal re-localization (see fig. B.3a and b). Fig. B.3c and d depict Raman scattering images zooming in on the gold nanorod. The marked spot in d) was identified in the Raman spectrum (not shown) as the nanorod analyzed in the darkfield study.

B.3 Raman G Radiation Patterns Enhanced by Deposited Gold Nanorods

In another study using gold nanorods with a different resonance (see section 2.1.2 for more details) antenna-enhanced Raman G radiation patterns of graphene were recorded. The coupling to the plasmon of the antenna is expected to influence the transition rates of the emission. The change of the angular distribution is unlikely to vary for different plasmon resonances of nanorods with the same dipole orientation. Whether the enhancement was provided by a single gold nanorod or by an agglomerate of oriented nanorods has not been confirmed yet. The nanorod dimensions were adjusted by synthetic control so that the nanoparticles exhibit an average plasmon resonance of 780 nm on glass. The absorption spectrum of the aqueous nanorod solution shows a maximum peak at ~ 760 nm attributed to the longitudinal plasmon mode (see fig. B.5a). The resonance shift for different nanorod environments is due to their different refractive indices (for more details about the redshift of plasmonic particles on a substrate see ref. [209]). Fig. B.5b illustrates a confocal Raman G scattering image of graphene with deposited gold nanorods. With Raman spectroscopy both the dark region and the spots of increased intensity were identified as graphene (spectra not shown). The spots depict the nanorods enhancing the graphene Raman signal. The investigated nanorod is marked in the image.

Raman G radiation patterns measured at the antenna distance $x = 700$ nm and $x = 400$ nm as well as the pattern on the nanorod are shown in fig. B.6a, b and c, respectively. According to the results of *Taminiau et al.* the antenna-emitter system is uncoupled at a distance larger than 500 nm (see fig. B.2) [124]. The corresponding radiation pattern shows increased intensity for lower angles that is attributed to laser radiation passing the optical filters. Due to the large extension of CVD-graphene covering the whole scanning range the reference image was measured on graphene instead of glass. Hence, the unblocked laser signal could not be corrected for due to absorption and scattering at graphene. In addition to that, the sample condition at different graphene locations varies (e.g. different defect density). Thus, the reference and measurement positions on graphene are not comparable.

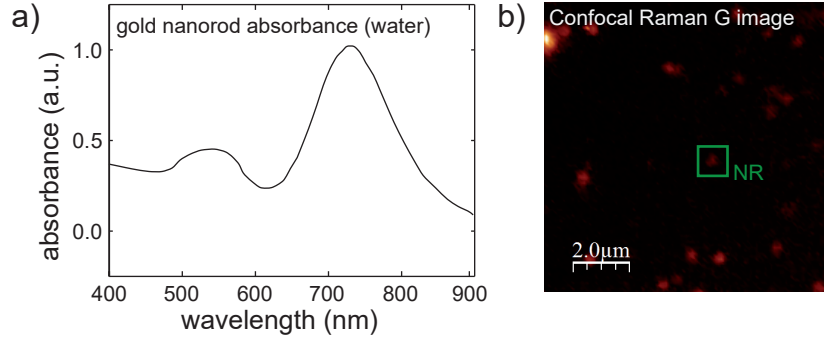


Figure B.5: a) Absorption spectrum of gold nanorods resonating at 780 nm (on glass) in aqueous solution, b) Confocal Raman G image of graphene with deposited gold nanorods.

Thus, background correction for the investigated location is difficult. However, this study concentrates on information about the polarizing state of the emission which is associated with the area at $NA > 1$. For this zone, homogeneous intensity was observed. This is expected for uncoupled graphene Raman G scattering see chapter 3. Hence, background correction for this area is assumed to be sufficient for the purposes of this study.

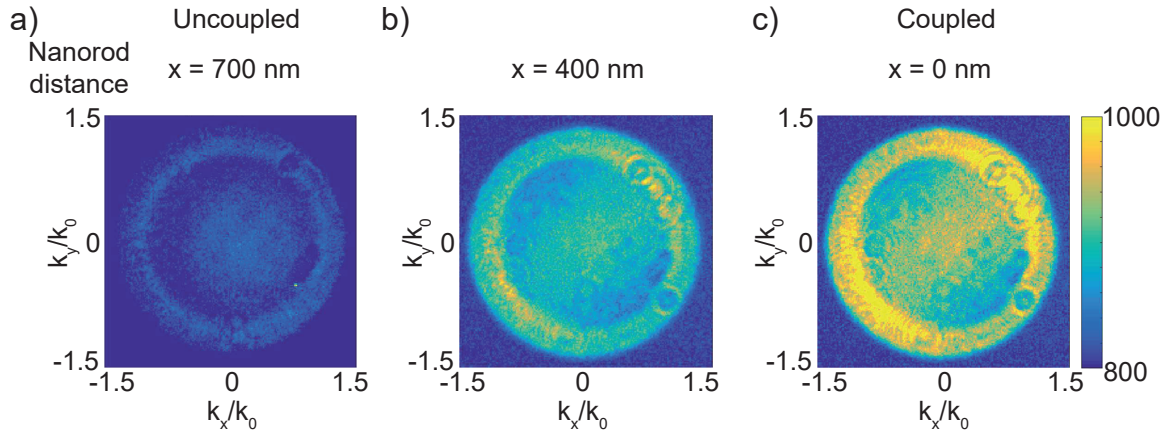


Figure B.6: Raman G radiation pattern of graphene recorded at antenna distance x . a) $x=700$ nm, b) $x=400$ nm, c) $x=0$ nm.

Compared to this, signal intensities at the positions $x=400$ nm and $x=0$ nm are weakly amplified by the respective factors 1.03 and 1.14 due to increased coupling to the nanorod. Both radiation patterns feature a double-lobe on comparable positions indicating a similar dipole orientation. The radiation patterns reflect the orientation of the gold nanorod. This is explained by stronger enhancement of radiation components parallel to the nanorod axis and weaker enhancement for the perpendicular component. When considering the Raman G band as a sum of two orthogonal point-dipoles (see chapter 3) both can be aligned parallel and perpendicular to the nanorod axis. For this approach, the parallel dipole is

weighted stronger than the perpendicular dipole.

For the enhanced radiation patterns the average intensity at the lobes are determined. This value is divided by the average intensity of the non-lobe area at the same NA range to estimate the grade of polarization. For $x=400$ nm and $x=0$ nm the patterns exhibit respective ratios of 1.12 and 1.21 indicating an increase of the grade of polarization for stronger coupling. This is in contrast to the investigations of *Taminiau et al.* [124] where increased antenna-coupling is associated to a reduction of the grade of polarization (see fig. B.2). This is understood when the antenna-emitter configuration of both experiments is considered. For the present situation the emitter shows an isotrope signal and the enhancement is anisotrope, while the situation is inverse for a dipolar emitter enhanced by an antenna oriented along z .

B.4 Conclusion and Outlook

In this chapter, first experimental steps towards the measurement of Raman radiation patterns enhanced by deposited gold nanorods were presented. The deposited gold nanorods on graphene were localized and identified by darkfield scattering microscopy. Oriented nanorods were distinguished by polarized darkfield scattering spectroscopy. For the measurement of the enhanced radiation patterns the position of the previously investigated nanorod was re-localized by confocal Raman imaging. Raman G radiation patterns at different distances to oriented gold nanorods were recorded. When reducing the antenna distance an increase of the enhancement factor and grade of polarization was observed. These are attributed to stronger antenna-emitter coupling.

Future investigations should include the determination of nanorod orientation and verification that the enhancement is provided by a single nanoparticle (SEM study). For a better background correction the deposition of the nanorod close to the edge of graphene would be beneficial. The analogous study of the Raman 2D band is expected to show a complex angular intensity distribution due to the polarization-dependence of the signal that needs to be considered. As both the antenna-enhancement and polarization-dependence can be expressed by dipoles the corresponding pattern is expected to be a superposition of multiple differently weighted point-dipoles.

The investigation presented here contributes to a better understanding of the change in propagation direction induced by the antenna-effect. In addition, this study helps in gaining more insight about the enhancement process of graphene Raman scattering.

Bibliography

- [1] S. Weiss. Measuring Conformational Dynamics of Biomolecules by Single Molecule Fluorescence Spectroscopy. *Nature Struct. Biol.*, 7:724–729, 2000.
- [2] P. Tamarat, A. Maali, B. Lounis, and M. Orrit. Ten Years of Single-Molecule Fluorescence Spectroscopy. *J. Phys. Chem. A*, 104:1–16, 2000.
- [3] W. Zinth and U. Zinth. *Optik: Lichtstrahlen - Wellen - Photonen*. Oldenbourg Verlag, 2012.
- [4] J. Tyndall. *The Glaciers of the Alps*. Longmans, Green, and Co., 1860.
- [5] J. Strutt. On the Light from the Sky, its Polarization and Colour. *Philos. Mag.*, 41:107–120, 1871.
- [6] J. Strutt. On the Scattering of Light by Small Particles. *Philos. Mag.*, 41:447–454, 1871.
- [7] J. Strutt. On the Electromagnetic Theory of Light. *Philos. Mag.*, 12:81–101, 1881.
- [8] J. Strutt. On the Transmission of Light through an Atmosphere Containing Small Particles in Suspension, and on the Origin of the Blue of the Sky. *Philos. Mag.*, 47:375–394, 1899.
- [9] Leon Brillouin. Diffusion de la lumiere et des rayonnements X par un corps transparent homogène; influence de l'agitation thermique. *Ann. Phys. (Paris)*, 17:88, 1922.
- [10] W. Schmidt. *Optische Spektroskopie - Eine Einführung*. Wiley-VCH, 2000.
- [11] A. Smekal. Zur Quantentheorie der Dispersion. *Naturwissenschaften*, 43:873–875, 1923.
- [12] V. Raman. The Molecular Scattering of Light. *Nobel Lecture*, 1930.
- [13] S. A. Acharya, N. Maheshwari, L. Tatikondewar, A. Kshirsagar, and S. K. Kulkarni. Ethylenediamine-Mediated Wurtzite Phase Formation in ZnS. *Cryst. Growth Des.*, 13:1369–1376, 2013.

- [14] Q. Fu, J. Lu, N. Lin, and S. Zheng. The Structures of Hydrazine Crystal and its Antibacterial Activities. *Rom. Biotechnol. Lett.*, 17:7557–7563, 2012.
- [15] J. C. Heckel, A. L. Weisman, S. T. Schneebeli, M. L. Hall, L. J. Sherry, S. M. Stranahan, K. H. DuBay, R. A. Friesner, and K. A. Willets. Polarized Raman Spectroscopy of Oligothiophene Crystals To Determine Unit Cell Orientation. *J. Phys. Chem. A*, 116:6804, 2012.
- [16] E. Smith and G. Dent. *Modern Raman Spectroscopy - A Practical Approach*. John Wiley & Sons Ltd, 2005.
- [17] M. Fleischmann, P. J. Hendra, and A. J. McQuillan. Raman Spectra of Pyridine Adsorbed at a Silver Electrode. *Chem. Phys. Lett.*, 26:163–166, 1974.
- [18] A. Hartschuh, E. J. Sanchez, S. Xie, and L. Novotny. High-Resolution Near-Field Raman Microscopy of Single-Walled Carbon Nanotubes. *Phys. Rev. Lett.*, 90:095503, 2003.
- [19] Cançado, A. Jorio, A. Ismach, E. Joselevich, A. Hartschuh, and L. Novotny. Mechanism of Near-Field Raman Enhancement in One-Dimensional Systems. *Phys. Rev. Lett.*, 103:186101, 2009.
- [20] L. G. Cançado, A. Hartschuh, and L. Novotny. Tip-Enhanced Raman Spectroscopy of Carbon Nanotubes. *J. Raman Spectrosc.*, 40:1420–1426, 2009.
- [21] N. Mauser and A. Hartschuh. Tip-Enhanced Near-Field Optical Microscopy. *Chem. Soc. Rev.*, 43:1248–1262, 2014.
- [22] M. A. Lieb, J. M. Zavislan, and L. Novotny. Single-Molecule Orientations Determined by Direct Emission Pattern Imaging. *J. Opt. Soc. Am. B*, 21:1210–1215, 2004.
- [23] M. Böhmler, N. Hartmann, C. Georgi, F. Hennrich, A. Green, M. Hersam, and A. Hartschuh. Enhancing and Redirecting Carbon Nanotube Photoluminescence by an Optical Antenna. *Opt. Express*, 18:16443–16451, 2010.
- [24] N. Hartmann, G. Piredda, J. Berthelot, G. Colas des Francs, A. Hartschuh, and A. Bouhelier. Launching Propagating Surface Plasmon Polaritons by a Single Carbon Nanotube Dipolar Emitter. *Nano Lett.*, 12:177–181, 2012.
- [25] F. Xia, T. Müller, R. Golizadeh-Mojarad, M. Freitag, Y.-M. Lin, J. Tsang, V. Perebeinos, and P. Avouris. Photocurrent Imaging and Efficient Photon Detection in a Graphene Transistor. *Nano Lett.*, 9:1039–1044, 2009.
- [26] Q. Cao, S.-H. Hur, Z.-T. Zhu, . Sun, C. Wang, M. A. Meitl, M. Shim, and J. A. Rogers. Highly Bendable, Transparent Thin-Film Transistors That Use Carbon-Nanotube-Based Conductors and Semiconductors with Elastomeric Dielectrics. *Adv. Mater.*, 18:304–309, 2006.

- [27] M. Pumera. Electrochemistry of Graphene: New Horizons for Sensing and Energy Storage. *Chem. Rec.*, 9:211–223, 2009.
- [28] E. S. Snow, F. K. Perkins, E. J. Houser, S. C. Badescu, and T. L. Reinecke. Chemical Detection with a Single-Walled Carbon Nanotube Capacitor. *Science*, 307:1942–1945, 2005.
- [29] M. Liang and L. Zhi. Graphene-Based Electrode Materials for Rechargeable Lithium Batteries. *J. Mat. Chem.*, 19:5871–5878, 2009.
- [30] L. Dai, D. W. Chang, J.-B. Baek, and W. Lu. Carbon Nanomaterials for Advanced Energy Conversion and Storage. *Small*, 8:1130–1166, 2012.
- [31] D. Yoon, H. Moon, Y.-W. Son, G. Samsonidze, B. H. Park, J. B. Kim, Y. Lee, and H. Cheong. Strong Polarization Dependence of Double-Resonant Raman Intensities in Graphene. *Nano Lett.*, 8:4270–4274, 2008.
- [32] K. S. Novoselov, A. K. Geim, S. V. Morozov, D. Jiang, Y. Zhang, S. V. Dubonos, I. V. Grigorieva, and A. A. Firsov. Electric Field Effect in Atomically Thin Carbon Films. *Science*, 306:666–669, 2004.
- [33] G. Tsoukleri, J. Parthenios, K. Papagelis, R. Jalil, A. C. Ferrari, A. K. Geim, K. S. Novoselov, and C. Galiotis. Subjecting a Graphene Monolayer to Tension and Compression. *Small*, 5:2397 – 2402, 2009.
- [34] A. K. Geim and K. S. Novoselov. The Rise of Graphene. *Nat. Mater.*, 6:183–191, 2007.
- [35] A. H. Castro Neto, F. Guinea, N. M. R. Peres, K. S. Novoselov, and A. K. Geim. The Electronic Properties of Graphene. *Rev. Mod. Phys.*, 81:109 – 162, 2009.
- [36] K. F. Mak, L. Ju, F. Wang, and T. F. Heinz. Optical Spectroscopy of Graphene: From the Far Infrared to the Ultraviolet. *Solid State Communications*, 152:1341 – 1349, 2012.
- [37] K. S. Kim, Y. Zhao, H. Jang, S. Y. Lee, and J. M. Kim and. Large Scale Pattern Growth of Graphene Films for Stretchable Transparent Electrodes. *Nature*, 457:706–710, 2009.
- [38] X. Li, L. Colombo, and R. S. Ruoff. Synthesis of Graphene Films on Copper Foils by Chemical Vapor Deposition. *Adv. Mater.*, 2016.
- [39] A. C. Ferrari, F. Bonaccorso, V. Fal’ko, K. S. Novoselov, S. Roche, P. Bøggild, S. Borini, F. H. Koppens, V. Palermo, and N. Pugno. Science and Technology Roadmap for Graphene, Related Two-Dimensional Crystals, and Hybrid Systems. *Nanoscale*, 7:4598–4810, 2015.

- [40] F. Bonaccorso, Z. Sun, T. Hasan, and A. C. Ferrari. Graphene Photonics and Optoelectronics. *Nat. Photonics*, 4:611–622, 2010.
- [41] N. M. Gabor, J. C. W. Song, Q. Ma, N. L. Nair, T. Taychatanapat, K. Watanabe, T. Taniguchi, L. S. Levitov, and P. Jarillo-Herrero. Hot Carrier Assisted Intrinsic Photoresponse in Graphene. *Science*, 334:648 – 652, 2011.
- [42] J. Park, Y.H. Ahn, and C. Ruiz-Vargas. Imaging of Photocurrent Generation and Collection in Single-Layer Graphene. *Nano Lett*, 9:1742–1746, 2009.
- [43] X. Xu, N. M. Gabor, J. S. Alden, A. M. van der Zande, and P. L. McEuen. Photo-Thermoelectric Effect at a Graphene Interface Junction. *Nano Lett.*, 10:562–566, 2009.
- [44] F. Schwierz. Graphene Transistors. *Nat. Nanotechnol.*, 5:487–496, 2010.
- [45] T. Gokus. *Time-Resolved Photoluminescence and Elastic White Light Scattering Studies of Individual Carbon Nanotubes and Optical Characterization of Oxygen Plasma Treated Graphene*. Ludwig-Maximilians-Universitat M'unchen, 2011. PhD thesis.
- [46] D. R. Cooper, B. D'Anjou, N. Ghattamaneni, B. Harack, M. Hilke, A. Horth, N. Majilis, M. Massicotte, L. Vandsburger, E. Whiteway, and V. Yu. Experimental Review of Graphene. *ISRN Condensed Matter Physics*, 2012:1–56, 2012.
- [47] S. Reich, C. Thomsen, and J. Maultzsch. *Carbon Nanotubes: Basic Concepts and Physical Properties*. Wiley-VCH Verlag, Weinheim, 2004.
- [48] P. R. Wallace. The Band Theory of Graphite. *Phys. Rev.*, 71:622–634, 1947.
- [49] J. C. Slonczewski and P. R. Weiss. Band Structure of Graphite. *Phys. Rev.*, 109:272–279, 1958.
- [50] Y. B. Zhang, Y. W. Tan, H. L. Stormer, and P. Kim. Experimental Observation of the Quantum Hall Effect and Berry's Phase in Graphene. *Nature*, 438:201–204, 2005).
- [51] K. S. Novoselov, A. K. Geim, S. V. Morozov, D. Jiang, and I. V. Grigorieva S. V. Dubonos A. A. Firsov M. I. Katsnelson. Two-Dimensional Gas of Massless Dirac Fermions in Graphene. *Nature*, 438:197–200, 2005.
- [52] P.R. Wallace. The Band Theory of Graphite. *Phys. Rev.*, 71:622, 1947.
- [53] A. C. Ferrari and D. M. Basko. Raman Spectroscopy as a Versatile Tool for Studying the Properties of Graphene. *Nat. Nanotechnol.*, 8:235–246, 2013.
- [54] R. Beams, L. G. Cançado, and L. Novotny. Raman Characterization of Defects and Dopants in Graphene. *J. Phys. Condens. Matter*, 27:083002, 2015.

- [55] A. C. Ferrari and J. Robertson. Resonant Raman Spectroscopy of Disordered, Amorphous, and Diamondlike Carbon. *Phys. Rev. B*, 64:075414, 2001.
- [56] A. C. Ferrari and J. Robertson. Interpretation of Raman Spectra of Disordered and Amorphous Carbon. *Phys. Rev. B*, 61:14095–14107, 1999.
- [57] A. C. Ferrari, J. C. Meyer, V. Scardaci, C. Casiraghi, M. Lazzeri, F. Mauri, S. Piscanec, D. Jiang, K. S. Novoselov, S. Roth, and A. K. Geim. Raman Spectrum of Graphene and Graphene Layers. *Phys. Rev. Lett.*, 97:187401, 2006.
- [58] M. S. Dresselhaus, G. Dresselhaus, and M. Hofmann. Raman Spectroscopy as a Probe of Graphene and Carbon Nanotubes. *Philos. Trans. R. Soc. London*, 366:231–236, 2008.
- [59] Z. H. Ni, T. Yu, Y. H. Lu, Y. Y. Wang, Y. P. Feng, and Z. X. Shen. Uniaxial Strain on Graphene: Raman Spectroscopy Study and Band-Gap Opening. *ACS Nano*, 2:2301–2305, 2008.
- [60] T. M. G. Mohiuddin, A. Lombardo, R. R. Nair, A. Bonetti, G. Savini, R. Jalil, N. Bonini, D. M. Basko, C. Galiotis, N. Marzari, K. S. Novoselov, A. K. Geim, and A. C. Ferrari. Uniaxial Strain in Graphene by Raman Spectroscopy: G Peak Splitting, Grüneisen Parameters, and Sample Orientation. *Phys. Rev. B*, 79:205433, 2009.
- [61] O. Frank, M. Mohr, J. Maultzsch, C. Thomsen, I. Riaz, R. Jalil, K. S. Novoselov, G. Tsoukleri, J. Parthenios, K. Papagelis, L. Kavan, and C. Galiotis. Raman 2D-Band Splitting in Graphene: Theory and Experiment. *ACS Nano*, 5:2231–2239, 2011.
- [62] T. Yu, Z. Ni, C. Du, Y. You, Y. Wang, and Z. J. Shen. Raman Mapping Investigation of Graphene on Transparent Flexible Substrate: The Strain Effect. *Phys. Chem. C*, 112:12602–12605, 2008.
- [63] Z. H. Ni, T. Yu, Z. Q. Luo, Y. Y. Wang, L. Liu, C. P. Wong, J. Miao, W. Huang, and Z. X. Shen. Probing Charged Impurities in Suspended Graphene Using Raman Spectroscopy. *ACS Nano*, 3:569–574, 2009.
- [64] A. Das, S. Pisana, B. Chakraborty, S. Piscanec, S. K. Saha, U. V. Waghmare, K. S. Novoselov, H. R. Krishnamurthy, A. K. Geim, A. C. Ferrari, and A. K. Sood. Monitoring Dopants by Raman Scattering in an Electrochemically Top-Gated Graphene Transistor. *Nat. Nanotechnol.*, 3:210–215, 2008.
- [65] Y. Hao, Y. Wang, L. Wang, Z. Ni, Z. Wand, R. Wang, C. K. Koo, Z. Shen, and J. T. L. Thong. Probing Layer Number and Stacking Order of Few-Layer Graphene by Raman Spectroscopy. *Small*, 6:195–200, 2010.
- [66] V. Carozo, C. M. Almeida, E. H. M. Ferreira, L. G. Canço, C. A. Achete, and A. Jorio. Raman Signature of Graphene Superlattices. *Nano Lett.*, 6:4527–4534, 2011.

- [67] M. Dresselhaus, G. Dresselhaus, R. Saito, and A. Jorio. Raman Spectroscopy of Carbon Nanotubes. *Phys. Rep.*, 409:47–99, 2005.
- [68] L. M. Malard, M. A. Pimenta, G. Dresselhaus, and M. S. Dresselhaus. Raman Spectroscopy in Graphene. *Phys. Rep.*, 473:51–87, 2009.
- [69] A. Jorio, M. S. Dresselhaus, R. Saito, and G. Dresselhaus. *Raman Spectroscopy in Graphene Related Systems*. Wiley, Weinheim, 2011.
- [70] F. Tuinstra and J. L. König. Raman Spectrum of Graphite. *J. Chem. Phys.*, 53:1126–1130, 1970.
- [71] D. Yoon, Y.-W. Son, and H. Cheong. Strain-Dependent Splitting of the Double-Resonance Raman Scattering Band in Graphene. *Phys. Rev. Lett.*, 106:155502, 2011.
- [72] A. Eckmann, A. Felten, A. Mishchenko, L. Britnell, R. Krupke, K. S. Novoselov, and C. Casiraghi. Probing the Nature of Defects in Graphene by Raman Spectroscopy. *Nano Lett.*, 12:3925–3930, 2012.
- [73] M. M. Lucchese, F. Stavale, E. H. Martins Ferreira, C. Vilani, M. V. O. Moutinho, R. B. Capaz, C. A. Achete, and A. Jorio. Quantifying Ion-Induced Defects and Raman Relaxation Length in Graphene. *Carbon*, 48:1592–1597, 2010.
- [74] L. G. Cançado, A. Jorio, E. H. Martins Ferreira, F. Stavale, C. A. Achete, R. B. Capaz, M. V. O. Moutinho, A. Lombardo, T. S. Kulmala, and A. C. Ferrari. Quantifying Defects in Graphene via Raman Spectroscopy at Different Excitation Energies. *Nano Lett.*, 11:3190–3196, 2011.
- [75] P. Lespade, A. March, M. Couzi, and F. Cruege. Characterisation de matériaux carbonés par microspectrométrie Raman. *Carbon*, 22:375–85, 1984.
- [76] L. G. Cançado, M. A. Pimenta, B. R. A. Neves, M. S. S. Dantas, and A. Jorio. Influence of the Atomic Structure on the Raman Spectra of Graphite Edges. *Phys. Rev. Lett.*, 93:247401, 2004.
- [77] C. Casiraghi, A. Hartschuh, H. Qian, S. Piscanec, C. Georgi, A. Fasoli, K. S. Novoselov, D. M. Basko, and A. C. Ferrari. Raman Spectroscopy of Graphene Edges. *Nano Lett.*, 9:1433–1441, 2009.
- [78] R. Beams, L. G. Cançado, and L. Novotny. Low Temperature Raman Study of the Electron Coherence Length Near Graphene Edges. *Nano Lett.*, 11:1177–1181, 2011.
- [79] S. Heydrich. *Raman Spectroscopy of Nanopatterned Graphene*. Universität Regensburg, 2014. PhD thesis.

- [80] A. Grüneis, R. Saito, G. Samsonidze, T. Kimura, M. A. Pimenta, A. Jorio, A. G. Souza Filho, Fresselhaus G., and Dresselhaus M. S. Inhomogeneous Optical Absorption around the K Point in Graphite and Carbon Nanotubes. *Phys. Rev. B*, 67:165402, 2003.
- [81] B. Partoens and F. M. Peeters. From Graphene to Graphite: Electronic Structure around the K Point. *Phys. Rev. B*, 74:075404, 2006.
- [82] L. G. Cançado, M. A. Pimenta, B. R. A. Neves, , G. Medeiros-Ribeiros, T. Enoki, Y. Kobayashi, K. Takai, K. Fukui, M. S. Dresselhaus, R. Saito, and A. Jorio. Anisotropy of the Raman Spectra of Nanographite Ribbons. *Phys. Rev. Lett.*, 93:047403, 2004.
- [83] G. Samsonidze. *Photophysics of Carbon Nanotubes*. Massachusetts Institute of Technology, 2007.
- [84] D. L. Mafra, G. Samsonidze, L. M. Malard, D. C. Elias, J. C. Brant, F. Plentz, E. S. Alves, and M. A. Pimenta. Determination of LA and TO Phonon Dispersion Relations of Graphene near the Dirac Point by Double-Resonance Raman Scattering. *Phys. Rev. B*, 76:233407, 2007.
- [85] P. Tan, C. Hu, J. Dong, W. Shen, and B. Zhang. Polarization Properties, High-Order Raman Spectra, and Frequency Asymmetry between Stokes and Anti-Stokes Scattering of Raman Modes in a Graphite Whisker. *Phys. Rev. B*, 64:214301, 2001.
- [86] R. Loudon. The Raman Effect in Crystals. *Adv. Phys.*, 13:423–482, 1964.
- [87] D. M. Basko. Effect of Inelastic Collisions on Multiphonon Raman Scattering in Graphene. *Phys. Rev. B*, 76:081405(R), 2007.
- [88] J. Maultzsch, S. Reich, and C. Thomsen. Double-Resonant Raman Scattering in Graphite: Interference Effects, Selection Rules, and Phonon Dispersion. *Phys. Rev. B*, 70:155403, 2004.
- [89] C. Thomsen and S. Reich. Double Resonant Raman Scattering in Graphite. *Phys. Rev. Lett.*, 85:5214–5217, 2000.
- [90] J. Jiang, R. Saito, G. Samsonidze, S. G. Chou, A. Jorio, G. Dresselhaus, and M. S. Dresselhaus. Electron-Phonon Matrix Elements in Single-Wall Carbon Nanotubes. *Phys. Rev. B*, 72:235408, 2005.
- [91] P. Venezuela, M. Lazzeri, and F. Mauri. Theory of Double-Resonant Raman Spectra in Graphene: Intensity and Line Shape of Defect-Induced and Two-Phonon Bands. *Phys. Rev. B: Condens. Matter Mater. Phys.*, 84:035433, 2011.
- [92] S. Sahoo, R. Palai, and R. S. Katiyar. Polarized Raman Scattering in Monolayer, Bilayer, and Suspended Bilayer Graphene. *J. Appl. Phys.*, 110:044320, 2011.

- [93] L. V. Radushkevich and V. M. Lukyanovich. O strukture ugleroda, obrazujuce gosja pri termiceskom razlozenii okisi ugleroda na zelesnom kontakte. *Zurn. Fisic. Chim.*, 26:88–95, 1952.
- [94] S. Iijima and T. Ichihashi. Single-Shell Carbon Nanotubes of 1-nm Diameter. *Nature*, 363:603–605, 1993.
- [95] D. S. Bethune, C. H. Kiang, M. S. De Vries, G. Gorman, R. Savoy, J. Vazquez, and R. Beyers. Cobalt Catalysed Growth of Carbon Nanotubes with Single-Atomic-Layer Walls. *Nature*, 363:605–607, 1993.
- [96] L. Yang, S. Wang, Q. Zheng, Z. Zhang, and L.-M. Peng. Carbon Nanotube Photoelectronic and Photovoltaic Devices and their Applications in Infrared Detection. *Small*, 9:1225–1236, 2013.
- [97] M. H. P. Pfeiffer, N. Stürzl, C. W. Marquardt, M. Engel, S. Dehm, F. Henrich, M. M. Kappes, U. Lemmer, and R. Krupke. Electroluminescence from Chirality-Sorted (9,7)-Semiconducting Carbon Nanotube Devices. *Opt. Express*, 19:1184–1189, 2011.
- [98] N. F. Hartmann. *Coupling of Emitters to Surface Plasmons Investigated by Back Focal Plane Microscopy*. Ludwig-Maximilians-Universität München, 2014. PhD thesis.
- [99] S. Maruyama. Nanotube Coordinate Generator with a Viewer for Windows. <http://www.photon.t.u-tokyo.ac.jp/maruyama/wrapping3/wrapping.html>.
- [100] G. Dukovic, M. Balaz, P. Doak, N. D. Berova, M. Zheng, R. S. McLean, and L. E. Brus. Racemic Single-Walled Carbon Nanotubes Exhibit Circular Dichroism when Wrapped with DNA. *J. Am. Chem. Soc.*, 128:9004–9005, 2006.
- [101] K. Akazaki, F. Toshimitsu, H. Ozawa, T. Fujigaya, and N. Nakashima. Recognition and One-Pot Extraction of Right- and Left-Handed Semiconducting Single-Walled Carbon Nanotube Enantiomers using Fluorene-Binaphthol Chiral Copolymers. *J. Am. Chem. Soc.*, 134:12700–12707, 2012.
- [102] Y. Miyauchi, M. Oba, and S. Maruyama. Cross-Polarized Optical Absorption of Single-Walled Nanotubes by Polarized Photoluminescence Excitation Spectroscopy. *Phys. Rev. B*, 74:205440, 2006.
- [103] R. Saito, G. Dresselhaus, and M. S. Dresselhaus. *Physical Properties of Carbon Nanotubes*. Imperial College Press, 1998.
- [104] J. Lefebvre and P. Finnie. Polarized Photoluminescence Excitation Spectroscopy of Single-Walled Carbon Nanotubes. *Phys. Rev. Lett.*, 98:167406, 2007.

- [105] R. Saito, A. Jorio, A. G. Souza Filho, G. Dresselhaus, M. S. Dresselhaus, and M. A. Pimenta. Probing Phonon Dispersion Relations of Graphite by double Resonance Raman Scattering. *Phys. Rev. Lett.*, 88:027401, 2002.
- [106] A. Jorio, M. S. Dresselhaus, and G. Dresselhaus. *Carbon Nanotubes*. Springer, Berlin / Heidelberg, 2008.
- [107] A. Jorio, A. G. Souza Filho, G. Dresselhaus, M. S. Dresselhaus, A. K. Swan, M. S. Ünlü, B. B. Goldberg, M. A. Pimenta, J. H. Hafner, C. M. Lieber, and R. Saito. G-Band Resonant Raman Study of 62 Isolated Single-Walled Carbon Nanotubes. *Phys. Rev. B*, 65:155412, 2002.
- [108] J. Maultzsch, S. Reich, C. Thomsen, S. Webster, R. Czerw, D. L. Carroll, S. M. C. Vieira, P. R. Birkett, and C. A. Rego. Raman Characterization of Boron-Doped Multiwalled Carbon Nanotubes. *Appl. Phys. Lett.*, 81:2647–2649, 2002.
- [109] A. Jorio, R. Saito, J. H. Hafner, C. M. Lieber, M. Hunter, T. McClure, G. Dresselhaus, and M. S. Dresselhaus. Structural (n,m) Determination of Isolated Single-Walled Carbon Nanotubes by Resonant Raman Scattering. *Phys. Rev. Lett.*, 86:1118–1121, 2001.
- [110] L. G. Cançado, K. Takai, T. Enoki, M. Endo, Y. A. Kim, H. Mizusaki, A. Jorio, L. N. Coelho, R. Magalhaes-Paniago, and M. A. Pimenta. General Equation for the Determination of the Crystallite Size L_a of Nanographite by Raman Spectroscopy. *Appl. Phys. Lett.*, 88:163106, 2006.
- [111] R. P. Vidano, D. B. Fischbach, L. J. Willis, and T. M. Loehr. Observation of Raman Band Shifting with Excitation Wavelength for Carbons and Graphites. *Solid State Commun.*, 39:341–344, 1981.
- [112] J. H. Hafner, M. J. Bronikowski, B. R. Azamian, P. Nikolaev, A. G. Rinzler, F. T. Colbert, K. A. Smith, and R. E. Smalley. Catalytic Growth of Single-Wall Carbon Nanotubes from Metal Particles. *Chem. Phys. Lett.*, 296:195–202, 1998.
- [113] B. Kitiyanan, W. E. Alvarez, J. H. Harwell, and D. E. Resasco. Controlled Production of Single-Wall Carbon Nanotubes by Catalytic Decomposition of CO on Bimetallic Co-Mo Catalysts. *Chem. Phys. Lett.*, 317:497–503, 2000.
- [114] L. Novotny. Effective Wavelength Scaling for Optical Antennas. *Phys. Rev. Lett.*, 98:266802, 2007.
- [115] M. Böhmeler. *Tip-Enhanced Near-Field Optical Microscopy on the quasi 1D Semiconductors Carbon Nanotubes and CdSe Nanowires*. Ludwig-Maximilians-Universität München, 2012. PhD thesis.

- [116] K.-S. Lee and M. A. El-Sayed. Gold and Silver Nanoparticles in Sensing and Imaging: Sensitivity of Plasmon Response to Size, Shape, and Metal Composition. *J. Phys. Chem. B*, 110:19220–19225, 2006.
- [117] L. Bujak, M. Olejnik, T. H. P. Brotsudarmo, M. K. Schmidt, N. Czechowski, D. Piatkowski, J. Aizpuru, R. J. Cogdell, W. Heiss, and S. Mackowski. Polarization Control of Metal-Enhanced Fluorescence in Hybrid Assemblies of Photosynthetic Complexes and Gold Nanorods. *Phys. Chem. Chem. Phys.*, 16:9015–9022, 2014.
- [118] T. K. Sau and C. J. Murphy. Seeded High Yield Synthesis of Short Au Nanorods in Aqueous Solution. *Langmuir*, 20:6414–6420, 2004.
- [119] F. Bonaccorso, A. Lombardo, T. Hasan, Z. Sun, L. Colombo, and A. C. Ferrari. Production and Processing of Graphene and 2D Crystals. *Mater. Today*, 15:564–589, 2012.
- [120] M. Minsky. Memoir on Inventing the Confocal Scanning Microscope. *Scanning*, 10:128–138, 1988.
- [121] A. G. Curto, T. H. Taminiau, G. Volpe, M. P. Kreuzer, R. Quidant, and N. F. van Hulst. Multipolar Radiation of Quantum Emitters with Nanowire Optical Antennas. *Nat. Commun.*, 4:1750–1757, 2013.
- [122] B. Hecht, H. Bielefeldt, L. Novotny, Y. Inouye, and D. W. Pohl. Local Excitation Scattering, and Interference of Surface Plasmons. *Phys. Rev. Lett.*, 77:1889–1892, 1996.
- [123] A. Volkmer, J.-X. Cheng, and X. S. Xie. Vibrational Imaging with High Sensitivity via Epidetected Coherent Anti-Stokes Raman Scattering Microscopy. *Phys. Rev. Lett.*, 87:023901, 2001.
- [124] T. H. Taminiau, F. D. Stefani, and N. F. van Hulst. Optical Antennas Direct Single-Molecule Emission. *Nat. Photonics*, 2:234–237, 2008.
- [125] S. Kühn, G. Mori, M. Agio, and V. Sandoghdar. Modification of Single Molecule Fluorescence Close to a Nanostructure: Radiation Pattern, Spontaneous Emission and Quenching. *Mol. Phys.*, 106:893–941, 2008.
- [126] J. A. Kurvits, M. Jiang, and R. Zia. Comparative Analysis of Imaging Configurations and Objectives for Fourier Microscopy. *J. Opt. Soc. Am. A*, 32:2082–2092, 2015.
- [127] L. Novotny. Allowed and Forbidden Light in Near-Field Optics. I. A Single Dipole. *J. Opt. Soc. Am. A*, 14:91–104, 1997.
- [128] H. Weyl. Ausbreitung elektromagnetischer Wellen in der drahtlosen Telegraphie. *Ann. Phys. (Leipzig)*, 60:481–500, 1919.

- [129] M. Born and E. Wolf. *Principles of Optics: Electromagnetic Theory of Propagation, Interference and Diffraction of Light*. Cambridge University Press, 2011. 7th ed.
- [130] A. Sommerfeld. über die Ausbreitung der Wellen in der drahtlosen Telegraphie. *Ann. Phys. (Leipzig)*, 28:665–736, 1909.
- [131] H. v. Hörschelmann. über die Wirkungsweise des geknickten Marconischen Senders in der drahtlosen Telegraphie. *Telegr. Teleph.*, 5:188–211, 1911.
- [132] A. Sommerfeld. über die Ausbreitung der Wellen in der drahtlosen Telegraphie. *Ann. Phys. (Leipzig)*, 81:1135–1153, 1926.
- [133] Ch. Fattinger and W. Lukosz. Optical-Environment-Dependent Lifetimes and Radiation Patterns of Luminescent Centers in Very Thin Films. *J. Lumin.*, 31/32:933–935, 1984.
- [134] L. Novotny and B. Hecht. *Principles of Nano-Optics*. Cambridge University Press, Cambridge, 2008.
- [135] E. Hecht. *Optics*. Addison Wesley, 2002. 4th ed.
- [136] S. Wu, G. Han, D. J. Milliron, S. Aloni, V. Altoe, D. V. Talapin, B. E. Cohen, and P. J. Shuck. Non-Blinking and Photostable Upconverted Luminescence from Single Lanthanide-Doped Nanocrystals. *Proc. Natl. Acad. Sci. U.S.A.*, 106:10917–10921, 2009.
- [137] L. Dai, I. Gregor, E. von der Hocht, T. Ruckstuhl, and J. Enderlein. Measuring Large Numerical Apertures by Imaging the Angular Distribution of Radiation of Fluorescing Molecules. *Opt. Express*, 13:9409–9414, 2005.
- [138] W. Lauterborn, T. Kurz, and M. Wiesenfeldt. *Kohärente Optik - Grundlagen für Physiker und Ingenieure*. Springer, 1993. 1st ed.
- [139] A. Drezet, A. Hohenau, D. Koller, A. Stepanov, H. Ditlbacher, B. Steinberger, F. R. Aussenegg, A. Leitner, and J. R. Krenn. Leakage Radiation Microscopy of Surface Plasmon Polaritons. *Mater. Sci. Eng. B*, 149:220–229, 2008.
- [140] K. Yamaguchi. Immersion Microscope Objective Lens. *US Patent*, 6,519,092:B2, 2003.
- [141] A. Mohtashami, C. I. Osorio, and A. F. Koenderink. Angle-Resolved Polarimetry Measurements of Antenna-Mediated Fluorescence. *Phys. Rev. Applied*, 4:054014, 2015.
- [142] A. C. Ferrari and J. Robertson. Raman Spectroscopy of Amorphous, Nanostructured, Diamond-Like Carbon, and Nanodiamond. *Phil. Trans. R. Soc. A*, 362:2477–2512, 2004.

- [143] A. C. Ferrari. Raman Spectroscopy of Graphene and Graphite: Disorder, Electron-Phonon Coupling, Doping and Nonadiabatic Effects. *Solid State Commun.*, 143:47–57, 2007.
- [144] W. Su and D. Roy. Visualizing Graphene Edges Using Tip-Enhanced Raman Spectroscopy. *J. Vac. Sci. Technol. B*, 31:041808, 2013.
- [145] N. Hartmann, G. Piredda, J. Berthelot, G. Colas des Francs, A. Bouhelier, and A. Hartschuh. Launching Propagating Surface Plasmon Polaritons by a Single Carbon Nanotube Dipolar Emitter. *Nano Lett.*, 12:177–181, 2011.
- [146] V. N. Popov and P. Lambin. Theoretical Polarization Dependence of the Two-Phonon Double-Resonant Raman Spectra of Graphene. *Eur. Phys. J. B*, 85:418–438, 2012.
- [147] R. V. Maximiano, R. Beams, L. Novotny, A. Jorio, and L. G. Cançado. Mechanism of Near-Field Raman Enhancement in Two-Dimensional Systems. *Phys. Rev. B*, 85:235434, 2012.
- [148] L. G. Cançado, R. Beams, A. Jorio, and L. Novotny. Theory of Spatial Coherence in Near-Field Raman Scattering. *Phys. Rev. X*, 4:031054, 2014.
- [149] T. Wilson and R. Juskaitis. The Axial Response of Confocal Microscopes with High Numerical Aperture Objective Lenses. *Bioimaging*, 3:35–38, 1995.
- [150] W. T. Tang, E. Chung, Y. H. Kim, P. T. So, and C. J. R. Sheppard. Investigation of the Point Spread Function of Surface Plasmon-Coupled Emission Microscopy. *Opt. Express*, 15:4634–4646, 2007.
- [151] L. G. Cançado and L. Novotny. Observing the Angular Distribution of Raman Scattered Fields. *ACS Nano*, 10:1722–1723, 2016.
- [152] D. Khang, J. Xiao, C. Kocabas, S. MacLaren, T. Banks, H. Jiang, Y. Huang, and J. Rogers. Molecular Scale Buckling Mechanics in Individual Aligned Single-Wall Carbon Nanotubes on Elastomeric Substrates. *Nano Lett.*, 8:124, 2008.
- [153] X. Zhou, J. Park, S. Huang, J. Liu, and P. McEuen. Band Structure, Phonon Scattering, and the Performance Limit of Single-Walled Carbon Nanotube Transistors. *Phys. Rev. Lett.*, 95:146805, 2005.
- [154] Z. Yao, C. Kane, and C. Dekker. High-Field Electrical Transport in Single-Wall Carbon Nanotubes. *Phys. Rev. Lett.*, 84:2941, 2000.
- [155] S. Berber, Y. K. Kwon, and D. Tomanek. Unusually High Thermal Conductivity of Carbon Nanotubes. *Phys. Rev. Lett.*, 84:4613–4616, 2000.
- [156] M. Kaempgen, G. Duesberg, and S. Roth. Transparent Carbon Nanotube Coatings. *Appl. Surf. Sci.*, 252:425–429, 2005.

- [157] J. Du, S. Pei, L. Ma, and H.-M. Cheng. Carbon Nanotube- and Graphene-Based Transparent Conductive Films for Optoelectronic Devices. *Adv. Mater.*, 26:1958–1991, 2014.
- [158] D. S. Hecht, L. Hu, and G. Irvin. Emerging Transparent Electrodes Based on Thin Films of Carbon Nanotubes, Graphene, and Metallic Nanostructures. *Adv. Mater.*, 23:1482–1513, 2011.
- [159] E. Artukovic, M. Kaempgen, D. S. Hecht, S. Roth, and G. Grüner. Transparent and Flexible Carbon Nanotube Transistors. *Nano Lett.*, 5:757–760, 2005.
- [160] J. Zhang, C. Wang, and C. Zhou. Rigid/Flexible Transparent Electronics Based on Separated Carbon Nanotube Thin-Film Transistors and Their Application in Display Electronics. *ACS Nano*, 6:7412–7419, 2012.
- [161] J. Liang, L. Li, D. Chen, T. Hajagos, Z. Ren, S.-Y. Chou, W. Hu, and Q. Pei. Intrinsically Stretchable and Transparent Thin-Film Transistors Based on Printable Silver Nanowires, Carbon Nanotubes and an Elastomeric Dielectric. *Nature Comm.*, 6:7647, 2015.
- [162] L. Yang, R. Zhang, D. Staiculescu, C. Wong, and M. Tentzeris. A Novel Conformal RFID-Enabled Module Utilizing Inkjet-Printed Antennas and Carbon Nanotubes for Gas-Detection Applications. *Antennas and Wireless Propagation Letters, IEEE*, 8:653–656, 2009.
- [163] A. Vena, L. Sydanheimo, M. Tentzeris, and L. Ukkonen. A Novel Inkjet Printed Carbon Nanotube-Based Chipless RFID Sensor for Gas Detection. *European Microwave Conference (EuMC)*, pages 9–12, 2013.
- [164] D. Kim, H.-C. Lee, J. Y. Woo, and C.-S. Han. Thermal Behavior of Transparent Film Heaters made of Single-Walled Carbon Nanotubes. *J. Phys. Chem. C*, 114:5817–5821, 2010.
- [165] M. S. Arnold, S. I. Stupp, and M. C. Hersam. Enrichment of Single-Walled Carbon Nanotubes by Diameter in Density Gradients. *Nano Lett.*, 5:713–718, 2005.
- [166] M. S. Arnold, A. A. Green, J. F. Hulvat, S. I. Stupp, and M. C. Hersam. Sorting Carbon Nanotubes by Electronic Structure via Density Differentiation. *Nat. Nanotechnol.*, 1:60–65, 2006.
- [167] M. S. Arnold, J. Suntivich, S. I. Stupp, and M. C. Hersam. Hydrodynamic Characterization of Surfactant Encapsulated Carbon Nanotubes using an Analytical Ultracentrifuge. *ACS Nano*, 2:2291–2300, 2008.
- [168] H. Liu, D. Nishide, T. Tanaka, and H. Kataura. Large-Scale Single-Chirality Separation of Single-Wall Carbon Nanotubes by Simple Gel Chromatography. *Nat. Commun.*, 2:309–317, 2011.

- [169] H. Liu, T. Tanaka, Y. Urabe, and H. Kataura. High-Efficiency Single-Chirality Separation of Carbon Nanotubes Using Temperature-Controlled Gel Chromatography. *Nano Lett.*, 13:1996–2003, 2013.
- [170] T. Tanaka, Y. Urabe, T. Hirakawa, and H. Kataura. Simultaneous Chirality and Enantiomer Separation of Metallic Single-Wall Carbon Nanotubes by Gel Column Chromatography. *Anal. Chem.*, 87:9467–9472, 2015.
- [171] D. Simien, J. A. Fagan, W. Luo, J. F. Douglas, K. Migler, and J. Obrzut. Influence of Nanotube Length on the Optical and Conductivity Properties of Thin Single-Wall Carbon Nanotube Networks. *ACS Nano*, 2:1879–1884, 2008.
- [172] G. E. Pike and C. H. Seager. Percolation and Conductivity: A Computer Study. I. *Phys. Rev. B*, 10:1421–1434, 1974.
- [173] J. Li and S.-L. Zhang. Finite-Size Scaling in Stick Percolation. *Phys. Rev. E*, 80:040104, 2009.
- [174] F. Hennrich, R. Krupke, K. Arnold, J. A. R. Stütz, S. Lebedkin, T. Koch, T. Schimmel, and M. M. Kappes. The Mechanism of Cavitation-Induced Scission of Single-Walled Carbon Nanotubes. *J. Phys. Chem. B*, 111:1932–1937, 2007.
- [175] G. Pagani, M. J. Green, P. Poulin, and M. Pasquali. Competing Mechanisms and Scaling Laws for Carbon Nanotube Scission by Ultrasonication. *PNAS*, 109:11599–11604, 2012.
- [176] A. Lucas, C. Zakri, M. Maugey, M. Pasquali, P. van der Schoot, and P. Poulin. Kinetics of Nanotube and Microfiber Scission under Sonication. *J. Phys. Chem. C*, 113:20599–20605, 2009.
- [177] Y. Tan and D. E. Resasco. Dispersion of Single-Walled Carbon Nanotubes of Narrow Diameter Distribution. *J. Phys. Chem. B*, 109:14454–14460, 2005.
- [178] H. Yu, S. Hermann, S. E. Schulz, T. Gessner, Z. Dong, and W. J. Li. Optimizing Sonication Parameters for Dispersion of Single-Walled Carbon Nanotubes. *Chemical Physics*, 408:11 – 16, 2012.
- [179] D. A. Skoog, D. M. West, and F. J. Holler. *Analytical Chemistry: An Introduction*. Brooks/Cole, 7th edition, 1999.
- [180] D. A. Skoog, D. M. West, F. J. Holler, and S. R. Crouch. *Fundamentals of Analytical Chemistry*. Thomson - Brooks/Cole, 8th edition, 2003.
- [181] M. S. Strano, V. C. Moore, M. K. Miller, M. J. Allen, E. H. Haroz, C. Kittrell, R. H. Hauge, and R. E. Smalley. The Role of Surfactant Adsorption During Ultrasonication in the Dispersion of Single-Walled Carbon Nanotubes. *J. Nanosci. Nanotechnol.*, 3:81–86, 2003.

- [182] S. Lee, J. W. Peng, and C. H. Liu. Probing Plasma-Induced Defect Formation and Oxidation in Carbon Nanotubes by Raman Dispersion Spectroscopy. *Carbon*, 47:3488–97, 2009.
- [183] J. R. Simpson, J. A. Fagan, L. Becker, E. K. Hobbie, and A. R. Hight Walker. The Effect of Dispersant on Defects in Length-Separated Single-Wall Carbon Nanotubes Measured by Raman Spectroscopy. *Carbon*, 47:3238–41, 2009.
- [184] P. Delhaes, M. Couzi, M. Trinquedone, J. Dentzer, H. Hamidou, and C. Vix-Guterl. A Comparison Between Raman Spectroscopy and Surface Characterizations of Multiwall Carbon Nanotubes. *Carbon*, 44:3005–13, 2006.
- [185] Y. Kobayashi, D. Takagi and Y. Ueno, and Y. Homma. Characterization of Carbon Nanotubes Suspended between Nanostructures using Micro-Raman Spectroscopy. *Phys E*, 24:26–31, 2004.
- [186] W. Qian, T. Liu, F. Wei, and H. Yuan. Quantitative Raman Characterization of the Mixed Samples of the Single and Multi-Wall Carbon Nanotubes. *Carbon*, 41:1851–4, 2003.
- [187] H. M. Heise, R. Ruckuk, A. K. Ojha, A. Srivastava, V. Srivastava, and B. P. Asthana. Characterization of Carbonaceous Materials using Raman Spectroscopy: a Comparison of Carbon Nanotube Filters, Single and Multi-Walled Nanotubes, Graphitised Porous Carbon and Graphite. *J. Raman Spectrosc*, 40:0344–53, 2009.
- [188] T. Hertel, S. Himmelein, T. Ackermann, D. Stich, and J. Crochet. Diffusion Limited Photoluminescence Quantum Yields in 1-D Semiconductors: Single-Wall Carbon Nanotubes. *ACS Nano*, 4:7161–7168, 2010.
- [189] S. G. Chou, H. Son, J. Kong, A. Jorio, R. Saito, M. Zheng, G. Dresselhaus, and M. S. Dresselhaus. Length Characterization of DNA-Wrapped Carbon Nanotubes using Raman Spectroscopy. *Appl. Phys. Lett.*, 90,131109., 2007,.
- [190] S. Heeg, A. Oikonomou, R. Fernandez-Garcia, S. Maier, A. Vijayaraghavan, and S. Reich. Strained Graphene as a Local Probe for Plasmon-Enhanced Raman Scattering by Gold Nanostructures. *Phys. Status Solidi RRL*, 7:1067–1070, 2013.
- [191] S. Heeg, N. Clark, A. Oikonomou, A. Vijayaraghavan, and S. Reich. Plasmon-Enhanced Raman Scattering by Suspended Carbon Nanotubes. *Phys. Status Solidi RRL*, 8:785–789, 2014.
- [192] S. Heeg, A. Oikonomou, R. Fernandez-Garcia, C. Lehmann, S. Maier, A. Vijayaraghavan, and S. Reich. Plasmon-Enhanced Raman Scattering by Carbon Nanotubes Optically Coupled with Near-Field Cavities. *Nano Lett.*, 14:1762–1768, 2014.
- [193] M. Mandai. Immersion Microscope Objective Lens. *US Patent*, 7,046,451 B2, 2006.

-
- [194] K. Watanabe. Immersion-Type Microscope Objective Lens. *US Patent*, 5,798,869 A, 1998.
- [195] N. Furutake. Immersion Microscope Objective Lens System. *US Patent*, 5,982,559 A, 1999.
- [196] S. Kudo. Immersion Microscope Objective. *US Patent*, 5,978,147 A, 1999.
- [197] N. Furutake. Microscope Objective Lens. *US Patent*, 6,128,139, 2000.
- [198] Y. Okuyama. Liquid Immersion Type Objective Lens. *US Patent Application*, 2003/0043473A1, 2003.
- [199] K. Watanabe. Liquid Immersion Type Microscope Objective Lens. *US Patent*, 6,700,710 B2, 2004.
- [200] K. Yamaguchi. Immersion Microscope Objective Lens. *US Patent*, 7,262,922 B2, 2007.
- [201] M. Yoshida. Immersion Type Microscope Objective Lens. *US Patent*, 7,889,433 B2, 2011.
- [202] K. Yamaguchi. Immersion Microscope Objective Lens. *US Patent*, 8,199,408 B2, 2012.
- [203] author. Ueber die fortleitung electriccher wellen durch drähte. *Annalen der Physik und Chemie*, 273:395–408, 1889.
- [204] P. Bharadwaj, B. Deutsch, and L. Novotny. Optical Antennas. *Adv. Opt. Photonics*, 1:438–483, 2009.
- [205] S. Eustis and M. A. El-Sayed. Why gold nanoparticles are more precious than pretty gold: Noble metal surface plasmon resonance and its enhancement of the radiative and nonradiative properties of nanocrystals of different shapes. *Chem. Soc. Rev.*, 35:209–217, 2006.
- [206] J. Wessel. Surface-Enhanced Optical Microscopy. *J. Opt. Soc. Am. B*, 2:1538–1541, 1985.
- [207] L. Novotny. Effective Wavelength Scaling for Optical Antennas. *Phys. Rev. Lett.*, 98:266802, 2007.
- [208] P. Bharadwas, B. Deutsch, and L. Novotny. Optical Antennas. *Adv. Opt. Photonics*, 1:438–483, 2009.
- [209] C. F. Bohren and D. R. Huffman. *Absorption and Scattering of Light by Small Particles*. Wiley-VCH Verlag GmbH, Weinheim, 2007.

Acronyms

1D	one-dimensional
2D	two-dimensional
A	acoustic
AFM	atomic force microscopy
APD	avalanche photo diode
BFP	back focal plane
BL	Bertrand lens
BZ	Brillouin zone
CB	conduction band
CCD	charged coupled device
CoMoCat	cobalt-molybdenum catalyst
CTAB	cetyltrimethylammonium bromide
CVD	chemical vapor deposition
FIT	full three-dimensional finite-integration technique
FWHM	full width half maximum
HiPCO	high pressure carbon monoxide
i	in-plane

IRinfrared
Llongitudinal
LCR liquid crystal retarder
LED light emitting diode
NAnumerical aperture
NIR near infrared
o out-of-plane
O optical
Obj. objective
ODoptical density
p parallel (polarization)
PMMA Poly(methyl methacrylate)
RBM radial breathing mode
s senkrecht (polarization)
SDBS sodium dodecyl benzenesulfonate
SDSsodium dodecyl sulfate
SERS surface-enhanced Raman scattering
SLGsingle-layer graphene
SPM scanning probe microscope
STM scanning tunneling microscopy
SWCNT single-walled carbon nanotube

T	transverse
TEM	transmission electron microscopy
TERS	tip-enhanced Raman scattering
TL	tube lens
VB	valence band

List of Figures

1.1	a) Real space unit cell of graphene with real space lattice vectors a_1 and a_2 , b) Full electronic dispersion of the π -bands in the graphene Brillouin zone with the high symmetry points \mathbf{K} , \mathbf{K}' , \mathbf{M} and Γ , c) Reciprocal space lattice with the high-symmetry points Γ , \mathbf{M} and \mathbf{K} (\mathbf{K}').	6
1.2	Raman Scattering process. a) Stokes process. b) Anti-Stokes process.	7
1.3	Energy level diagrams of Raman scattering processes. a) non-resonant Raman scattering, b) Raman Scattering with incident resonance, c) Raman scattering with scattered resonance, d) Double Resonant Raman scattering.	9
1.4	a) Phonon dispersion relation of graphene along the high symmetry lines of Γ - \mathbf{K} - \mathbf{M} - Γ of the graphene BZ, b) Scheme depicting the vibration modes of the iTO- and iLO-phonons associated with the G band at the Γ point, c) Scheme depicting the vibration mode of the iTO-phonon associated with the D and 2D band at the \mathbf{K} point.	10
1.5	a) Raman spectra of pristine and defected graphene, b) G band process, c) double-resonant D band process, d) second-order 2D band process, e) intravalley double resonant D' band process, f) intravalley double resonant 2D' band process.	11
1.6	a) Scheme of the polarization-dependent 2D Raman process involving electrons with momenta k and k' , described by the respective angles θ and θ' , at the \mathbf{K} and \mathbf{K}' points, b) Polarized Raman spectra obtained for a fixed excitation polarization and a varied analyzer polarization.	13
1.7	a) Normalized Raman 2D/G ratio as a function of the polarization for the scattered light, b) Normalized 2D/G intensity ratio as a function of the relative angle β measured for different incident polarization α .	14
1.8	a) Light absorption process contour plot, b) Stokes process contour plot, c) Polar plot of experimental and calculated 2D/G intensity ratio as a function of β .	16
1.9	Construction of a (6,5) SWCNT unit cell by rolling up a rectangular stripe of graphene with chiral vector \vec{C}_h , translation vector \vec{T} and the graphene lattice vectors \vec{a}_1 and \vec{a}_2 .	19
1.10	The chiral index (n,m) determines whether SWCNTs are metallic or semi-conducting.	20

1.11	Schematics of the SWCNT band structure with a band gap between the highest valence band and the lowest conduction band, a) dominant transitions E_{11} and E_{22} polarized parallel to the nanotube axis, b) less prominent transitions E_{12} and E_{21} polarized perpendicular to the nanotube axis. . . .	21
1.12	a) Raman spectra of nanographite samples with different crystallite sizes L_α , b) Plot of the intensity ratio I_D/I_G for nanographite samples as a function of $1/L_\alpha$	23
1.13	a) Raman spectra of SLG samples exposed to Ar^+ ion-bombardment with distinct ion doses, b) The plot I_D/I_G as a function of the average distance between point defects L_D for samples exposed to distinct Ar^+ doses. . . .	24
1.14	Simulation of point-defects created by the impact of an ion on the graphene sheet with two distinct regions: the activated A-region and the structurally disordered S-region. a) - d) Simulation for different defect concentrations a) $1011 \text{ Ar}^+ \text{ cm}^{-2}$; b) $1012 \text{ Ar}^+ \text{ cm}^{-2}$; c) $1013 \text{ Ar}^+ \text{ cm}^{-2}$; d) $1014 \text{ Ar}^+ \text{ cm}^{-2}$. . .	25
2.1	Exemplary TEM images of Au Nanorods. TEM image of a) a single Au nanorod, b) and c) Au nanorod clusters.	29
2.2	Histograms of the 630 nm resonant Au nanorod spatial features, a) aspect ratio, b) long axis, c) short axis.	30
2.3	Histograms of the 780 nm resonant Au nanorod spatial features, a) aspect ratio, b) long axis, c) short axis.	30
2.4	Scheme of the confocal microscope setup with the detection methods back focal plane imaging, confocal imaging and spectroscopy.	33
2.5	a) Illustration of the different angular zones for dipolar radiation at a dielectric substrate upper half-space (P_u), forbidden zone (P_f), allowed zone (P_a) and surface of the dielectric, b) Projection of the angular radiation into the allowed zone with the critical angle θ_{crit} and maximal collection angle θ_{max}	36
2.6	Geometry used for the calculation dipolar radiation patterns at an interface.	37
2.7	Calculated radiation patterns of dipoles on a glass/air interface for, a) a x-dipole with $\Phi = 0^\circ$ and $\Theta = 90^\circ$, b) a y-dipole with $\Phi = 90^\circ$ and $\Theta = 90^\circ$, c) a z-dipole with $\Phi = 0^\circ$ and $\Theta = 0^\circ$, d) a random orientated dipole with dipole components \vec{p}_1 , \vec{p}_2 and \vec{p}_3 oriented along the cartesian coordinate axes.	40
2.8	a) Imaging of the microscope objective's BFP, b) illustration of the inverse radiation paths of the emitted signal and the light of a laser pointer for alignment.	42
2.9	Effect of installing a pinhole in the focus of the TL on dipole radiation patterns. Calculated dipole radiation patterns a) before and b) after mathematical broadening, c) Cross-sections of both calculated patterns through their corresponding pattern maxima.	43

2.10	a) Scheme of the microscope objective's composition with beampath of rays emitted at different angle, b) Objective quality and alignment sensitivity of the used objective, c) Influence of the objective's magnification on the radiation pattern size, d) Vignetting reductions of effective NA. Fraction of light transmitted for full field of view.	44
3.1	a) Back focal plane geometry with plain of incidence, b) Scheme illustrating the geometrical relationships for the adjustment of the electrical field components.	49
3.2	Non-polarized and polarized radiation patterns of single point-dipoles, a) Calculated y-dipole pattern, non-polarized, parallel and perpendicular polarized, b) Experimental radiation pattern of SWCNT oriented along y, non-polarized, parallel and perpendicular polarized, c) Calculated dipole pattern with $\Phi = 315^\circ$, non-polarized, x- and y-polarized, d) Calculated parallel and perpendicular polarized electric field patterns for a y-dipole.	50
3.3	Raman spectrum of the investigated graphene flake. The inset shows a Raman 2D confocal micrograph of the studied flake.	52
3.4	a) Experimental and calculated G peak radiation patterns with and without analyzer, b) Cross-sections taken through the center of the experimental and calculated BFP patterns in a).	53
3.5	a) Experimental and calculated 2D radiation patterns with and without analyzer, b) Cross-sections taken through the center of the experimental and calculated BFP patterns in a).	54
3.6	a) Scheme illustrating the excitation in the 3-dipole model, b) The patterns of the three dipoles summed up accordingly result in the same pattern as for the 2-dipole model.	55
3.7	a) Depolarization of excitation p_L and emission p_S at the glassair interface as a function of the focusing angle θ , b) experimental and calculated 2D intensity ratio for parallel and perpendicular polarized light $r_{2D} = I(2D)_{\parallel}/I(2D)_{\perp}$	57
3.8	a) Parallel polarized SLG Raman Spectra as a function of NA, b) NA dependence of $I(2D)/I(G)$	58
3.9	Experimental and coherent case calculation for 2D intensity ratio for parallel and perpendicular polarized light.	59
3.10	Experimental and calculated fraction of detected light as a function of NA.	60
4.1	The procedure for the recycling of the precipitate from the previous sonication-centrifugation process.	65
4.2	a) Absorption spectra of the different dispersions, b) The summarized absorbance of dispersions 1-4 compared to direct sonication for 80 min, c) Proposed mechanism for the unexpected optimum of the dispersion efficiency.	66
4.3	AFM micrographs of the SWCNTs extracted from <i>dispersion 1</i> , <i>dispersion 4</i> and the <i>80 min dispersion</i> . The length histograms were obtained from multiple micrographs.	68

4.4	Typical raw Raman spectrum. The inset shows an exemplary confocal Raman G' image of SWCNTs self-assembled by the coffee-ring effect for the Raman investigation.	69
4.5	Distribution of the D/G intensity ratio of SWCNTs from a) dispersions fabricated with increasing sonication time t , b) dispersions of different recycling steps.	70
4.6	Distribution of the D/G' intensity ratio of SWCNTs from a) dispersions fabricated with increasing sonication time t , b) dispersions of different recycling steps.	70
A.1	x- and y-polarized radiation patterns calculated for dipoles with $\Phi=0^\circ, 90^\circ, 45^\circ$ and 315°	78
B.1	Understanding optical antennas. a) Principle of an antenna, b) Origin of the surface plasmon resonance.	86
B.2	Influence of the antenna-effect on the radiation of a single dipolar emitter.	87
B.3	Localization of a single gold nanorod deposited on graphene, a) Overexposed Darkfield Scattering image of a single Au nanorod deposited on graphene, b) Confocal Raman 2D Image of a single Au nanorod deposited on graphene.	88
B.4	a) Non-polarized and b) polarized darkfield scattering spectrum of a single Au nanorod.	89
B.5	a) Absorption spectrum of gold nanorods resonating at 780 nm (on glass) in aqueous solution, b) Confocal Raman G image of graphene with deposited gold nanorods.	91
B.6	Raman G radiation pattern of graphene recorded at antenna distance x . a) $x=700$ nm, b) $x=400$ nm, c) $x=0$ nm	91

List of Publications

During the course of my PhD research, the following peer-reviewed papers have been published:

- Stefan Weigand, Harald Budde, Karlheinz Sünkel, „2-Pyridylmetallocenes, Part V. Synthesis of Hydroxymethyl-, Formyl- and Carboxy-pyridylferrocene and Study of their Cycloplatination Reactions. Molecular Structures of $[C_5H_3R(2-C_5H_4N)-1,2Fe Cp]$ (R= CHO, COOH) and σ -Pt $[(C_5H_5)FeC_5H_2(2-C_5H_4N)(CH_2OH)]Cl$ (DMSO)“, *Z. Anorg. Allg. Chem.* 639, 1242 (2013).
- Harald Budde, Nicolás Coca-López, Xian Shi, Richard Ciesielski, Antonio Lombardo, Duhee Yoon, Andrea C. Ferrari, Achim Hartschuh, „Raman Radiation Patterns of Graphene“, *ACS Nano* 10, 1756 (2016).
- Mona Calik, Torben Sick, Mirjam Dogru, Markus Döblinger, Stefan Datz, Harald Budde, Achim Hartschuh, Florian Auras, Thomas Bein, „From Highly Crystalline to Outer Surface-Functionalized Covalent Organic Frameworks - A Modulation Approach“, *J. Am. Chem. Soc.* 138, 1234 (2016).
- Thomas Ackermann, Harald Budde, Elina Fuks, Achim Hartschuh, Siegmund Roth, „Recycle it: Material-efficient dispersing of carbon nanotubes without scission“, submitted to *Scientific Reports* (2016).

List of Conferences

- DPG Frühjahrstagung 2012, Berlin (Germany), 25.03. - 30.03.2012
Poster: Fabrication and Characterization of Self-Assembled and Self-Aligned Single-Walled Carbon Nanotubes
- WNCO 2012, Niederstetten (Germany), 25.09. - 28.09.2012
Oral Presentation: Fabrication and Electroluminescence of Self-Assembled and Self-Aligned Single-Walled Carbon Nanotube Networks
- CeNS Workshop Venice 2012 Nanosciences: „Soft, Solid, Alive and Kicking“, San Servolo (Italy), 17.09. - 21.09.2012
Poster: Fabrication and Characterization of Self-Assembled and Self-Aligned Single-Walled Carbon Nanotubes
- NIM Winterschool 2013, Kirchberg (Austria), 03.03.2013 - 09.03.2013
Oral Presentation and Poster: Fabrication and Characterization of Self-Assembled and Self-Aligned Single-Walled Carbon Nanotubes
- WNCO 2013, Knottenried (Germany), 07.10. - 10.10.2016
Oral Presentation: Evaporation-Driven Sorting of Single-Walled Carbon Nanotube Chiralities
- DPG Frühjahrstagung 2014, Dresden (Germany), 30.03. - 02.04.2014
Oral Presentation: Back Focal Plane Imaging of Raman Scattering from Graphene
- DPG Frühjahrstagung 2015, Berlin (Germany), 15.03. - 20.03.2015
Poster: Polarization-Dependent Radiation Patterns of Raman Scattering from Graphene
- WONTON 2015, Kloster Banz (Germany), 31.05. - 04.06.2015
Poster: Polarization-Dependent Radiation Patterns of Raman Scattering from Graphene
- IWEPM 2016, Kirchberg (Austria), 13.02. - 20.02.2016
Poster: Raman Radiation Patterns of Graphene
- EMRS 2016 Spring Meeting, Lille (France), 02.05. - 06.05.2016
Oral Presentation: Raman Radiation Patterns of Graphene

Acknowledgements

First, I want to thank **Prof. Achim Hartschuh** for giving me the opportunity to experiment and study in his group. I learned a lot about the world of nanooptics due to his support. I also want to thank him for sending me to various conferences in- and outside of Germany. That way I could meet many interesting people, learn more about my field from different points of view and of course could enjoy the local cuisine and culture.

I want to thank **Prof. Don C. Lamb** for his fast decision to be my second reviewer and taking the time to look at my work.

Many thanks to my collaborators **Dr. Duhee Yoon** and **Thomas Ackermann** for the long discussions and cooperative atmosphere during our scientific work. I also want to thank **Dr. Sophia Betzler** and **Dr. Mauricio Pilo-Pais** for their TEM and Darkfield microscopy measurements of gold nanorods as well as their advice and suggestions.

I am also very grateful to **Dr. Alberto Comin** and **Dr. Matthias Handloser** for the countless scientific discussions and their invaluable support regarding soft- and hardware issues.

I especially want to thank my colleagues **Kevin, Nico, Richard, Tobia** and **Xian** for the great time we had in- and outside of the lab. For the latter part I also want to include **Lijing** and **Rachele**. I will never forget the fun we had cooking, drinking, chatting about anything and everything, eating hotpot, making music in a band, singing 7 drunken nights, hiking to Kloster Andechs, sledding down the Wallberg, failing at producing honeywine in a pumpkin at Halloween and myriads of other activities. Thank you for your practical and moral support and of course for your friendship! You guys rock! Open!

Of course I want to thank the whole Hartschuh group! **Alex, Andrew, Dawid, Giovanni, Irene, Julia, Katrin, Miriam, Nicolai, Nina, Sabrina, Tobias** and **Veit**: I had a good time with you guys.

I also appreciate the excellent collaboration of my lab course students **Irene** (who now is also a member of the group), **Rebekka, Kerstin, Elina** and **Patricia** who did a very good job in supporting me at the study of evaporation-induced self-assembly of carbon

nanotubes (expanding on the work of my master thesis) and antenna-enhanced Raman radiation patterns.

At this point I want to thank all my friends who did a good job in distracting me from writing when a break was necessary and making hilarious comments about my situation whenever possible. Keep reaching for that rainbow! Vielen Dank für eure Freundschaft!

Meine Familie war in dieser Zeit eine große Hilfe. Die vielen kleinen kulinarischen Köstlichkeiten und Unterhaltungen mit denen mich **meine Eltern** während meiner Doktorarbeit unterstützt haben bedeuten mir viel! Ein großer Dank gilt auch meinem Bruder **Michael**, dessen Rat in unterschiedlichen Bereichen ich sehr schätze. Danke, dass ihr mich mein Leben lang gefördert habt!

Last but not least I want to thank my girlfriend **Julia** for her continuous support. Especially her patient listening to my lamentations and words of motivation when things did not go as smoothly as expected helped a lot! Danke, dass es dich gibt!